# 2D COORDINATE SPACE HARTREE-FOCK-BOGOLIUBOV CALCULATIONS FOR NEUTRON-RICH NUCLEI IN THE $A \sim 100$ MASS REGION

By

Artur Robert Blazkiewicz

Dissertation

Submitted to the Faculty of the

Graduate School of Vanderbilt University

in partial fulfillment of the requirements

for the degree of

DOCTOR OF PHILOSOPHY

in

Physics

December, 2005

Nashville, Tennessee

Approved

Prof. Volker E. Oberacker

Prof. A. Sait Umar

Prof. S. Victoria Greene

Prof. Thomas J. Weiler

# ACKNOWLEDGMENTS

At the end of my thesis I would like to thank people who made this thesis possible and an enjoyable experience for me.

First of all I wish to express my sincere gratitude to my supervisor Prof. Volker E. Oberacker, who guided this work and helped whenever I was in need.

I am also indebted to Prof. Sait A. Umar for his numerical expertise and providing the most updated software.

I am grateful to the members of my committee for their support and their comradeship, Prof. Victoria Green, Prof. Thomas Weiler and, late Prof. Robert Panvini.

Finally, I would like to express my deepest gratitude for the constant support, understanding and love that I have been receiving from my wife Anupama. Special thanks to Prof. L. Smentek and my family, my brother and my late mother. My mother's love and encouragement had been for me invaluable until her death on April 2002.

I acknowledge the financial support under U.S. Department of Energy grant No. DE-FG02-96ER40963 with Vanderbilt University and McMinn fellowship which I have been receiving for the past four years. Most of the numerical calculations were carried out at the Vanderbilt University's ACCRE multiprocessor platform and also at the IBM-RS/6000 SP supercomputer of the National Energy Research Scientific Computing Center which is supported by the office of Science of the U.S. Department of energy.

TABLE OF CONTENTS

LIST OF TABLES

Table Page

LIST OF FIGURES

# CHAPTER I

# INTRODUCTION

## 1.1 Overview

This work concentrates on the properties of the neutron-rich nuclei in the $A \sim 100$ mass region. The results are obtained by solving the axially symmetric Hartree-Fock-Bogoliubov equations in coordinate space on the two-dimensional (2D) lattice utilizing the basis-spline expansion method.

The introduction section of Chapter I contains a brief description of the physics of neutron-rich nuclei and its role in the formation of the complete nuclear structure theory. In the same chapter we review the basic modern theoretical methods of description of the nuclear many-body problem.

In Chapter II the formal structure of the free Nucleon-Nucleon interaction is derived and its properties are compared to the effective interaction inside the nuclear medium. The necessity of using the phenomenological interactions (Skyrme SLy4) instead of the effective ones obtained by solving the Bethe-Goldstone equation is explained as well.

A detailed derivation and description of the Hartree-Fock-Bogoliubov equations is given in Chapter III. The method of solution of the HFB problem in coordinate-space in axial symmetry on the 2D lattice using the Basis-Splines is described. The new method of solution of the HFB equations as the decoupled set of equations is also presented.

The parallel implementation of the HFB code using Message Passing Interface (MPI) is given in Chapter IV.

Finally, in Chapter V we describe results obtained for the two neutron-rich chains of ${}^{104-116}_{36}$Kr and ${}^{102-122}_{40}$Zr isotopes. In studies of the Zr isotopes a comparison with the calculations of Stoitsov et al. of separation energies, deformations, rms-radii, pairing gaps and neutron densities is made. The studies of the rate of convergence of the HFB observables is also included in this Chapter. The calculations of the Kr isotope chain reveal the deformation change similar as in the case of the Zirconium isotopes. The calculations for the Kr isotopes confirmed also that the mass region of $A \sim$ is the area of competition between

various coexisting nuclear shapes.

The main conclusion ends this thesis as the Chapter VI.

## 1.2 Nuclear landscape including neutron-rich nuclei

In nature there are 92 stable elements and about 300 stable isotopes [1]. About 2700 unstable isotopes can be currently obtained experimentally, all of which are radioactive and decay by capture or emission of electrons, positrons, or alpha particles, or by undergoing spontaneous fission.

It is very common to plot all known nuclides with the number of neutrons on the x-axis and the number of protons of the y-axis to obtain the so-called "nuclear landscape" or "valley of stability". On the chart of nuclides (Fig. 1) there are depicted nuclei which have been observed experimentally. The stable nuclei in the middle of the picture are given by the black squares. Below and above of it (colored squares) we can find unstable isotopes. The red lines show the magic numbers. For the light nuclei the stability line is rather straight(N=Z). With increasing mass number the number of neutrons needs to be larger than protons in order to balance the repulsive Coulomb force between protons. The radioactive nuclei can decay via (red squares) beta plus process, (blue squares) beta minus process, (yellow squares) alpha decay, and (green squares ) spontaneous fission.

By adding nucleons to a nucleus we can reach the so-called "drip line", beyond which the nuclei are unstable against nucleon emission (neutron emission for the neutron-dripline, proton emission in case of the proton-dripline). The name drip-line originates from the analogy of water dripping from a leaky faucet to a full cup. One drop above the limit can cause water to spill over or drip out of the cup. Similarly, if too many neutrons or protons are added to the nucleus, it will decay to the more stable one by emitting nucleons.

The experimental data up to today are only available for the nuclei relatively close to the stability line. For many others even if they can be observed not even basic properties such as mass, shape, half-life and the lowest excited states are known. The problem lies in the experimental difficulties of obtaining and measuring the properties of short lived nuclear systems.

The nuclear landscape (Fig. 1) shows only nuclei which have been obtained experimentally. The theoretical calculations can go beyond that, predicting the existence of thousands exotic radioactive nuclei (Fig. 2). This unstable area indicated in green in Fig. (2) is called the "Terra Incognita", meaning in Latin "unexplored land".

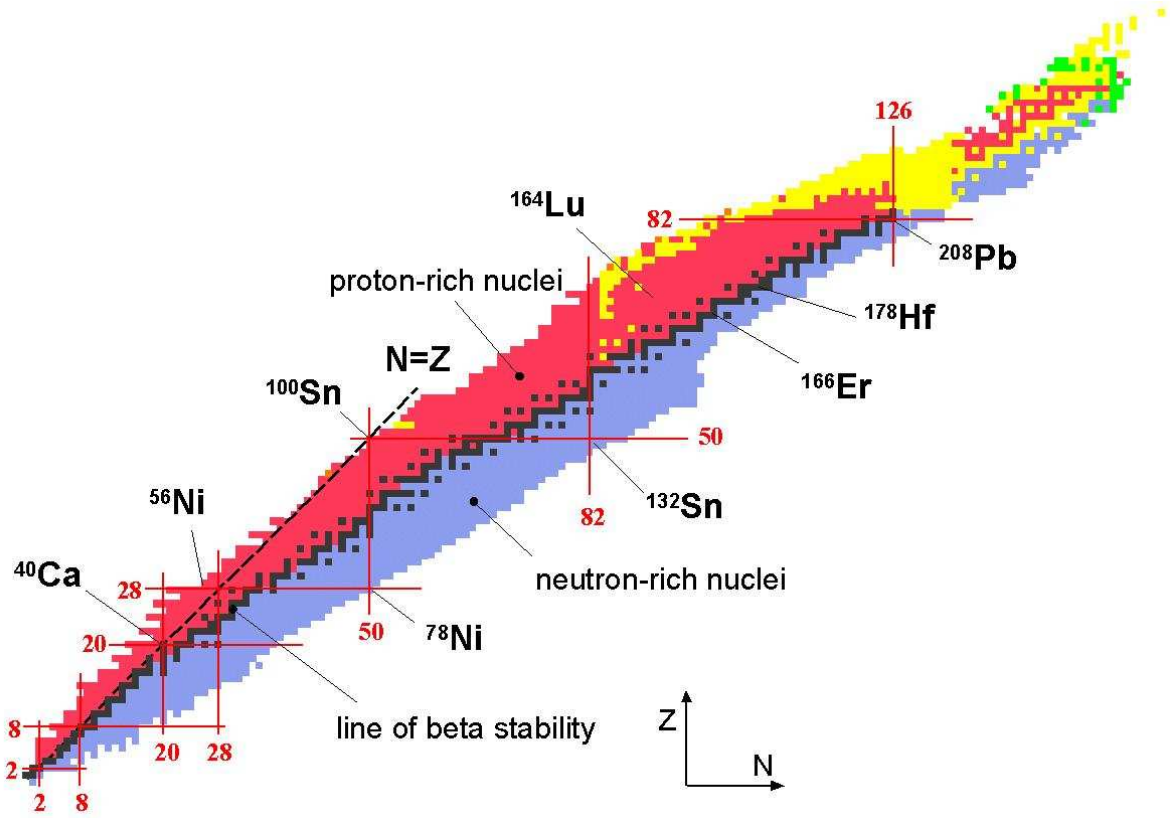


Figure 1: The nuclear landscape. Shown are isotopes obtained experimentally. Figure by Claes Fahlander, Nuclear Structure Group from Lund University, Sweden.

This work addresses the properties of the neutron-rich nuclei. An exploration of nuclei with large neutron excess is not only motivated by predicting the neutron-dripline. Researching such nuclei is governed, among other factors, by fundamental goal of nuclear structure physics, which is to predict the form of the effective nucleon-nucleon interaction. The effective nucleon-nucleon (N-N) interaction (inside the nucleus) is radically different from the free N-N interaction, and in particular depends on the neutron and proton densities (see section (2.2)). At present the precise analytical form of the nuclear Hamiltonian is not known - it can only be approximated. There is a hope that probing nuclei under extreme conditions will enable to achieve this goal.

The physics of neutron-rich nuclei is expected to possess radically new features, e.g. the strong density dependence of the effective interaction between the nucleons may lead to

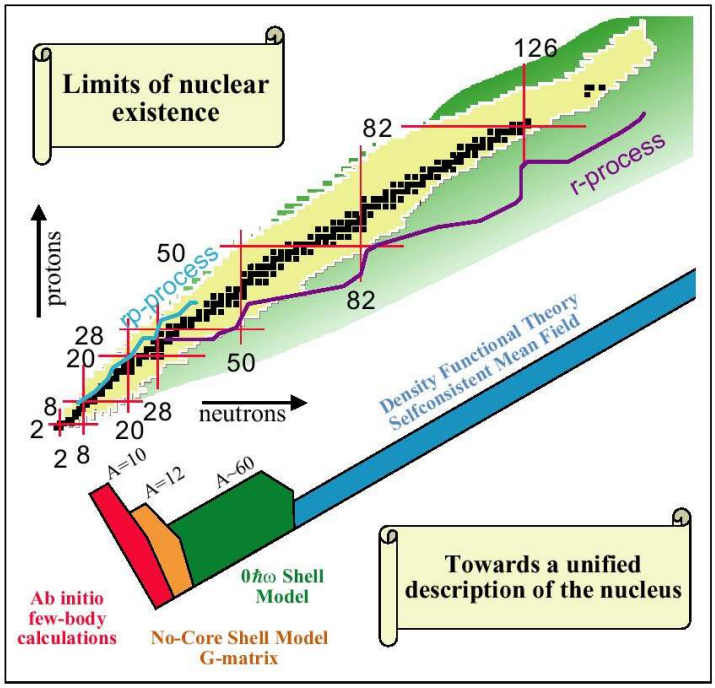


Figure 2: Nuclear landscape including the nuclei predicted theoretically ("Terra Incognita"-green color ). Shown are also the many-body nuclear structure theories as a function of the mass number A and the r-process path. The r-process path in the NZ-plane connects the maximum-abundance isotopes of all the isotopic chains. Figure is From [2].

radically different nuclear symmetries and excitations.

One of the predicted new features is the change in the single-particle energy levels, which will be shifted and re-ordered as the dripline is reached. The change will manifest itself as the breakdown of traditional shell gaps and magicity (Fig. 3) (e.g numbers 50 and 82). These shell gaps are associated with magic numbers, which correspond to particularly stable nuclei. The main reason for this change is the reduction in the spin-orbit interaction strength in nuclei with the large neutron excess. Another feature of the changed structure of the single-particle spectrum of the neutron-rich nuclei is the proximity of the neutron Fermi level to the continuum states (Fig. 4).

One of the important feature of the neutron rich nuclei is the weak binding of the outer nucleons, which gives rise to the very different nuclear density distributions and sizes compared to the stable nuclei. In certain neutron-rich light nuclei, the wave function describing

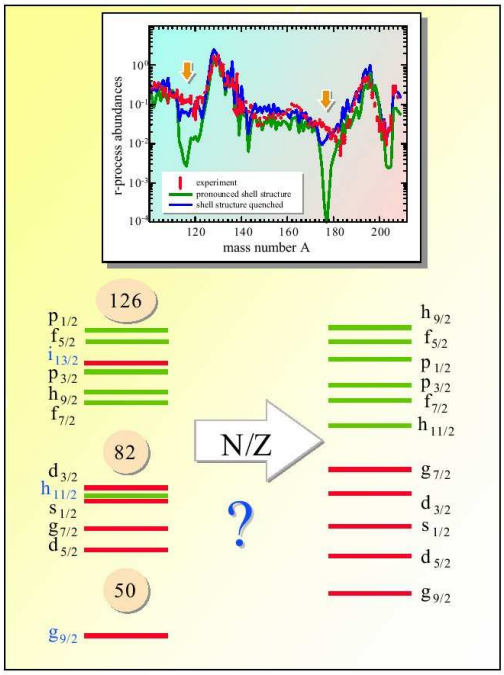


Figure 3: Left: Spherical shell structure characteristic of stable nuclei. Right: Neutron shell structure predicted for neutron-rich nuclei shows the quenching of the magic gaps at N=82 and N=126 (from J. Dobaczewski et al., PRC53, 2809 (1996)). In the inset the red squares represent the experimentally deduced r-process solar abundances. The theoretical abundances are marked by green (incorporates the shell structure similar to the stable nuclei) and blue (incorporates the shell structure with the quenched magic gaps). It is seen that the calculations, which incorporate the shell structure characteristic for the neutron-rich nuclei greatly improve the agreement with the experimental solar abundances (from Pfeiffer et al. Z.Phys. A357, 235 (1997)).

the quantum state of the last neutron or neutrons, extends to large distances, well outside the nuclear core. These last few neutrons spend most of their time far from the normal density core of the nucleus and form a "halo" [3]. In heavier nuclei a related phenomenon is the large spatial extension of the neutron density compared to the proton density, which shows up as the so-called "neutron-skin". Its formation has some intriguing consequences; the outer neutron skin would represent effectively a new form of nuclear matter, which in its purest state is only found in neutron stars. The formation of a skin opens up also the possibility of new modes of collective motion, exhibited as the oscillations of the skin against the core, e.g. the "scissors" vibrational mode [4].

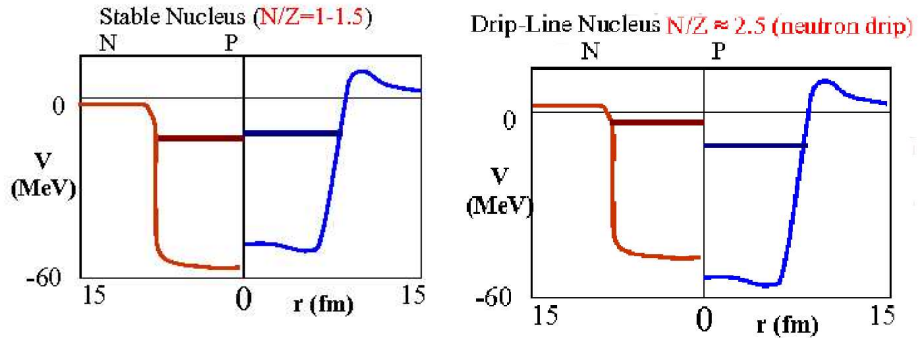


Figure 4: The potential wells (neutrons+protons) for the stable nucleus (left) and neutron-rich system (right) .

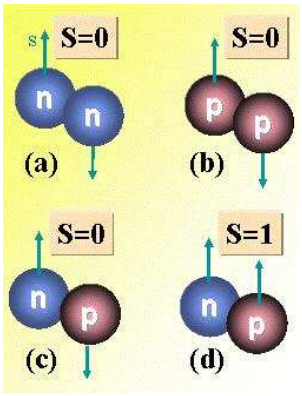


Figure 5: Four different possibilities of forming the Cooper-pairs in the nucleus.

Another phenomenon which occurs in nuclei is the analog of superconductivity in solid state physics, where a total of four classes of correlated pairs can form (Fig. 5), each of which involves an enhanced (attractive) interaction. The phenomenon of superconductivity is very well known in solid state physics and stems from the interaction between correlated "Cooper" pairs of electrons of opposite spin moving in opposite directions within an ionic lattice structure. In the heavier nuclei only the neutron-neutron and proton-proton correlations are important due to the different Fermi levels [5], unlike in case of the $N \approx Z$ nuclei where the Fermi levels are almost the same (Fig. 4).

The detailed understanding of the structure of exotic nuclei is intimately connected to astrophysics, since the nucleosynthesis - which usually happens inside massive stars -

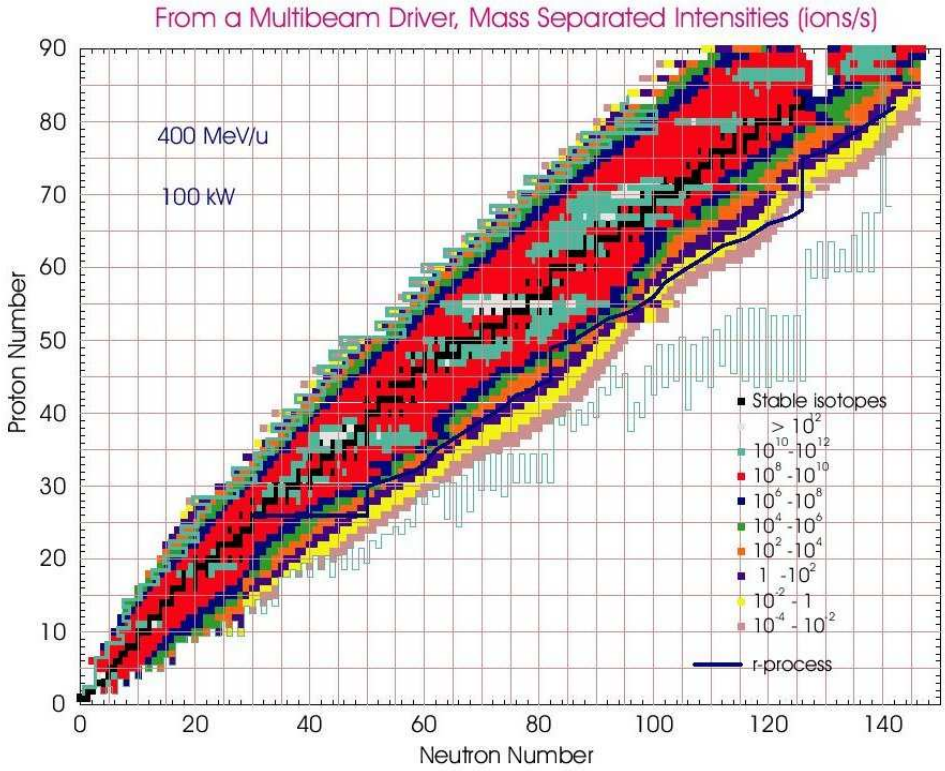


Figure 6: Estimates of the intensity of radioactive beams in ions/s that will be available at RIA. From [2].

is typically taking place in regions of extreme neutron to proton ratios. The isotopes of elements beyond Fe are formed in the neutron-capture process inside the type II supernovae, which eject a rich flux of neutrons during their core collapse process [6]. The two main n-capture processes for astrophysical nucleosynthesis are called the slow (s) and (r) rapid n-capture process. In the s-process, the time $\tau_n$ between two successive captures of the neutrons is much longer than the mean beta-decay lifetime $\tau_\beta$, where the opposite holds for the r-process ($\tau_n << \tau_\beta$) . The r-process path in the NZ-plane (Fig. 3) connects the maximum-abundance isotopes of all the isotopic chains. During the core collapse, when the intense neutron flux ends, a nucleus on the r-process path will beta decay back up to the valley of stability and produce one of the stable nuclei. The determination of the r-process path relies on the nuclear mass models, which can provide the separation energies $S_n$ for the neutron-rich nuclei. Thus, the properties of very neutron-rich nuclei are linked to the

r-process component of the solar system abundances of heavy elements (inset of Fig. 3).

These intriguing predictions can only be tested by experiments on the most neutron-rich nuclei. A major thrust in nuclear science is physics associated with the rare isotope beams, which address basic questions of nuclear structure, nuclear astrophysics, and fundamental interaction physics. Intense beams of heavier neutron-rich nuclei will provide an enormous boost to the studies of properties of exotic nuclei. Among many existing rare isotopes research laboratories in the world are CERN ISOLDE facility [7], TRIUMF (Vancouver) [8], NSCL at Michigan State University [9], ATLAS at the Argonne National Laboratory [10], HRIBF at Oak Ridge National Laboratory [11]. There are also plans to build modern large-scale facilities in Japan(RIKEN[12]), Europe(GSI[13]), and in USA(RIA[14]). RIA is a bold new facility concept, whose capabilities will far exceed those of any other facility known so far. Heavy ion beams of more than 400 MeV/nucleon will be available (Fig. 6).

### 1.3 Modern theoretical methods of description of the nuclear many-body problem

The properties of all existing and theoretically predicted nuclei can be calculated based on various nuclear many-body theoretical frameworks. This is certainly a triumph of the theoretical many-body nuclear science. Yet, still a lot needs to be done to achieve a complete description of properties of the nuclear systems. In Fig. (2) the nuclear many-body theories as the function of the mass number are shown. The area up to the mass number $A \approx 10$ can be described by the family of methods called Ab initio ( Latin -"from first principles") methods. Currently, the Ab Initio methods unfortunately cannot be extended to describe systems heavier than $A \approx 10$. Therefore scientists utilize the shell-model methods for A $>$ 10. After the mass region of A $> 60$, the shell model needs to be substituted by the density functional theories based on the self-consistent mean-field. The Ab initio methods and the Shell-Model can in principle be extended to a heavier regimes if more powerful computers and algorithms are available in the future. The density-functional theory though, works better for the relatively large mass numbers, where the concept of the average mean-field is better justified. The classification of nuclear many-body methods can be also done from the point of view of the NN nuclear interaction, from which the many-body Hamiltonian is constructed. While the Ab Initio methods can use both the free NN interaction or

effective interaction as the input, the Shell Model and density functional theories both rely on effective interactions (Fig. 7). In the next subsection we review the latest research for the Ab Initio and Non Ab Initio methods.

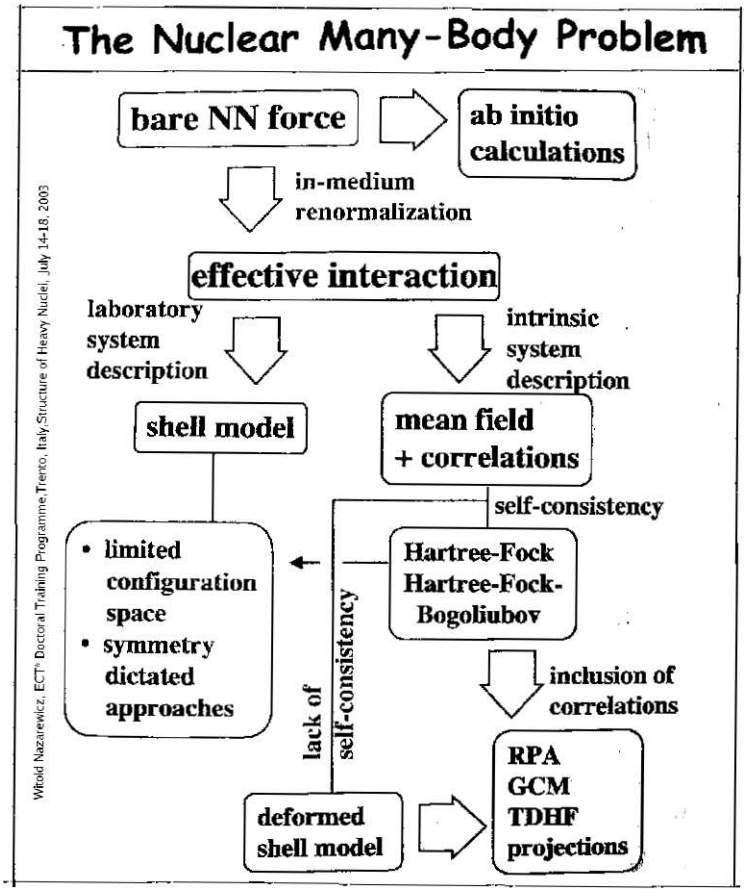


Figure 7: Classification of the many-body theories according to the type of interaction. Figure by Witold Nazarewicz, ECT* Doctoral Training Programme, Trento, Italy, "Structure of Heavy Nuclei", July 14-18, 2003.

### 1.3.1 Ab Initio methods

Ideally, one would like to calculate properties of the A-nucleon system using the free-space NN interaction fitted to the properties of NN scattering. Recently, many modern N-N

potentials have been developed, based on meson exchange theories, which fit all available N-N scattering data and properties of the deuteron (sec: 2.1). Originally, the family of the "Ab Initio" methods used as input the free NN interaction to calculate the properties of the nuclei. The classification with respect to the type of the NN interaction is based on the criterion, whether to obtain the effective interaction from the bare NN interactions a fit to the properties of known nuclei was made. If this is so, then the method cannot be called Ab Initio as the calculations are not carried from first principles.

No Core Shell-Model

The No Core Shell-Model Method (NCSM), is based on the concept of the independent particle motion, which is very well known from atomic physics. Similarly, a nucleon in the nucleus moves in the average field (mean-field) generated by the other nucleons. The atomic nucleus, in the mean-field description is assumed to possess a shell-structure by analogy to the electrons in the atom. This is indeed the case and can be observed experimentally by looking at the neutron separation energies [15] and binding energies, which show preferred magic numbers [16]. The independent-particle shell-model was first proposed by Goeppert-Mayer and Haxel Jensen, and Suess to explain the magic numbers in nuclei [17].

In the NCSM there is no assumption of an inner core [18, 19, 20, 21]. All of the nucleons are treated as active particles. The calculations are performed in the harmonic oscillator basis and use the bare interaction as input. The use of the bare interaction causes too slow convergence [22], therefore alternative faster methods need to be used. In order to overcome these difficulties, Navratil et al. [23, 24] introduced an effective interaction which can be derived in a systematic way from the bare NN and 3N forces. The authors start from the one- and two-body Hamiltonian for the A-nucleon system [20]

$$H = \sum_{i=1}^{A} \frac{\mathbf{p}_i^2}{2m} + \sum_{i<j}^{A} V_{ij}, \tag{1}$$

where m is the nucleon mass and $V_{ij}$ is the nucleon-nucleon interaction, which is modified by adding and substracting the center-of-mass harmonic oscillator potential $\frac{1}{2}Am\Omega^2\mathbf{R}^2$, $\mathbf{R} = 1/A\sum_{i=1}^{A}\mathbf{r}_i$. The modified Hamiltonian, depending on the harmonic-oscillator frequency $\Omega$

is alternatively written as

$$H_A^\Omega = \sum_{i=1}^{A} h_i + \sum_{i<j}^{A} V_{ij} = \sum_{i=1}^{A} \left[ \frac{\mathbf{p}_i^2}{2m} + \frac{1}{2} m\Omega^2 \mathbf{r}_i^2 \right] + \sum_{i<j}^{A} \left[ \mathcal{V}_{ij} - \frac{m\Omega^2}{2A} (\mathbf{r}_i - \mathbf{r}_j)^2 \right], \tag{2}$$

where $\mathcal{V}_{ij}$ is the sum of two-body nuclear and Coulomb interaction dependent on the intrinsic coordinates. Since solving the many-body problem in finite HO space using the free NN interaction will cause pathological results, Navratil et al. [23] following Da Providencia and Shakin [25], derived the model-space dependent effective Hamiltonian

$$\mathcal{H} = e^{-S} H_A^\Omega e^S, \tag{3}$$

where $S = \sum_{i<j}^{A} S_{ij}$ is a two-body, anti-Hermitian operator which needs to be found. The transformed Hamiltonian $\mathcal{H}$ can be expanded in terms of up to A-body clusters $\mathcal{H} = \mathcal{H}^{(1)} + \mathcal{H}^{(2)} + \mathcal{H}^{(3)} \ldots$, where one- and two body terms are equal to $\mathcal{H}^{(1)} = \sum_{i=1}^{A} h_i$, $\mathcal{H}^{(2)} = \sum_{i<j}^{A} \tilde{V}_{ij}$, with

$$\tilde{V}_{12} = e^{-S_{12}} (h_1 + h_2 + V_{12}) e^{S_{12}} - (h_1 + h_2). \tag{4}$$

It is possible to determine the transformation operator $S_{12}$ from the decoupling condition between the model space P and Q space on the two cluster level using the projectors P and Q with P+Q=1 requiring

$$Q_2 e^{-S_{12}} (h_1 + h_2 + V_{12}) e^{S_{12}} P_2 = 0. \tag{5}$$

The resulting two-body effective interaction $\tilde{V}_{12}$ depends on A, on the HO frequency $\Omega$, and on $\mathrm{N_{max}}$, the maximum many-body HO excitation energy [23]. It also follows that $\tilde{V}_{12} \to V_{12}$ for $N_{\max} \to \infty$. The approximation made by Navratil et al. [23] is to neglect higher than the two-body clusters in the unitary transformed Hamiltonian expansion, yet the method can generalized to include higher than two-body clusters; e.g. incorporating the three body clusters leads to the inclusion of the three-body interaction [26].

It should be stressed that although the interaction $\tilde{V}_{12}$ is called effective, there is no fit involved to the properties of nuclei, which is often the case in the process of obtaining in medium effective interactions. In that sense the NCSM can be called an "Ab Initio" method. The NCSM calculations are limited; the heaviest calculated system so far is $^{12}$C, where authors calculated the ground states and excited states by extracting the effective interaction

from the "CD-Bonn" and the "Argonne-v18" potentials [23]. The NCSM calculations are computationally very demanding, the matrix size for the $^{12}$C reached 6488004 [23]. In 2003, Navratil et al. [26] incorporated the three-body force on the three cluster level and extended the calculations up to $^{13}$C. A hope to extend the NSCM calculations for heavier systems relies on faster parallel computers and developments in computer hardware and algorithms in the future [22].

Green's Function Monte Carlo method

The Green's Function Monte Carlo method (GFMC) originates from the Variational Monte Carlo (VMC) method developed by Pandharipande and collaborators in 1981 [27]. In the VMC method the many-body ground state energy is obtained by varying the trial many-body wave-function $\Phi_V$

$$E = \frac{\langle \Phi_V | H | \Phi_V \rangle}{\langle \Phi_V | \Phi_V \rangle}, \tag{6}$$

where $H$ is the many body Hamiltonian with realistic two- and three body interactions, e.g. the two-body Argonne $v_{18}$ and three-body Illinois interaction IL2 [28]. The Metropolis Monte Carlo integration is used to evaluate $\langle \Phi_V | H | \Phi_V \rangle$. The variational function $\Phi_V$ is a very sophisticated antisymmetric vector in the spin-isospin space for the nucleus of interest. Each component is a complex valued function of the positions of all A nucleons [22]. There is an enormous number of components in the many-body wave-function $\Phi_V$, e.g. $^3$H has the max. 24 spin-isospin states

$$(pnn\ npn\ nnp) \otimes (\uparrow\uparrow\uparrow\ \uparrow\uparrow\downarrow\ \uparrow\downarrow\uparrow\ \uparrow\downarrow\downarrow\ \downarrow\uparrow\uparrow\ \downarrow\uparrow\downarrow\ \downarrow\downarrow\uparrow\ \downarrow\downarrow\downarrow). \tag{7}$$

The total number of components can be further reduced by using symmetries and isospin conservation, but still we have 16, 160, 1792, 21 504, and 267 168 components for $^4$He, $^6$Li, $^8$Be, $^{10}$B and $^{12}$C respectively [22].

The GFMC is a more accurate method [29] and uses as the starting point the VMC trial wave function $\Phi_V$ [28]. It is a stochastic method that systematically improves on $\Phi_V$ by projecting out the lowest-energy eigenstate from $\Phi_V$ using the evolution operator with imaginary time $\tau = it$

$$\Phi_0 = \lim_{\tau \to \infty} \exp[-(H - E_0)\tau] \Phi_V. \tag{8}$$

In practice the evolution operator is very difficult to calculate. Therefore, the short-time Green's function for the small time step $\Delta\tau = \tau/n$ is used instead [29, 22]

$$\Phi_0 = \{\exp[-(H - E_0)\Delta\tau]\}^n \Phi_V = G^n \Phi_V. \tag{9}$$

In coordinate space this results in a multidimensional integral over 3An (typically more than 100,000) dimensions, which is done by Monte Carlo . Because of the rapid growth of the number of spin-isospin components of the trial wave-function $\Phi_V$, the calculations are feasible up to only A=10 [22]. These requires $\approx 10,000$ processor hours on modern massively parallel computers, or $\approx 10^{16}$ floating point operations, for a single state [22].

Coupled Cluster Expansion method

The Coupled Cluster Expansion Method (CCE) was proposed by Coester and Kummel in 1958-1960 [30, 31, 32] for the description of correlations in finite nuclei. In 1978 Zabolitzky et al. [33] applied this method to $^{40}$Ca. The method is also very well known in computational quantum chemistry [32]. In 2000, Michaila and Heisenberg[34] applied the CCE formalism to the description of the spherical $^{16}$O nucleus using the bare NN interaction. Instead of using the free NN interaction, Dean et al. [32] calculated the properties of $^4$He and $^{16}$O using the renormalized (in terms of the G-matrix, see sec: 2.2) two-body interaction derived from the free "Idaho-A" interaction [35].

In the CCE method the correlated many-body ground state $|\tilde{0}\rangle$ is postulated as the expansion in terms of the n-particle n-hole (np-nh) creation and destruction operators acting on the vacuum $|0\rangle$( n-particle Slater determinant) [34]

$$|\tilde{0}\rangle = \exp(T)|0\rangle, \tag{10}$$

where

$$T = T_1 + T_2 + \ldots + T_A \tag{11}$$

is the cluster correlation operator i.e. [32]

$$T_1 = \sum_{i<e_f} \sum_{a>e_f} t_i^a \underbrace{a_a^\dagger a_i}_{1p-1h}, \tag{12}$$

$$T_2 = \sum_{i,j<e_f} \sum_{ab>e_f} t_{ij}^{ab} \underbrace{a_a^\dagger a_b^\dagger a_j a_i}_{2p-2h}, \tag{13}$$

and higher order terms for $T_3$ to $T_A$ ($e_f$ is the Fermi level). Coupled-cluster theory can be systematically improved by increasing the number of $T_i$ operators one computes. In the present work of Dean et al. [32] one truncates the expansion at the $2p-2h$ level (two-cluster level ) . The expectation value $\langle \mathbf{A} \rangle$ of any operator $\mathbf{A}$ in the ground state $|\tilde{0}\rangle$ is equal to

$$\langle A \rangle = \langle 0| \exp(-T) \mathbf{A} \exp(T) |0\rangle, \tag{14}$$

and the correlation amplitudes $t_i^a, t_{ij}^{ab} \ldots$ are determined by solving the set of coupled non-linear equations [22]

$$0 = \langle 0| \exp(-T) \mathbf{H} \exp(T) O_n^\dagger |0\rangle, \; n \leq A, \tag{15}$$

where $O_n^\dagger = \{1, a_a^\dagger a_i, a_a^\dagger a_b^\dagger a_j a_i, \ldots\}$. The CCE method is computationally very demanding. The authors of Ref. [32] make use of massively parallel computers, which can provide also a large amount of memory. In the future Dean, et al. plan to include $3p-3h$ amplitudes, incorporate the three-body interaction, and calculate properties of heavier systems.

### 1.3.2 Non Ab Initio methods

This section describes the standard Shell-model approach, which is one example of the Non Ab Initio methods. In section (1.3.2) we describe another Non Ab Initio method, namely the Hartree-Fock and Hartree-Fock-Bogoliubov theories - members of the family of mean-field and density functional theories.

Large scale shell-model calculations

The standard Shell Model calculations, in contrast to the NCSM, start from the assumption of an inert core ( LS closed shell). It means that the magic number is associated with the filling of the orbits for a given value of the oscillator major quantum number $N_0 = 2n+l$. For example, we have the following shells p($N_0$=1), sd ($N_0$=2), pf ($N_0$=3) and so on (Fig. 8). The closed shell configuration can be described by a single Slater determinant, using the Hartree-Fock method. For example, for $^{24}_{12}$Mg we close the p-shell ($^{16}$O core) and use as the valence space the $1d_{3/2}, 1d_{5/2}, 2s_{1/2}$ orbitals (Fig. 8). With such a choice of the core the energy is relative to $^{16}$O. The choice of the inert core is successful if calculations describe observed energy levels and transitions for the nuclei covered by the model space. Even the

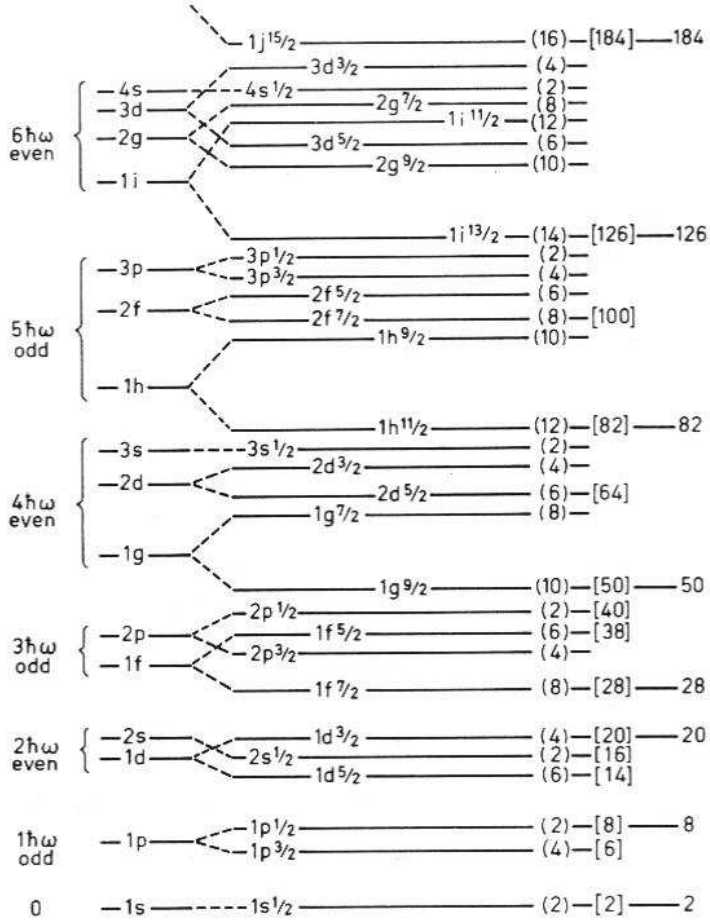


Figure 8: Single-particle energy spectrum of the nucleus with the spherical harmonic oscillator potential and the spin-orbit term. Figure is from [17] .

most successful model will encounter the states attributed to the configuration outside the model space the so-called intruder states. The intruder states start at the excitation energy which is typical of the first excited state in the closed-shell nuclei. They are can be fully incorporated by increasing the size of the model space. However, increasing the size of the model space makes the calculations more time consuming ,as the computation time grows exponentially.

The starting point for the shell model Hamiltonians is the renormalized G-matrix (Eq. 56 ) based upon modern free NN interactions [36]. For the assumed closed core, Brückner's G-matrix theory is used to obtain a set of Two Body Matrix Elements (TBME) for the

chosen model space. During the calculations of the TBME, a fit to the properties of known nuclei is involved. In that sense, the standard Shell-Model method cannot be classified as an Ab Initio method [37]. The G-matrix approach to the nuclear interactions relies upon the use of the harmonic-oscillator basis even in calculations for nuclei close to the dripline [36]. For nuclei far away from the valley of stability, the continuum rather than the oscillator basis should be considered [37].

The modern shell model codes can now be routinely applied up to the lower pf-shell ($^{40}$Ca is the core) nuclei; calculations are limited by the memory requirements during the the standard diagonalization process [38, 39].

The reach of the shell-model calculations was extended by the use of the Monte Carlo techniques (large multidimensional integration instead of diagonalization) [40, 41, 42, 43]. Calculations over the entire region of the pf-shell are now possible. In Ref. [41] the authors calculate various properties of nuclei from the mass region A=64-76. In particular, ground state properties, thermal and rotational pairing properties for N=Z nuclei, Gamow-Teller strengths and distributions e.g. $^{58,60,62,64}$Ni, $\gamma$-Soft nuclei e.g. $^{124}$Xe, $\beta\beta$ decay in $^{76}$Ge.

As stressed in Ref. [41], multi-$\hbar\omega$ (more than one single oscillator shell) Shell Model Monte Carlo calculations are required to properly describe the properties of the neutron-rich nuclei. For example, the structure of light neutron-rich nuclei in the sd-shell requires inclusion of the fp-shell orbitals for the proper description (so-called sdpf-shell, see the calculations of the neutron-rich $^{32}$Mg and $^{46}$Ar). Multi-$\hbar\omega$ calculations require increased memory and computational cycles [41].

Nonrelativistic self-consistent mean-field

The many body Hamiltonian (Eq. 16) depends approximately on at least 3A coordinates, where A is the mass number [44]

$$H = \sum_{i=1}^{A} \frac{-\hbar^2}{2m}\nabla_i^2 + \frac{1}{2}\sum_{ij}^{Z} V_{ij}^{(2)Coul} + \frac{1}{2}\sum_{ij}^{A} V_{ij}^{(2)Nucl} + \frac{1}{6}\sum_{ijk}^{A} V_{ijk}^{(3)Nucl}. \qquad (16)$$

It consists of the kinetic energy operator for the nucleons, two-body Coulomb interaction between protons, and the two-body and three-body strong nuclear interactions . Generally, one has to solve at least A coupled second order partial differential equations. This is

indeed possible with the aid of modern supercomputers and doesn't pose a problem. The real difficulty arises in calculating the observables where one would have to calculate at least 3A dimensional integrals, which is highly impractical.

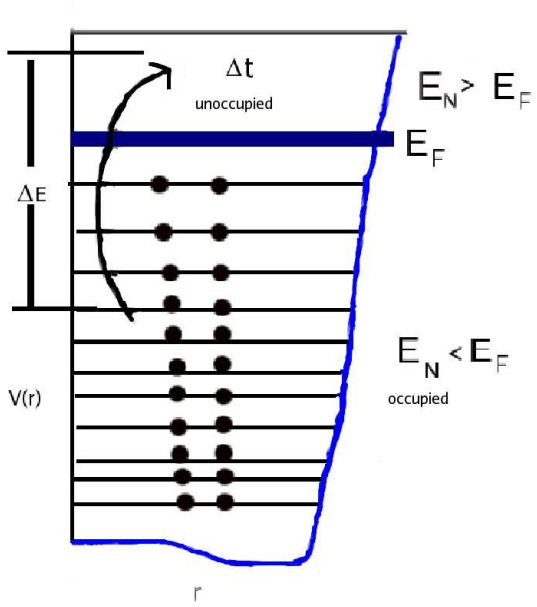


Figure 9: Illustration of the Pauli exclusion principle in the nucleus.

The remedy to this problem is a very well known single-particle description of the many-body system, where a given particle moves in the average "mean-field" generated by the rest of (A-1) particles. The mean-field description of the nucleus assumes that independent nucleons move in almost unperturbed single particle orbits [46](p.36). Such an assumption is valid under the condition that collisions among the nucleons can be neglected and replaced by the collisions with the wall of the mean-field . This can be qualitatively explained by considering the Pauli exclusion principle for the nucleons inside the nucleus (Fig. 9). The scattering of nucleons to a final state below the Fermi level is forbidden by the Pauli exclusion principle as these states are already occupied. The Heisenberg uncertainty principle between energy and time $\Delta E \cdot \Delta t \geq \frac{\hbar}{2}$ allows the non energy-conserving scatterings to unoccupied states above the Fermi level for a short period of time. In first approximation, the scattering

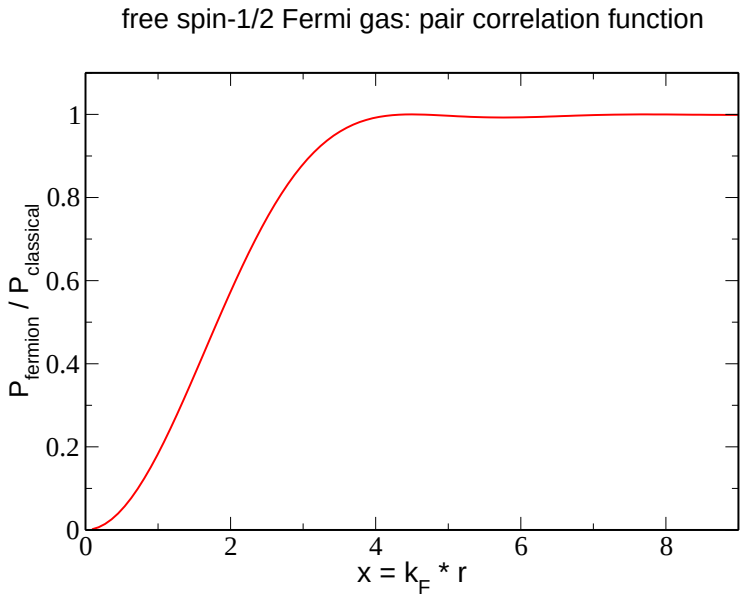


Figure 10: Shown is the pair correlation function for a gas of non-interacting spin-1/2 fermions as a function of the dimensionless distance $x = k_F \cdot r$. The Fermi momentum in nuclear matter is $k_F = 1.3$ fm$^{-1}$ . Figure is from [45].

above the Fermi level at non-relativistic energies can be safely neglected. We can draw a similar conclusion by plotting the pair correlation function for a gas of non-interacting spin-1/2 fermions with the same spin orientation versus the relative distance r (Fig. 10). As shown in the plot, the fermions have a tendency to repel each other at small distances due to the "Pauli correlations". The pair correlation probability vanishes at distance $r = 0$ and is strongly suppressed up to distances of about $r_0 = 2$ fm. As a result, the average distance between nucleons in a nucleus is about 2.4 fm. On the other hand, at such distances the N-N interaction between nucleons becomes weak (Fig. 12), thus the interaction between nucleons inside nuclear medium is effectively quenched by the exclusion principle. Altough Fig. 10 is for a free non-interacting fermion gas, similar results can be obtained for an interacting Fermi gas and for nucleons in the shell model [47](p.248-252).

On the experimental side, the scattering experiments involving incident neutrons and protons [15](p.139) allow also to deduce the mean free path of nucleons. It turns out that the average distance between collisions among the nucleons is comparable with the size of the nucleus. The Pauli exclusion principle, relatively long mean free path for nucleons, and

consequently weak interaction at such distances attribute jointly to the smoothly varying average potential, which is felt by the individual nucleons.

The assumption of the mean-field description greatly simplifies the calculations. The mean-field potential can be obtained from the Hartree-Fock (HF) theory [46, 44, 48] by solving self-consistently the HF equations

$$\underbrace{\left\{\frac{-\hbar^2}{2m}\nabla^2 + \Gamma_H(\mathbf{r},\rho(\mathbf{r}))\right\}\phi_n^{HF}(\mathbf{r}) + \int \Gamma_{Ex}\ (\mathbf{r},\rho(\mathbf{r},\mathbf{r}'))\phi_n^{HF}(\mathbf{r}')d\mathbf{r}'}_{h_{HF}(\mathbf{r})\phi_n^{HF}(\mathbf{r})} = E_n^{HF}\phi_n^{HF}(\mathbf{r}). \tag{17}$$

In Eq. (17) the functions $\phi_n^{HF}$ are the single-particle wavefunctions, $E_n^{HF}$ stands for the single-particle energies, and potentials $\Gamma_H$ and $\Gamma_{Ex}$ are the one-body mean-field (Fock term) and the exchange terms respectively, extracted from the two-body $V^{(2)}$ and three-body $V^{(3)}$ nuclear interactions. As we can see the mean-field potential depends on the density and density matrix

$$\rho(\mathbf{r}) = \sum_{j=1}^{F}\phi_j^*(\mathbf{r})\phi_j(\mathbf{r}), \tag{18}$$

$$\rho(\mathbf{r},\mathbf{r}') = \sum_{j=1}^{F}\phi_j^*(\mathbf{r})\phi_j(\mathbf{r}'), \tag{19}$$

which is what makes Eq. (17) nonlinear in the wavefunctions $\phi_n^{HF}$. In order to solve the HF-equations for a given single-particle wavefunction $\phi_n^{HF}$, one needs to know all of the wavefunctions, which enter via densities $\rho(\vec{r})$ and $\rho(\vec{r},\vec{r}')$. The total energy of the system in the HF theory is not a sum of the single-particle energies $E_n^{HF}$, because particles are not free. Rather, it is the expectation value of the many-body Hartree-Fock Hamiltonian $H^{HF}$,

$$E_0^{HF} = \langle\Phi_0^{HF}|H^{HF}|\Phi_0^{HF}\rangle, \tag{20}$$

$$H^{HF} = \sum_{i=1}^{A} h_{HF}(i), \tag{21}$$

in the Hartree-Fock ground state $|\phi_0^{HF}\rangle$, which is a Slater determinant [46, 44, 48] . In particular, for the Skyrme forces, Eqs. (68-71), the mean-field energy functional is composed of the kinetic energy term, the Skyrme functional term, the Skyrme spin-orbit term, Coulomb term, and center of mass correction term [49, 50]

$$E_0^{HF} = E_{kin} + E_{Sky} + E_{Sky,LS} + E_{Coul} + E_{CM}. \tag{22}$$

The Skyrme part of the energy is a functional (for even-even nuclei and time-reversal invariance) of the total density $\rho$ and the density for protons or neutrons $\rho_{q=p,n}$, the total kinetic energy density $\tau$ and the kinetic energy density $\tau_q$ for protons or neutrons, and the gradients of the densities $\rho$ and $\rho_q$

$$E_{Sky}(\rho,\rho_q,\tau,\tau_q,\nabla\rho\ldots) = \int d^3r \left[ b_0\rho(\mathbf{r})^2 + b_1\rho(\mathbf{r})\tau(\mathbf{r}) - \frac{b_2}{2}\rho(\mathbf{r})\nabla^2\rho(\mathbf{r}) + \frac{b_3}{3}\rho(\mathbf{r})^{\alpha+2} \right] \quad (23)$$

$$- \int d^3r \sum_\alpha \left[ \frac{b_0'}{2}\rho_q^2 + b_1'\rho_q\tau_q - \frac{b_2'}{2}\rho_q\nabla^2\rho_q + \frac{b_3'}{3}\rho^\alpha\rho_q^2 \right]. \quad (24)$$

In the HF theory it is assumed that the nucleons move in the average mean-field and undergo independent particle motion. This is of course an approximation. In extracting the mean-field potential $V_{NN}^{(1)}$ (Eq. (17)) one neglects the so-called residual part, $H_{res}$, of the interaction . This can be seen if we decompose symbolically the Hamiltonian from Eq. (16) as

$$H = \underbrace{T^{(1)} + V^{(1)}}_{H_{mf}} + \underbrace{[V^{(2)} + V^{(3)} - V^{(1)}]}_{H_{res}} \equiv H_{HF} + H_{res}, \quad (25)$$

where the one body mean-field potential (derived from the HF theory ) $V^{(1)}$ was added and subtracted. The Hartree-Fock theory describes the properties of nuclei near the line of stability. The more accurate description requires an inclusion of the the residual part of the Hamiltonian (Eq. 25) into the theoretical framework. This is done, for example, in:

- HF+BCS - theory (short-range part of the residual force represented as the pairing force between nucleons) [51, 52]
- HFB -theory ("Hartree-Fock-Bogoliubov"), see chapter (III) - self-consistent mean-field+pairing
- RPA - theory ("Random Phase Approximation", linear response theory) [46, 48, 44] - describes excited states.

Relativistic Mean-Field models

The biggest advantage of nuclear models based on the relativistic mean-field (RMF) approximation is that the spin-orbit interaction arises naturally as a result of the Dirac

structure of nucleons. In this model the, nucleus is described as a system of Dirac nucleons which interact through the exchange of virtual mesons $\sigma, \omega, \rho_3$ and photons (see Table.1). In principle one should also include into the description the contribution from the pions $\pi^0, \pi^\pm$ with the masses 135 MeV/$c^2$ and 139.6 MeV/$c^2$ respectively. In the RMF theory one works with the parity symmetric single-particle states in a mean-field. This causes the expectation value of the pion to vanishe, as these particles are psedoscalars. This is the reason why pion is not included in the RMF theories. There are however attempts to include contribution from the pions into the RMF framework by assuming that single-particle states in the mean field are not good parity states. As a result, the expectation value of the pion field becomes finite [53]. We review the RMF theory where single-particle states are good parity states.

The starting point is the one-boson exchange Lagrange density [54](p.4)

$$\mathcal{L} = \mathcal{L}_{nucleon} + \mathcal{L}_{meson} + \mathcal{L}_{couple} \tag{26}$$

which consists of the free Lagrangian for the nucleon and meson fields and also the term coupling the nucleon to the mesons. The difficulty of solving the full field-theoretic problem

Table 1: Rest masses of the selected mesons together with the spin $J$, parity $\pi$, and isospin T [54].

| meson | $J^\pi$ | T | kind | m[MeV/$c^2$] |
|---|---|---|---|---|
| $\sigma$ | $0^+$ | 0 | scalar | 508.194 |
| $\omega$ | $1^-$ | 0 | vector | 782.501 |
| $\rho_3$ | $1^-$ | 1 | vector | 763.000 |

requires several approximations. Among these is a replacement of the field operators by their expectation values (the mean-field approximation) i.e. $\hat{\sigma} \rightarrow \langle \sigma(\vec{r}) \rangle$ etc. The stationary equations of motion can be derived from the Lagrange density by varying the action $S = \int d^4x \ \mathcal{L}$ with respect to the fields [55]. This results in the Dirac equation for the nucleonic

states in the presence of fields

$$H_D\ \psi_i = \varepsilon_i\ \psi_i \Longrightarrow \begin{pmatrix} m+S+V & \vec{\sigma}\cdot\mathbf{p} \\ \vec{\sigma}\cdot\mathbf{p} & -m-S+V \end{pmatrix} \begin{pmatrix} f \\ g \end{pmatrix}_i = \varepsilon_i \begin{pmatrix} f \\ g \end{pmatrix}_i \tag{27}$$

as well in the equations (Klein-Gordon) describing meson fields [54](p.3)

$$(-\Delta + m_\sigma^2)\sigma(\mathbf{r}) = g_\sigma \rho_s(\mathbf{r}), \tag{28}$$

$$(-\Delta + m_\omega^2)\omega(\mathbf{r}) = g_\omega \rho(\mathbf{r}), \tag{29}$$

$$(-\Delta + m_\rho^2)\rho_3(\mathbf{r}) = g_\rho(\rho_n(\mathbf{r}) - \rho_p(\mathbf{r})), \tag{30}$$

$$-\Delta A_0(\mathbf{r}) = e\rho_c(\mathbf{r}), \tag{31}$$

where $\Delta \equiv \partial_\mu \partial^\mu = (\partial_t)^2 - \vec{\nabla}^2$. The single particle wave-functions $\psi_i$ in Eq.(27) are four-dimensional spinors describing stationary nucleonic states with index i and single-particle energy $\varepsilon_i$, where $\vec{\sigma} = (\sigma_1, \sigma_2, \sigma_3)$ is a vector composed of Pauli spin matrices. The Potentials S and V are defined as

$$S = g_\sigma \sigma(\mathbf{r}), \tag{32}$$

$$V = g_\omega \omega(\mathbf{r}) + g_\rho \rho_3(\mathbf{r}) + A_0(\mathbf{r}). \tag{33}$$

The meson fields $\sigma(\mathbf{r}), \omega(\mathbf{r}), \rho_3(\mathbf{r})$ in Eqs. (28-31) are classical fields (potentials) with the nucleonic densities as sources, and the nucleons move freely in the mean-field generated by the exchange of mesons and photons. The above model contains several free parameters e.g. nucleon mass $m$, meson masses $m_\sigma, m_\omega, m_\rho$ whose experimental values are known and also coupling constants $g_\sigma, g_\omega, g_\rho$, which can all be fitted, altough with the large widths, to the properties of known nuclei [54]. The set of equations (27-31) constitutes a self-consistent problem where the many-body Dirac equations and the Klein-Gordon equations for the meson fields are coupled via densities calculated as [54]

$$\rho(\mathbf{r}) = \sum_{i=1}^{A} \psi_i^+ \psi_i = \sum_{i=1}^{A} f_i^+(\mathbf{r}) f_i(\mathbf{r}) + g_i^+(\mathbf{r}) g_i(\mathbf{r}), \tag{34}$$

$$\rho_s(\mathbf{r}) = \sum_{i=1}^{A} \bar{\psi}_i \psi_i = \sum_{i=1}^{A} f_i^+(\mathbf{r}) f_i(\mathbf{r}) - g_i^+(\mathbf{r}) g_i(\mathbf{r}). \tag{35}$$

The density $\rho$ is the usual density, $\rho_s$ is the scalar density, $\rho_n, \rho_p$ are neutron and proton densities and $\rho_c$ is the charge density distribution.

In order to describe properly the properties of nuclei the RMF model needs several improvements, yet the basic assumptions and equations remain the same. In Ref. [54] Lalazissis et al. present results for the 1315 even-even nuclei with $10 \leq Z \leq 98$. While the model works pretty well for nuclei close to the $\beta$ stability line, it, among other things, does not predict correctly properties in the vicinity of the neutron dripline (see secs: 5.1,5.2 ). This is due to the very well known shortcoming of the simplistic BCS model [56] used to describe the pairing interaction in $\mathcal{L}_{nucleon}$.

The proper description of the exotic nuclei necessities a unified and self-consistent treatment of mean-field and pairing correlations, which can be done in the Relativistic Hartree-Bogoliubov (RHB) framework [57, 58, 59, 60, 61, 62]. In the Hartree approximation for the self-consistent mean-field, the relativistic Hartree-Bogoliubov equations read [61, 62]

$$\underbrace{\begin{pmatrix} \hat{H}_D - m - \lambda & \hat{\Delta} \\ -\hat{\Delta}^* & -(\hat{H}_D^* - m - \lambda) \end{pmatrix}}_{\hat{H}_{RHB}} \begin{pmatrix} U_k(\mathbf{r}) \\ V_k(\mathbf{r}) \end{pmatrix} = E_k \begin{pmatrix} U_k(\mathbf{r}) \\ V_k(\mathbf{r}) \end{pmatrix} \tag{36}$$

where $\hat{h}_D$ is the single-nucleon Dirac Hamiltonian (Eq. 27), $\lambda$ is the Fermi level, and m is the nucleon mass. The generalized single-nucleon Hamiltonian $\hat{H}_{RHB}$ contains two average potentials: the self consistent mean field $\hat{\Gamma} = \hat{H}_D - m - \lambda$ and the pairing field $\hat{\Delta}$. The column vectors denote the quasiparticle wave functions from which the densities are calculated, and $E_k$ are the quasiparticle energies. Similarly as in case of solution of the set of equations (27-31), the RHB equations are solved self-consistently, where the sources for the Klein-Gordon equations for the meson fields are calculated from the eigenstates of the RHB equations. A detailed description of the relativistic Hartree-Bogoliubov model for spherical and deformed nuclei can be found in Refs. [58, 60].

CHAPTER II

# NUCLEAR HAMILTONIAN

Quoting the authors of Ref. [44] "The physical world consists of interacting many-particle systems". This work concentrates on the non-relativistic description of the atomic nucleus. Such an approximation is justified by the fact the nucleon inside the atomic nucleus moves at non-relativistic speed. This can be seen from Fig. 11, where we depict the neutron single-particle potential for the neutron-rich $^{112}$Zr nucleus. As we compare the rest mass of the neutron ( $\approx$939.5 MeV/$c^2$) and the depth of the neutron potential we can draw the conclusion that neutron moves with non-relativistic velocities. Therefore is valid to

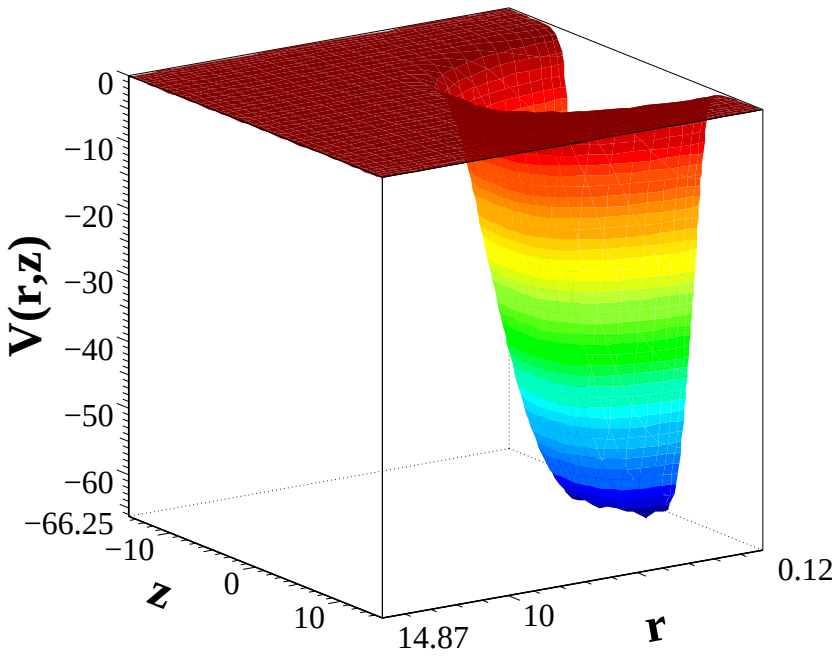


Figure 11: The neutron single-particle potential for the $^{112}$Zr isotope.

describe nuclear forces by potentials under the additional assumption that no new particles

are created from the vacuum [47].

### 2.1 The free $V_{NN}$ nucleon-nucleon interaction .

The free N-N potential can be derived in essentially two different ways: its mathematical structure can be inferred from general symmetry principles, as first pointed in 1941 by Eisenberg and Wigner [63]. We follow here the treatment in the textbook by Ring and Schuck [46]. An alternative approach is the derivation of $V_{NN}$ from free meson-exchange theory. We start with a brief review of the first approach. The two body $V_{NN}$ nuclear potential in coordinate representation depends on the position vectors $\vec{r}_1, \vec{r}_2$, momenta $\vec{p}_1, \vec{p}_2$, spin vectors $\vec{\sigma}_1, \vec{\sigma}_2$ also on an isospin $\vec{\tau}_1$ and $\vec{\tau}_2$ of the two interacting nucleons

$$V_{NN} \equiv V_{NN}(\vec{r}_1, \vec{r}_2, \vec{p}_1, \vec{p}_2, \vec{\sigma}_1, \vec{\sigma}_2, \vec{\tau}_1, \vec{\tau}_2). \tag{37}$$

Potential $V_{NN}$ must obey several symmetries [46]:

- Permutation invariance. Invariance under an exchange of the coordinates

$$V_{NN}(\vec{r}_1, \vec{r}_2, \vec{p}_1, \vec{p}_2, \vec{\sigma}_1, \vec{\sigma}_2, \vec{\tau}_1, \vec{\tau}_2) = V_{NN}(\vec{r}_2, \vec{r}_1, \vec{p}_2, \vec{p}_1, \vec{\sigma}_2, \vec{\sigma}_1, \vec{\tau}_2, \vec{\tau}_1). \tag{38}$$

- Translational invariance. Potential depends only on relative coordinate $\vec{r} = \vec{r}_1 - \vec{r}_2$

$$V_{NN} \equiv V_{NN}(\vec{r}, \vec{p}_1, \vec{p}_2, \vec{\sigma}_1, \vec{\sigma}_2, \vec{\tau}_1, \vec{\tau}_2). \tag{39}$$

- Galilean invariance. Potential depends only on relative momentum $\vec{p}= \frac{1}{2}(\vec{p}_1 - \vec{p}_2)$

$$V_{NN} \equiv V_{NN}(\vec{r}, \vec{p}, \vec{\sigma}_1, \vec{\sigma}_2, \vec{\tau}_1, \vec{\tau}_2). \tag{40}$$

- Isobaric invariance. Nuclear Force is independent of the charge of nucleons ( invariance under rotation in isospin space) . Only isospin scalars are allowed

$$V_{NN} \approx \vec{\tau}_1 \cdot \vec{\tau}_2. \tag{41}$$

- Parity invariance. Invariance under space reflection.

$$V_{NN}(\vec{r}, \vec{p}, \vec{\sigma}_1, \vec{\sigma}_2, \vec{\tau}_1, \vec{\tau}_2) = V_{NN}(-\vec{r}, -\vec{p}, \vec{\sigma}_1, \vec{\sigma}_2, \vec{\tau}_1, \vec{\tau}_2). \tag{42}$$

- Time reversal invariance. Physical observables do not depend on the direction of time.

$$V_{NN}(\vec{r},\vec{p},\vec{\sigma}_1,\vec{\sigma}_2,\vec{\tau}_1,\vec{\tau}_2) = V_{NN}(\vec{r},-\vec{p},-\vec{\sigma}_1,-\vec{\sigma}_2,\vec{\tau}_1,\vec{\tau}_2). \tag{43}$$

  Only even number of products involving $\vec{p}$ and $\vec{\sigma}_i$ are allowed.

- Rotational invariance in coordinate space.

The total angular momentum of the N-N system must be conserved ( invariance under rotation in a combined configuration and spin space, implies only scalar products) . The only allowed scalars invariant under parity and time reversal transformation are [64]

$$V_{NN} \propto r^2 = |\vec{r}|^2, \vec{\sigma}_1 \cdot \vec{\sigma}_2, \vec{\sigma}_i \cdot \vec{r}, \vec{\sigma}_i \cdot (\vec{r} \times \vec{p}). \tag{44}$$

It is valid to consider first velocity independent forces (static) [15] as the first approximation. Such an approximation is valid at low energies. Additionally it can be assumed that force is central (depends only of the magnitude $r \equiv |\vec{r}|$ of the vector $\vec{r}$ ) . The most general potential, which satisfies rotational, parity, isobaric (Eq. 41), and time reversal invariance can be symbolically written as

$$V_{NN} \propto \begin{bmatrix} 1 \\ \vec{\sigma}_1 \cdot \vec{\sigma}_2 \end{bmatrix} \times \begin{bmatrix} 1 \\ \vec{\tau}_1 \cdot \vec{\tau}_2 \end{bmatrix} \times f(r), \tag{45}$$

where $f(r)$ denotes arbitrary radial functions. Symbol "$\times$" means that we have to form all of the possible combinations. More explicitly, we can write potential $V_{NN}$ as [15]

$$V_{NN} \approx V_c(r) + W_c(r)\vec{\tau}_1 \cdot \vec{\tau}_2 + [V_{sc}(r) + W_{sc}(r)\vec{\tau}_1 \cdot \vec{\tau}_2](\vec{\sigma}_1 \cdot \vec{\sigma}_2),$$

where $V_c, W_c, V_{sc}, W_{sc}$ are arbitrary radial functions that cannot be determined from the invariance principles. The velocity-independent nuclear force doesn't form a complete description of the $V_{NN}$ interaction . There is experimental evidence of a need to include in the potential velocity-dependent components [44]. As we can see from Eq. 44 we have already formed the velocity dependent component $\vec{\sigma}_i \cdot (\vec{r} \times \vec{p})$. Additionally, the requirement that potential $V_{NN}$ obeys permutation invariance (Eq. 38) implies that the spin dependence must enter symmetrically [15]

$$\vec{S} = \frac{1}{2}(\vec{\sigma}_1 + \vec{\sigma}_2), \tag{46}$$

where $\vec{S}$ is the total spin. Thus, the velocity dependent term in $V_{NN}$ potential has the following form

$$\vec{L}\cdot\vec{S} = \frac{1}{2}(\vec{r}\times\vec{p})(\vec{\sigma}_1+\vec{\sigma}_2). \tag{47}$$

Nucleon-nucleon scattering experiments also give a hint of the existence of non central terms. Particularly, the measured quadrupole moment of the deuteron cannot be explained by a central force [64]. See a candidate for the tensor force $(\sigma_i\cdot\vec{r})$ in the Eq. 44. The only possible combination that doesn't violate parity and time reversal invariance must be proportional to $(\vec{r}\cdot\vec{\sigma}_1)(\vec{r}\cdot\vec{\sigma}_2)$. The tensor force is usually introduced in terms of the following operator [46]

$$S_{12} = \frac{3(\vec{r}\cdot\vec{\sigma}_1)(\vec{r}\cdot\vec{\sigma}_2)}{r^2} - \vec{\sigma}_1\cdot\vec{\sigma}_2. \tag{48}$$

Above considerations leave us with the velocity-dependent non central nucleon-nucleon interaction that can be symbolically written as

$$V_{NN} \propto \begin{bmatrix} 1 \\ \vec{\sigma}_1\cdot\vec{\sigma}_2 \end{bmatrix} \times \begin{bmatrix} 1 \\ \vec{\tau}_1\cdot\vec{\tau}_2 \\ S_{12} \\ \vec{L}\cdot\vec{S} \end{bmatrix} \times f(r), \tag{49}$$

or equivalently

$$\begin{aligned} V_{NN} \approx [V_c(r) + W_c(r)\vec{\tau}_1\cdot\vec{\tau}_2] + [V_{sc}(r) + W_{sc}(r)\vec{\tau}_1\cdot\vec{\tau}_2](\vec{\sigma}_1\cdot\vec{\sigma}_2) + \\ [V_T(r) + W_T(r)\vec{\tau}_1\cdot\vec{\tau}_2]S_{12} + [V_{LS}(r) + W_{LS}(r)\vec{\tau}_1\cdot\vec{\tau}_2](\vec{L}\cdot\vec{S}). \end{aligned} \tag{50}$$

The radial functions in the Eq. 50 cannot be determined from the invariance principles. They can be obtained from a fit to experimental data or from meson exchange theories.

In 1935, Yukawa postulated that N-N interaction can be understood by the virtual exchange of pions; the original theory involved a scalar (spin 0) meson and was later generalized to vector mesons (spin 1). At large distances the problem can be described by the relativistic Klein-Gordon equation for pions (spin-less particles) and relativistic Dirac equations for nucleons [65]. One calculates the T-matrix for one-pion exchange; in the static limit, this quantity is identical to the N-N interaction $V_{NN}(\vec{q})$. By inverse Fourier transform,

one obtains [66] the so-called one-pion exchange potential (OPEP)

$$V_{OPEP}(\vec{r},\vec{\sigma}_1,\vec{\sigma}_2,\vec{\tau}_1,\vec{\tau}_2)=\frac{-g_0^2}{4\pi}\left(\frac{\mu}{2M}\right)^2\frac{1}{3}(\vec{\tau}_1\cdot\vec{\tau}_2)\left(\vec{\sigma}_1\cdot\vec{\sigma}_2+S_{12}\left(1+\frac{3}{\mu r}+\frac{3}{(\mu r)^2}\right)\right)\frac{e^{-\mu r}}{r}, \tag{51}$$

where $\mu$ and $M$ are respectively the inverse Compton wavelengths of pion and nucleon, $g_0$ stands for pion-nucleon coupling. Recently, modern N-N potentials have been developed, based on meson exchange theories, which fit all available N-N scattering data and properties of the deutron. Among these are the "Argonne-V18" potential [63], the "Nijmegen-potential" [67], and the "CD-Bonn potential" [68]. As a result of two meson and heavier meson exchange, $V_{NN}$ becomes strongly repulsive at small distances ($r\approx 0.5fm$).

### 2.2 Effective N-N interaction (Brückner's G-matrix) inside the nuclear medium

The nucleon-nucleon interaction is significantly modified compared to the free N-N interaction. The presence of other particles in the nuclear medium allows for non-conservation of the energy and momentum of the N-N pairs (energy and momentum can be transfered to other particles). Another new feature compared to the two body system is that not all of the scattering states are available. Particularly, only scattering states above the Fermi level ($E_n > E_f$) are allowed, as all of the states below the Fermi sea are occupied. To illustrate the features of the N-N system inside the medium we analyze first the scattering matrix $T$ for two free nucleons, which is governed by the Lippman-Schwinger equation [46]

$$T^E_{\vec{k}_1,\vec{k}_2,\vec{k}'_1,\vec{k}'_2}=\bar{v}_{\vec{k}_1,\vec{k}_2,\vec{k}'_1,\vec{k}'_2}+\frac{1}{2}\sum_{\vec{p}_1,\vec{p}_2}\bar{v}_{\vec{k}_1,\vec{k}_2,\vec{p}_1,\vec{p}_2}\frac{1}{E-\left(\frac{\vec{p}_1^{\,2}}{2m}\right)-\left(\frac{\vec{p}_2^{\,2}}{2m}\right)+i\eta}T^E_{\vec{p}_1,\vec{p}_2,\vec{k}'_1,\vec{k}'_2}, \tag{52}$$

where $\vec{k}_1,\vec{k}_2$ and $\vec{k}'_1,\vec{k}'_2$ are the momenta of the incoming and outgoing particles respectively, and $E$ is the total energy of the N-N system. In the summation there are no restrictions for the momenta $\vec{p}_1,\vec{p}_2$ and we have conserved energy and momenta.

$$\vec{k}_1+\vec{k}_2=\vec{k}'_1+\vec{k}'_2. \tag{53}$$

In the operator form Eq. 52 is often written as [46]

$$T=\bar{v}+\bar{v}\frac{1}{E-H_0}T\Rightarrow T=\frac{\bar{v}}{1-\bar{v}(E-H_0)^{-1}}. \tag{54}$$

where $\bar{v}$ represents free N-N interaction (Eq. 50), and

$$H_0 = \frac{\vec{p}_1^2}{2m} + \frac{\vec{p}_2^2}{2m}. \tag{55}$$

In a similar way the N-N scattering inside nuclear medium is governed by the analogous equations (Bethe-Goldstone) for an analog of matrix $T$ so-called Brückner "G-matrix" $G$ [46]. We can immediately write down the equation for matrix $G$ by substituting in the Lippman-Schwinger (Eq. 52) plane waves with shell model states ($\vec{k}_1, \vec{k}_2 \to m, n$ ), including in summation only states above Fermi Energy ($E_n > E_f$), and removing the restrictions for the conservation of energy and momentum $\vec{k}_1 + \vec{k}_2 \neq \vec{k}_1' + \vec{k}_2'$. The Bethe-Goldstone equation for Brücker's G-matrix $G$ has the following form [69]

$$G^E_{ab,cd} = \bar{v}_{ab,cd} + \frac{1}{2} \sum_{m,n>E_f} \bar{v}_{ab,mn} \frac{1}{E - E_m - E_n + i\eta} G^E_{mn,cd}, \tag{56}$$

where $ab \ldots mn$ and $E_n, E_m$ are shell-model indices and energies respectively. The potential $\bar{v}$ is a free N-N potential (Eq. (50). We can see that the effective N-N interaction can be obtained from the bare N-N interaction if only the shell-model energies $E_n, E_m$ are known. Symbolically matrix $G$ can be written as [46]

$$G = \bar{v} + \bar{v} \frac{Q_F}{E - H_0} G \Rightarrow G = \frac{\bar{v}}{1 - \bar{v} Q_F (E - H_0)^{-1}}, \tag{57}$$

where

$$Q_F = \sum_{(m<n)>E_f} |mn\rangle\langle mn| \tag{58}$$

is a projection operator excluding occupied states ("Pauli Blocking"). The Equations 52 and 56 look very similar and one can be mislead that they posses the same properties. The fact that energy and momentum in case of a scattering of free nucleons is conserved ("'on-shell" scattering) and not conserved in the case of presence of medium ("off-shell" scattering) attributes to the completely different behaviors at small distances ( $|\vec{r}_1 - \vec{r}_2| \approx 0, \bar{v} \to \infty$). The "on-shell" scattering case introduces a singularity in (Eq. 54), and therefore at small distances interaction is infinite. By contrast the matrix $G$ remains finite, because in the "off-shell" scattering the denominator in (Eq. 57) does not have a zero. At large distances ( $|\vec{r}_1 - \vec{r}_2| \to \infty, \bar{v} \to 0$) both matrices have the same asymptotic behavior and go to zero

as the potential $\bar{v}$ also goes to zero. All of the mentioned asymptotic behaviors have been illustrated in Fig. 12 [47]. Shown is the radial part, $V_T(r)$, of the free N-N tensor interaction

$$V_T(r)S_{12}$$

(see Eq. 50) and the corresponding effective interaction. We observe that both interactions are identical at distances larger than about 1fm. However, at smaller distances, the effective interaction (solid curve) remains finite and is much weaker than the free interaction (dotted curve).

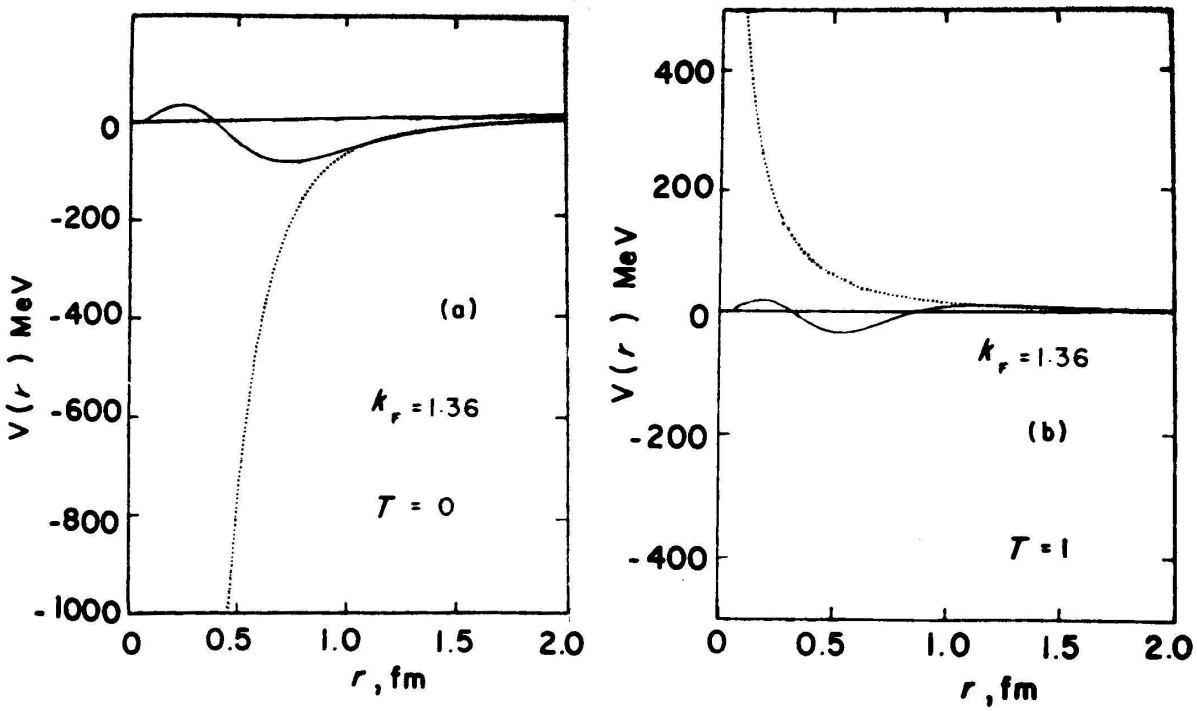


Figure 12: Tensor component of Reid Soft-Core potential. Shown are the effective interaction (solid line) and bare N-N interaction (dotted curve) vs. distance $r$. Figures (a) and (b) correspond to a different total isospin T=0,1. Plots were made at $k_F = 1.36$ fm$^{-1}$ [70, 71, 72].

## 2.3 Phenomenological effective N-N interactions.

In practice solving the Bethe-Goldstone equation (56) is rather difficult and requires several approximations. Another drawback is not too good agreement with the experimental data even if calculations are feasible [46]. As a remedy we can use phenomenological forces, with several free parameters that need to be adjusted to reproduce the experimental data. One of the most widely used effective-interaction (used also by our group) is the so-called Skyrme interaction [73]. To see how the Skyrme force can be derived it is convenient to transform an arbitrary two body local potential to momentum space using Fourier transform [46]

$$\langle \mathbf{k}|V|\mathbf{k}'\rangle = \frac{1}{(2\pi\hbar)^3}\int e^{\frac{-i}{\hbar}(\mathbf{k}-\mathbf{k}')\mathbf{r}}V(\mathbf{r})d^3\mathbf{r}, \tag{59}$$

where $\mathbf{r} = |\vec{r}_1 - \vec{r}_2|$ is the relative distance, $\mathbf{k} = |\vec{k}_1 - \vec{k}_2|$, $\mathbf{k}' = |\vec{k}'_1 - \vec{k}'_2|$ are relative momenta of two nucleons before and after collision. We know that the nuclear interaction is short ranged. The first approximation to the potential $V(\mathbf{r})$ can be then the $\delta$ function $(V(\mathbf{r}) \approx \delta(\mathbf{r}))$ . This leads to a trivial constant dependence in momentum space. One has to use more realistic finite range potential, which translates to a non trivial momentum dependence. To achieve this we o expand potential (Eq. 59) in powers of momenta and retain only terms up the second order (low momentum expansion valid at low energies) and keep only rotationally invariant terms [46]

$$(2\pi\hbar)^3\langle \mathbf{k}|V|\mathbf{k}'\rangle \approx V_0 + V_1(\mathbf{k'^2} + \mathbf{k^2}) + V_2\mathbf{k}\cdot\mathbf{k}' + \dots. \tag{60}$$

Using the inverse Fourier transformation, we find the equivalent potential in coordinate-space

$$V(\mathbf{r}) = V_0\delta(\mathbf{r}) + V_1\left(\hat{\mathbf{k}}^{\mathbf{2}}\delta(\mathbf{r}) + \delta(\mathbf{r})\hat{\mathbf{k}}'^{\mathbf{2}}\right) + V_2\hat{\mathbf{k}}'\delta(\mathbf{r})\hat{\mathbf{k}}, \tag{61}$$

where the derivative operators (relative momenta) $\hat{k}$ and $\hat{k}'$ are defined by

$$\hat{\mathbf{k}} = \frac{1}{2i}(\nabla_{\mathbf{1}} - \nabla_{\mathbf{2}}), \tag{62}$$

$$\tag{63}$$

acting on the right and

$$\hat{\mathbf{k}}' = -\frac{1}{2i}(\nabla_{\mathbf{1}} - \nabla_{\mathbf{2}}), \tag{64}$$

$$\tag{65}$$

Table 2: Skyrme parameters for SLy4 force[49, 76] in units of ( MeV fm$^3$) for $t_0$ through $t_3$ and $W_0$ parameters, remaining ones are dimensionless.

| $t_0$ | $t_1$ | $t_2$ | $t_3$ | $W_0$ | $x_0$ | $x_1$ | $x_2$ | $x_3$ | $\alpha$ |
|---|---|---|---|---|---|---|---|---|---|
| -2488.913 | 486.818 | -546.395 | 13777.0 | 123 | 0.8340 | -0.3438 | -1.0 | 1.3540 | 1/6 |
| $\frac{\hbar^2}{2m}$ | | | | | | | | | |
| 20.73553 | | | | | | | | | |

acting on the left. The potential (Eq. 60) has been also supplemented by the addition of a spin-orbit term as (note rotational invariance ) [74, 73]

$$\vec{L}\cdot\vec{S}(\mathbf{k},\mathbf{k}') \equiv iW_0(\vec{\sigma}^{(1)}+\vec{\sigma}^{(2)})\cdot(\mathbf{k}\times\mathbf{k}'). \tag{66}$$

Finally, Skyrme[73] introduced also the three body interaction term of the very simple form

$$V(\vec{r}_1,\vec{r}_2,\vec{r}_3) = t_3\delta(\vec{r}_1-\vec{r}_2)\delta(\vec{r}_2-\vec{r}_3), \tag{67}$$

which for even-even nuclei corresponds to a two body density dependent [74] interaction. The Skyrme interaction contains several free parameters, which need to fitted to a bulk properties of known nuclei (rms-radii, binding energy etc. ). The widely used form of this density-dependent two-body effective interaction has the following form [73, 75]

$$\begin{aligned}
V_{12}(\mathbf{r}) &= t_0(1+x_0\hat{P}_\sigma)\delta(\mathbf{r}) && (68)\\
&+ \frac{1}{2}t_1(1+x_1\hat{P}_\sigma)\left(\hat{\mathbf{k}}'^{\mathbf{2}}\delta(\mathbf{r})+\delta(\mathbf{r})\hat{\mathbf{k}}^{\mathbf{2}}\right)+t_2(1+x_2\hat{P}_\sigma)\hat{\mathbf{k}}'\cdot\delta(\mathbf{r})\hat{\mathbf{k}} && (69)\\
&+ iW_0(\hat{\sigma}^{(1)}+\hat{\sigma}^{(2)})\cdot(\hat{\mathbf{k}}'\times\delta(\mathbf{r})\hat{\mathbf{k}}) && (70)\\
&+ \frac{1}{6}t_3(1+x_3\hat{P}_\sigma)\rho^\alpha\delta(\mathbf{r}), && (71)
\end{aligned}$$

where $\hat{P}_\sigma$ is the spin-exchange operator. The first term (Eq. 68) describes the pure $\delta$ force. The second one (Eq. 69) approximates the finite range force and the third (Eq. 70) represents a two body spin-orbit interaction. The last term introduces the density dependence, which describes the many-body effects. The properties of the nucleons in the nucleus are influenced by the state of other nucleons in the system. For the even-even nuclei the three body term [46] reduces to the two-body interaction. In our recent calculations

performed with the HFB-2D-LATTICE code we have used the so-called SLy4 force (Table. 2).

# CHAPTER III

# HARTREE-FOCK-BOGOLIUBOV THEORY

The next chapter concentrates on the Hartree-Fock-Bogoliubov theory and the methods of solution of the HFB equations in coordinate-space.

## 3.1 Derivation of the HFB equations

We start from the many-body Hamiltonian in the second quantization form [44]

$$\begin{aligned}\hat{H} = & \sum_{k,l=1}^{\infty} \langle k|t|l\rangle \hat{c}_k^\dagger \hat{c}_l + \frac{1}{2} \sum_{k,l,m,n=1}^{\infty} \langle kl|v^{(2)}|mn\rangle \hat{c}_k^\dagger \hat{c}_l^\dagger \hat{c}_n \hat{c}_m + \\ & \frac{1}{6} \sum_{i,j,k,l,m,n=1}^{\infty} \langle ijk|v^{(3)}|lmn\rangle \hat{c}_i^\dagger \hat{c}_j^\dagger \hat{c}_k^\dagger \hat{c}_n \hat{c}_m \hat{c}_l,\end{aligned} \tag{72}$$

where e.g. $|i\rangle$ is the single particle basis with the associated ladder operators $\hat{c}_i^\dagger$, $t$ stands for the one-body kinetic energy operator from Eq.( 16), $\hat{v}^{(2)}$ and $\hat{v}^{(3)}$ are two and three body operators (Eq. 16). The standard approach [46, 48] is to apply the Wicks's theorem to the Hamiltonian Eq. (72) to arrive at [48]

$$E_0^{HFB} = \langle \Phi_0^{HFB}|\hat{H}|\Phi_0^{HFB}\rangle = \sum_{k,l} t_{kl}\rho_{lk} + \frac{1}{2} \sum_{k,l,m,n} \bar{v}_{klmn}^{(2)} \left(\rho_{nl}\rho_{mk} + \frac{1}{2}\kappa_{mn}\kappa_{kl}^*\right), \tag{73}$$

or equivalently

$$E_0 = \sum_{k,l} \left(t_{kl}\rho_{lk} + \frac{1}{2}V_{kl}^{(1)}\rho_{lk} + \frac{1}{2}\Delta_{kl}\kappa_{lk}^*\right), \tag{74}$$

where we have defined the mean-field $V_{kl}^{(1)}$ and paring field $\Delta_{kl}$ as [48]

$$\langle k|V^{(1)}|m\rangle \equiv V_{km}^{(1)} \equiv \sum_{l,n} \bar{v}_{klmn}^{(2)}\rho_{nl}, \tag{75}$$

$$\langle kl|\Delta\rangle \equiv \Delta_{kl} \equiv \frac{1}{2}\sum_{m,n} \bar{v}_{klmn}^{(2)}\kappa_{mn}, \tag{76}$$

The Hamiltonian $H_0$ is expressed through the normal matrix $\rho_{lk}$ and the pairing tensor $\kappa_{lk}$, which on the other hand are the following contractions of the operators $\hat{c}_k$ and $\hat{c}_l^\dagger$ [48, 46]

$$\rho_{lk} = \langle \Phi_0^{HFB}|\hat{c}_k^\dagger \hat{c}_l|\Phi_0^{HFB}\rangle \equiv \underbrace{\hat{c}_k^\dagger \hat{c}_l}, \tag{77}$$

$$\kappa_{kl} = \langle \Phi_0^{HFB} | \hat{c}_l \hat{c}_k | \Phi_0^{HFB} \rangle \equiv \underbrace{\hat{c}_l \hat{c}_k}, \tag{78}$$

$$\kappa_{kl}^* = \langle \Phi_0^{HFB} | \hat{c}_k^\dagger \hat{c}_l^\dagger | \Phi_0^{HFB} \rangle \equiv \underbrace{\hat{c}_k^\dagger \hat{c}_l^\dagger}. \tag{79}$$

The ground state energy (Eq. 74) has relatively simple form because of the application of the Hartree-Fock-Bogoliubov transformation [77] of the operators $\hat{c}_i, \hat{c}_j^\dagger$ to the so-called quasiparticle operators $\hat{\beta}_i, \hat{\beta}_j^\dagger$. The new quasiparticle operators define the HFB ground state $\Phi_0^{HFB}$ - which is the quasiparticle vacuum state,

$$\hat{\beta} | \Phi_0^{HFB} \rangle = 0. \tag{80}$$

The Hartree-Fock-Bogoliubov transformation is canonical , therefore it preserves the commutation relations of the operators $\hat{c}_i, \hat{c}_j^\dagger$ and is defined as [46]

$$\hat{\beta}_j^\dagger = \sum_k \left( U_{kj} \hat{c}_k^+ + V_{kj} \hat{c}_k \right), \tag{81}$$

$$\hat{\beta}_i = \sum_k \left( U_{ki}^* \hat{c}_k + V_{ki}^* \hat{c}_k^+ \right), \tag{82}$$

or symbolically

$$\begin{pmatrix} \hat{\beta} \\ \hat{\beta}^\dagger \end{pmatrix} = \begin{pmatrix} U^\dagger & V^\dagger \\ V^T & U^T \end{pmatrix} \begin{pmatrix} \hat{c} \\ \hat{c}^\dagger \end{pmatrix}. \tag{83}$$

We can easily invert the transformation in the Eqs. (81,82). After inserting the result into the Eqs. (77,78) the matrices $\rho_{ij}$ and $\kappa_{ij}$ can be expressed now alternatively in terms of the coefficients $V$ and $U$

$$\rho_{lk} = (V^* V^T)_{lk}, \tag{84}$$

$$\kappa_{lk} = (V^* U^T)_{lk}. \tag{85}$$

The Hartree-Fock-Bogoliubov equations in the energy representation can be obtained in an analogous way in the case of the derivation of the Hartree-Fock (HF) equations [48]. In case of HF the energy functional depends only on the density matrix $\rho_{ij}$. One obtains the Hartree-Fock (HF) equations by varying the energy functional with respect to $\rho_{ij}$

$$\delta|_{\rho_{ij}} [E_0^{HF}(\rho_{ij}) - \mathrm{trace}\{\Lambda(\rho^2 - \rho)\}] = 0, \tag{86}$$

where $\Lambda$ is a Lagrange multiplier matrix. After variation the Hartree-Fock equation has a very simple form

$$[h, \rho] = 0, \tag{87}$$

where

$$\hat{h} \equiv \hat{t} + \hat{V}^{(1)}. \tag{88}$$

In case of HFB theory, the matrix $\rho$ in Eq. (86) is generalized to the matrix $\Re$, which is both Hermitian and idempotent

$$\Re^{\dagger} = \Re, \Re^2 = \Re. \tag{89}$$

The Matrix $\Re$ is defined as [48, 46]

$$\Re \equiv \begin{pmatrix} \rho & \kappa \\ -\kappa^* & 1-\rho^* \end{pmatrix}. \tag{90}$$

The HFB variational principle is supplemented with additional Lagrange multiplier $\lambda$, which plays the role of the chemical potential (Fermi level ) [48, 46]

$$\delta|_{\Re}[E_0^{HFB}(\Re) - \lambda\hat{N} - \mathrm{trace}\{\Lambda(\Re^2 - \Re)\}] = 0, \tag{91}$$

where $\hat{N}$ denotes the particle number operator, and again we arrive with the very simple compact form of the Hartree-Fock-Bogoliubov equations

$$[\mathcal{H}, \Re] = 0, \tag{92}$$

where [48]

$$\mathcal{H} \equiv \begin{pmatrix} h-\lambda & \Delta \\ -\Delta^* & -(h-\lambda)^* \end{pmatrix}. \tag{93}$$

The introduction of the another additional Lagrange multiplier is implied by the fact that the particle number is not conserved in the HFB approximation (quasiparticle vacuum is not an eigenstate of the particle number operator) [46, 48]. Finally, from the commutator Eq. (92) , matrix Eq. (90) and relations Eq. (89) we can write down the Hartree-Fock Bogoliubov equations in the energy representation [48, 46]

$$\mathcal{H}\begin{pmatrix} U_\alpha \\ V_\alpha \end{pmatrix} = E_\alpha \begin{pmatrix} U_\alpha \\ V_\alpha \end{pmatrix}, \tag{94}$$

$$\mathcal{H}\begin{pmatrix} V_\alpha^* \\ U_\alpha^* \end{pmatrix} = -E_\alpha \begin{pmatrix} V_\alpha^* \\ U_\alpha^* \end{pmatrix}. \tag{95}$$

It should be noted the generalized matrix $\Re$ as well as the Hamiltonian $\mathcal{H}$ possess the two simultaneous eigenvectors corresponding to positive and negative quasiparticle energy, $\pm E_\alpha$. In Eq. (94) only the choice of the eigenvectors corresponding to the the positive $+E_\alpha$ quasiparticle energies was made. It is forbidden to choose positive and negative quasiparticle energies at the same time, otherwise it is impossible to satisfy the anti-commutation relations for the operators $\hat{\beta}_\alpha$ and $\hat{\beta}^\dagger_\alpha$ [46].

### 3.1.1 HFB equations in coordinate space.

In order to solve the HFB equation on the spatial lattice the Eq. (94) needs to be transformed from the energy representation to the coordinate representation by inserting completeness relation of the form $\int d^3r' \sum_{\sigma'} |\mathbf{r}'\sigma'\rangle\langle\mathbf{r}'\sigma'|$ and closing from the left by Dirac's bra $\langle\mathbf{r}\sigma|$ to arrive at [78]

$$\int d^3r' \sum_{\sigma',q'} \begin{pmatrix} h^q(\mathbf{r},\sigma,q,\mathbf{r}',\sigma',q') & \Delta^q(\mathbf{r},\sigma,q,\mathbf{r}',\sigma',q') \\ -\Delta^{*q}(\mathbf{r},\sigma,q,\mathbf{r}',\sigma',q') & -h^{*q}(\mathbf{r},\sigma,q,\mathbf{r}',\sigma',q') \end{pmatrix} \begin{pmatrix} U^q_\alpha(\mathbf{r}',\sigma',q') \\ V^q_\alpha(\mathbf{r}',\sigma',q') \end{pmatrix} = \tag{96}$$

$$\begin{pmatrix} E^q_\alpha + \lambda^q & 0 \\ 0 & E^q_\alpha - \lambda^q \end{pmatrix} \begin{pmatrix} U^q_\alpha(\mathbf{r},\sigma,q) \\ V^q_\alpha(\mathbf{r},\sigma,q) \end{pmatrix}. \tag{97}$$

The definition of the quasiparticle wavefunctions $U^q_\alpha(\mathbf{r},\sigma)$ and $V^q_\alpha(\mathbf{r},\sigma)$ is determined by the normal matrix and pairing tensor from Eqs. (84) in the coordinate space, which in the assumed basis $\{\phi_\alpha(\mathbf{r},\sigma)\}$ are expressed in the following way [46]

$$\rho(\mathbf{r}\sigma q,\mathbf{r}'\sigma' q') = \sum_{ij} \rho_{ij}\phi_i(\mathbf{r}\sigma q)\phi^*_j(\mathbf{r}'\sigma' q'), \tag{98}$$

$$\kappa(\mathbf{r}\sigma q,\mathbf{r}'\sigma' q') = \sum_{ij} \kappa_{ij}\phi_i(\mathbf{r}\sigma q)\phi_j(\mathbf{r}'\sigma' q'). \tag{99}$$

The above coordinate space matrices can be conveniently expressed in terms of quasiparticle wavefunctions $U_\alpha(\mathbf{r},\sigma,q)$ and $V_\alpha(\mathbf{r},\sigma,q)$ as

$$\rho(\mathbf{r}\sigma q,\mathbf{r}'\sigma' q') = \sum_{\alpha} V^*_\alpha(\mathbf{r}\sigma q)V_\alpha(\mathbf{r}'\sigma' q'), \tag{100}$$

$$\kappa(\mathbf{r}\sigma q,\mathbf{r}'\sigma' q') = \sum_{\alpha} V^*_\alpha(\mathbf{r}\sigma q)U_\alpha(\mathbf{r}'\sigma' q'), \tag{101}$$

with the quasiparticle wavefunctions defined naturally as ( Eqs. (98-99,84) [79, 78]

$$U_\alpha(\mathbf{r}\sigma q) = \sum_i U_{i\alpha}\phi_i(\mathbf{r}\sigma q), \tag{102}$$

$$V_\alpha(\mathbf{r}\sigma q) = \sum_i V_{i\alpha}\phi_i^*(\mathbf{r}\sigma q). \tag{103}$$

In the HFB formalism, there are two types of quasiparticle wavefunctions, $U_\alpha$ and $V_\alpha$, which are bi-spinors of the form

$$U_\alpha^q(\mathbf{r}) = \begin{pmatrix} U_\alpha^q(\mathbf{r},\uparrow) \\ U_\alpha^q(\mathbf{r},\downarrow) \end{pmatrix}, \quad V_\alpha^q(\mathbf{r}) = \begin{pmatrix} V_\alpha^q(\mathbf{r},\uparrow) \\ V_\alpha^q(\mathbf{r},\downarrow) \end{pmatrix}. \tag{104}$$

In the wavefunctions, the dependence on the quasiparticle energy $E_\alpha$ is denoted by the index $\alpha$ and the isospin dependence by q for simplicity. The HFB Hamiltonian Eq.( 96) is

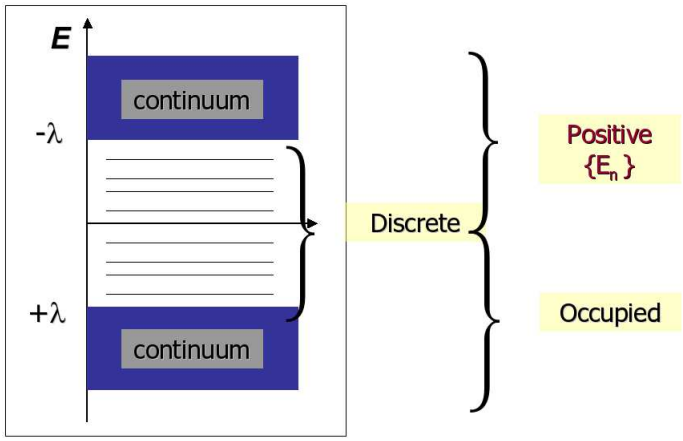


Figure 13: ]
HFB quasiparticle energy spectrum.

constructed from the Hermitian Hartree-Fock Hamiltonian Eq. (88) and the antisymmetric pairing field $\Delta$ (Eq. (76)) [46, 48]. It is possible to replace the antisymmetric pairing field $\Delta$ with the Hermitian pairing Hamiltonian $\tilde{h}$ [80], and to replace the pairing tensor $\kappa$ with the pairing density $\tilde{\rho}$ defined as [81, 80, 82]

$$\tilde{h}(\mathbf{r}\sigma q, \mathbf{r}'\sigma' q) = -2\sigma'\Delta(\mathbf{r}\sigma q, \mathbf{r}' - \sigma' q'), \tag{105}$$

$$\tilde{\rho}(\mathbf{r}\sigma q, \mathbf{r}'\sigma' q) = -2\sigma'\kappa(\mathbf{r}\sigma q, \mathbf{r}' - \sigma' q'). \tag{106}$$

With such definitions the HFB equation( Eq. 96) can be rewritten alternatively as [81, 80,

82]

$$\int d^3r' \sum_{\sigma',q'} \begin{pmatrix} h^q(\mathbf{r},\sigma,q,\mathbf{r}',\sigma',q') & \tilde{h}^q(\mathbf{r},\sigma,q,\mathbf{r}',\sigma',q') \\ \tilde{h}^q(\mathbf{r},\sigma,q,\mathbf{r}',\sigma',q') & -h^q(\mathbf{r},\sigma,q,\mathbf{r}',\sigma',q') \end{pmatrix} \begin{pmatrix} \phi^q_{1,\alpha}(\mathbf{r}',\sigma',q') \\ \phi^q_{2,\alpha}(\mathbf{r}',\sigma',q') \end{pmatrix} = \tag{107}$$

$$\begin{pmatrix} E^q_\alpha + \lambda^q & 0 \\ 0 & E^q_\alpha - \lambda^q \end{pmatrix} \begin{pmatrix} \phi^q_{1,\alpha}(\mathbf{r},\sigma,q) \\ \phi^q_{2,\alpha}(\mathbf{r},\sigma,q) \end{pmatrix}, \tag{108}$$

where the quasiparticle wavefunctions and the densities are defined in the following way

$$\phi^*_{1,\alpha}(\mathbf{r}\sigma q) = \sum_i U_{i\alpha}(2\sigma)\phi_i(\mathbf{r}-\sigma,q), \tag{109}$$

$$\phi_{2,\alpha}(\mathbf{r}\sigma q) = \sum_i V^*_{i\alpha}\phi_i(\mathbf{r}\sigma q), \tag{110}$$

$$\rho(\mathbf{r}\sigma q,\mathbf{r}'\sigma' q') = \sum_\alpha \phi_{2,\alpha}(\mathbf{r}\sigma,q)\phi^*_{2,\alpha}(\mathbf{r}'\sigma' q'), \tag{111}$$

$$\tilde{\rho}(\mathbf{r}\sigma q,\mathbf{r}'\sigma' q') = -\sum_\alpha \phi^*_{2,\alpha}(\mathbf{r}\sigma,q)\phi_{1,\alpha}(\mathbf{r}'\sigma' q'). \tag{112}$$

In the present work, we use Skyrme effective N-N interactions (Chapter 2.3) in the particle mean field Hamiltonian $h$, and a delta interaction in the pairing field Hamiltonian $\tilde{h}$ [82]

$$\tilde{h}(\mathbf{r},\sigma,q,\mathbf{r}',\sigma',q') = \frac{1}{2}V^q_0\tilde{\rho}_q(\mathbf{r})\delta(\mathbf{r}-\mathbf{r}')\delta_{\sigma\sigma'}\delta_{qq'}. \tag{113}$$

These type of the effective interactions are diagonal in isospin space and local in position space,

$$h(\mathbf{r}\sigma q,\mathbf{r}'\sigma' q') = \delta_{q,q'}\ \delta(\mathbf{r}-\mathbf{r}')h^q_{\sigma,\sigma'}(\mathbf{r}), \tag{114}$$

$$\tilde{h}(\mathbf{r}\sigma q,\mathbf{r}'\sigma' q') = \delta_{q,q'}\ \delta(\mathbf{r}-\mathbf{r}')\tilde{h}^q_{\sigma,\sigma'}(\mathbf{r}). \tag{115}$$

Thus, the HFB equation (Eq. 107) reduces to the following structure in spin-space [82]:

$$\begin{pmatrix} (h^q-\lambda^q) & \tilde{h}^q \\ \tilde{h}^q & -(h^q-\lambda^q) \end{pmatrix} \begin{pmatrix} \phi^q_{1,\alpha} \\ \phi^q_{2,\alpha} \end{pmatrix} = E^q_\alpha \begin{pmatrix} \phi^q_{1,\alpha} \\ \phi^q_{2,\alpha} \end{pmatrix} \tag{116}$$

with

$$h^q(\mathbf{r}) = \begin{pmatrix} h^q_{\uparrow\uparrow}(\mathbf{r}) & h^q_{\uparrow\downarrow}(\mathbf{r}) \\ h^q_{\downarrow\uparrow}(\mathbf{r}) & h^q_{\downarrow\downarrow}(\mathbf{r}) \end{pmatrix},\ \tilde{h}^q(\mathbf{r}) = \begin{pmatrix} \tilde{h}^q_{\uparrow\uparrow}(\mathbf{r}) & \tilde{h}^q_{\uparrow\downarrow}(\mathbf{r}) \\ \tilde{h}^q_{\downarrow\uparrow}(\mathbf{r}) & \tilde{h}^q_{\downarrow\downarrow}(\mathbf{r}) \end{pmatrix}\ . \tag{117}$$

The quasiparticle energy spectrum is discrete for $|E| < -\lambda$ and continuous for $|E| > -\lambda$ (Fig. 13) [81]. For even-even nuclei it is customary to solve the HFB equations for positive

quasiparticle energies and consider all negative energy states as occupied in the HFB ground state.

It is generally acknowledged that an accurate theoretical treatment of the pairing interaction is essential for a description of the exotic nuclei [82, 83]. Besides large pairing correlations, the HFB calculations have to face the problem of an accurate description of the continuum states with a large spatial extent. All of these features represent major challenges for the numerical solution.

There are various mean-field methods of solving the non-relativistic HFB equations. Generally, they can be divided into two categories: lattice methods and basis expansion methods. In the lattice approach no region of the spatial lattice is favored over any other region: the well bound, weakly bound and (discretized) continuum states can be represented with the same accuracy. Among the codes which solve the HFB problem on a lattice in coordinate space using the quasiparticles we have: a 1-D (spherical) HFB code [81] and the present 2-D (axially symmetric) code [82, 83, 84]. In the basis expansion method a wave function is expanded into the chosen basis functions: the harmonic oscillator basis (HO) [85], the transformed harmonic oscillator basis (THO) [79]. The HFB equations have also been solved in coordinate space by means of the two-basis method [86] where one uses a truncated basis composed of bound and discretized continuum states up to a a few MeV in the continuum [87]. In an alternative approach, the HFB equations are solved on a 3-D Cartesian mesh using the canonical-basis approach [88].

We solve the Hartree-Fock-Bogoliubov (HFB) equations for deformed, axially symmetric nuclei in coordinate space on a 2-D lattice [82, 83]. Our computational technique (the Basis-Spline collocation and Galerkin method) is particularly well suited to study the ground state properties of nuclei near the driplines. It allows us totake into account high-energy continuum states up to an equivalent single-particle energyof 60 MeV or more.

### 3.1.2 2-D reduction of the HFB problem for axially symmetric systems and numerical solution .

Our goal is to reduce the Hamiltonians given by the Eq. (107) to the case of axial symmetry around the z-axis using cylindrical coordinates $(r, \phi, z)$. We require the Hamiltonian

to be invariant under rotations $\hat{R}_z$ i.e. $[\hat{\mathcal{H}}, \hat{R}_z] = 0$. Because rotations are generated by the angular momentum operator $\hat{j}_z$ via

$$\hat{R}_z(\phi) = \exp(-i\phi\hat{j}_z/\hbar), \tag{118}$$

this requirement is equivalent to

$$[\hat{\mathcal{H}}, \hat{J}_z(\phi)] = \hat{0}\ , \tag{119}$$

where

$$\hat{J}_z(\phi) = \hbar \begin{pmatrix} -i\partial_\phi + 1/2 & 0 & 0 & 0 \\ 0 & -i\partial_\phi - 1/2 & 0 & 0 \\ 0 & 0 & -i\partial_\phi + 1/2 & 0 \\ 0 & 0 & 0 & -i\partial_\phi - 1/2 \end{pmatrix}, \tag{120}$$

We find the simultaneous eigenstates of the operator $\hat{J}_z(\phi)$ and $\hat{\mathcal{H}}$ by solving the following equation

$$\hat{\tilde{J}_z}(\phi)\Psi_\Omega(r,\phi,z) = \hbar\Omega\Psi_\Omega(r,\phi,z)\ , \tag{121}$$

to arrive at [82]

$$\Psi_\Omega(r,\phi,z) = \frac{1}{\sqrt{2\pi}} \begin{pmatrix} e^{i(\Omega+1/2)\phi}\ U_1(r,z) \\ e^{i(\Omega-1/2)\phi}\ L_1(r,z) \\ e^{i(\Omega-1/2)\phi}\ U_2(r,z) \\ e^{i(\Omega+1/2)\phi}\ L_2(r,z) \end{pmatrix}, \tag{122}$$

where $\Omega = \pm\frac{1}{2}, \pm\frac{3}{2}, \pm\frac{5}{2}, \ldots$ is the eigenvalue of the the operator $\hat{J}_z(\phi)$. Using that information we simplify the eigenvalue problem (e.g Eq. (107))

$$\hat{\mathcal{H}}_\Omega(\tilde{h}, r, \phi, z)\Psi_\Omega(r,\phi,z) = E_{\alpha,\Omega}\Psi_\Omega(r,\phi,z)\ , \tag{123}$$

in the following way

$$\sum_{\sigma\sigma'} \begin{pmatrix} h^q_{\sigma\sigma'}(r,z) - \lambda^q & \tilde{h}^q_{\sigma\sigma'}(r,z) \\ \tilde{h}^q_{\sigma\sigma'}(r,z) & -h^q_{\sigma\sigma'}(r,z) + \lambda^q \end{pmatrix}_\Omega \begin{pmatrix} \phi^q_{1,\alpha}(r,z,\sigma') \\ \phi^q_{2,\alpha}(r,z,\sigma') \end{pmatrix}_\Omega = E^q_\alpha \begin{pmatrix} \phi^q_{1,\alpha}(r,z,\sigma) \\ \phi^q_{2,\alpha}(r,z,\sigma) \end{pmatrix}_\Omega \tag{124}$$

where

$$h^q_{\sigma\sigma'}(r,z) = \begin{pmatrix} h^q_{\uparrow\uparrow}(r,z) & h^q_{\uparrow\downarrow}(r,z) \\ h^q_{\downarrow\uparrow}(r,z) & h^q_{\downarrow\downarrow}(r,z) \end{pmatrix}, \tilde{h}^q_{\sigma\sigma'}(r,z) = \begin{pmatrix} \tilde{h}^q_{\uparrow\uparrow}(r,z) & \tilde{h}^q_{\uparrow\downarrow}(r,z) \\ \tilde{h}^q_{\downarrow\uparrow}(r,z) & \tilde{h}^q_{\downarrow\downarrow}(r,z) \end{pmatrix}, \tag{125}$$

and

$$\phi^q_{1,\alpha}(r,z,\sigma) = \begin{pmatrix} \phi^q_{1,\alpha}(r,z,\uparrow) \\ \phi^q_{1,\alpha}(r,z,\downarrow) \end{pmatrix}, \quad \phi^q_{2,\alpha}(r,z,\sigma) = \begin{pmatrix} \phi^q_{2,\alpha}(r,z,\uparrow) \\ \phi^q_{2,\alpha}(r,z,\downarrow) \end{pmatrix}. \tag{126}$$

The matrix elements (turn out to be real) from the Hamiltonian Eq. (124) and corresponding densities are calculated accordingly using cylindrical coordinates. A detailed description of our theoretical method has been published in refs. [82, 76, 89]; in the following, we give a brief summary. Using cylindrical coordinates $(r, z, \phi)$, we introduce a 2-D grid $(r_\alpha, z_\beta)$ with $\alpha = 1, ..., N_r$ and $\beta = 1, ..., N_z$ (Fig. 14). In radial direction, the grid spans the region

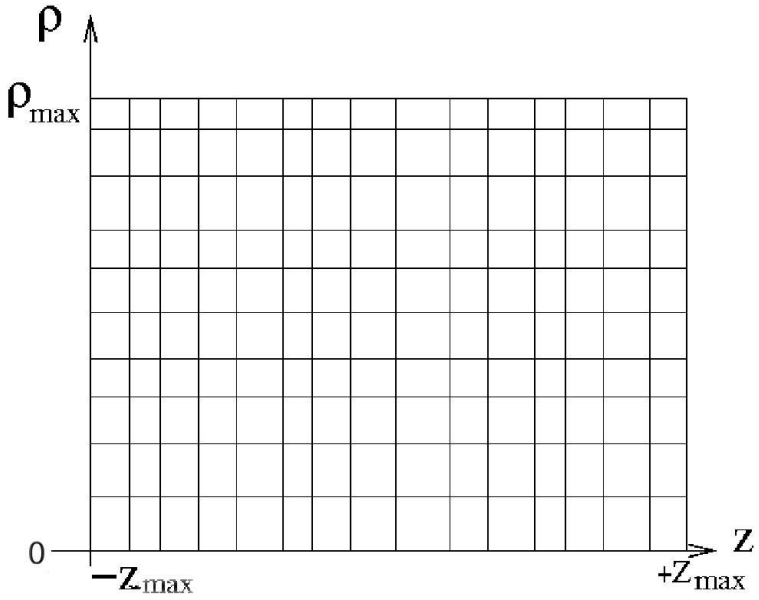


Figure 14: 2-D grid in cylindrical coordinates.

from 0 to $r_{max}$. Because we want to be able to treat octupole shapes, we do not assume left-right symmetry in $z$-direction. Consequently, the grid extends from $-z_{max}$ to $+z_{max}$. Typically, $z_{max} \approx r_{max}$ and $N_z \approx 2 \cdot N_r$. For the lattice representation, the wavefunctions

and operators are represented in terms of Basis-Splines [90, 91, 50, 92, 93, 94]. B-Splines of order $M$, $B_i^M(x)$, are a set $(i = 1, ..., \mathcal{N})$ of piecewise continuous polynomial sections of order $M - 1$; a special case are the well-known finite elements which are B-Splines of order $M = 2$. By using B-Splines of seventh or ninth oder, we are able to represent derivative operators very accurately on a relatively coarse grid with a lattice spacing of about 0.8 fm resulting in a lattice Hamiltonian matrix of relatively low dimension. The four components $(n = 1, ..., 4)$ of the HFB bi-spinor wavefunction $\psi_n(r, z)$ are expanded in terms of a product of B-Splines

$$\psi_n(r_\alpha, z_\beta) = \sum_{i=1}^{\mathcal{N}_i} \sum_{j=1}^{\mathcal{N}_j} B_i^M(r_\alpha) B_j^M(z_\beta) U_n^{ij} \ . \tag{127}$$

For the lattice representation of the Hamiltonian, we use a hybrid method in which derivative operators are constructed using the Galerkin method [89, 93, 95]; this amounts to a global error reduction. Local potentials are represented by the collocation method [94, 93] (local error reduction). The numerical solution of the HFB equations results in a set of quasiparticle wavefunctions and energies. The quasiparticle energy spectrum contains both bound and (discretized) continuum states. We diagonalize the HFB Hamiltonian separately for fixed isospin projection $q$ and angular momentum projection $\Omega$. Note that the number of quasiparticle eigenstates is determined by the dimensionality of the lattice HFB Hamiltonian. For fixed values of $q$ and $\Omega$, we obtain $4 \cdot N_r \cdot N_z$ eigenstates, typically up to 1,000 MeV. Production runs of our HFB-2D-LATTICE code are carried out on an IBM-SP massively parallel supercomputer and on the local cluster computer at the ACCRE, Vanderbilt University. We utilize MPI message passing interface. Parallelization is possible for different angular momentum states $\Omega$ and isospins (p/n) . Details are described in Section 4.1.

### 3.1.3 Calculated HFB observables

Despite the fact that the quasiparticles we have introduced do not have a direct physical meaning, we can extract physical information from them. We express the densities in terms of quasiparticle wave-functions, which on the other hand carry physical information about the nucleus. Of the long list of the quantities that can be calculated the most important are:

- total binding energy $E_{bind}(Z, N)$

In addition to the energy components in the HF theory, Eq. (22), i.e. kinetic energy term, the Skyrme functional term, the Skyrme spin-orbit term, Coulomb term, and center of mass correction term, the HFB energy functional is supplemented with a pairing energy term arising from the presence of the paring Hamiltonian Eq. (113)

$$E_0^{HF} = E_{kin} + E_{Sky} + E_{Sky,LS} + E_{Coul} + E_{CM} + E_{pair} \tag{128}$$

- two-neutron separation energy

$$S_{2n}(Z,N) = E_{bind}(Z,N) - E_{bind}(Z,N-2). \tag{129}$$

The two-neutron separation energy is defined as as the binding energy difference of the two neighborhood nuclei. Note that in using this equation, all binding energies must be entered with a positive sign. The position of the two-neutron dripline is defined by the condition $S_{2n}(Z,N) = 0$, and nuclei with negative two-neutron separation energy are unstable against the emission of two neutrons.

- mass quadrupole moment

$$Q_{zz} = \int d^3r(3z^2 - \mathbf{r}^2)\rho(\mathbf{r}), \tag{130}$$

carries information about the deformation of the nucleus. Particularly, depending on the sign of this quantity we can have for

$$Q_{zz} = \begin{cases} 0, \text{ spherical deformation} \\ \textit{negative}, \text{ oblate deformation} \\ \textit{positive}, \text{ prolate deformation.} \end{cases} \tag{131}$$

Depending on the the kind of the density in the Eq. (130) we can calculate; the total mass quadrupole moment $Q_{zz}(total)$ for $\rho = \rho_n + \rho_p$, the mass quadrupole moment for protons or neutrons $Q_{zz}(n/p)$ for $\rho = \rho_{n/p}$.

- mean-square radius

$$\langle r^2 \rangle = \frac{1}{N} \int d^3r \rho(\mathbf{r})\mathbf{r^2}, \tag{132}$$

for neutrons or protons $\langle r^2 \rangle_{n/p}, (\rho = \rho_{n/p}), N$ is the number of neutrons or protons, or the total rms $\langle r^2 \rangle_{total}, (\rho = \rho_n + \rho_p)$, N is the total number of the particles.

- average pairing gaps (Eq. 113) defined as [80, 82, 46]

$$\langle \Delta_q \rangle = -\frac{1}{N_q} Tr(\tilde{h}^q \rho_q), \tag{133}$$

  for protons or neutrons.

- Fermi level (Fig. 13) $\lambda_q$ for protons and neutrons

The above quantities are calculated using the cylindrical coordinates in Ref. [82] in case of the axial symmetry.

### 3.1.4 Decoupled HFB equations.

In Ref.[96] the authors managed to decouple the HFB equations and solve the smaller problem (diagonalization) rather than diagonalizing the full HFB Hamiltonian. The problem that was solved in Ref.[96] in the notation of Eq.(96) is the following

$$\begin{pmatrix} \hat{h}' & -\hat{\Delta} \\ \hat{\Delta} & -\hat{h}' \end{pmatrix} \begin{pmatrix} \hat{\psi}^{\pm}_{\alpha,1} \\ \hat{\psi}^{\pm}_{\alpha,2} \end{pmatrix} = E^{\pm}_{\alpha} \begin{pmatrix} \hat{\psi}^{\pm}_{\alpha,1} \\ \hat{\psi}^{\pm}_{\alpha,2} \end{pmatrix} , \tag{134}$$

where $\hat{h}' \equiv \hat{h} - \lambda$ ($\lambda$ is the Fermi level ). The quasiparticle states denoted as $\hat{\psi}^{+}_{\alpha,1}, \hat{\psi}^{+}_{\alpha,2}$ are positive eigenstates and $\hat{\psi}^{-}_{\alpha,1}, \hat{\psi}^{-}_{\alpha,2}$ are negative eigenstates corresponding to $E^{\pm}_{\alpha} \equiv \pm|E_{\alpha}|$ respectively. We keep the Eq.(134) in the operator form as going to the specific representation is straightforward (e.g. Eq. 96). The method that was applied in Ref.[96] can be equivalently formulated as the unitary transformation $R$

$$R = R^T = R^{-1} = \frac{1}{\sqrt{2}} \begin{pmatrix} 1 & 1 \\ 1 & -1 \end{pmatrix} , \tag{135}$$

of the Hamiltonian Eq. (134)

$$R \begin{pmatrix} \hat{h}' & -\hat{\Delta} \\ \hat{\Delta} & -\hat{h}' \end{pmatrix} R^{-1} R \begin{pmatrix} \hat{\psi}^{\pm}_{\alpha,1} \\ \hat{\psi}^{\pm}_{\alpha,2} \end{pmatrix} = E^{\pm}_{\alpha} R \begin{pmatrix} \hat{\psi}^{\pm}_{\alpha,1} \\ \hat{\psi}^{\pm}_{\alpha,2} \end{pmatrix} . \tag{136}$$

After the transformation Eq. (136) will have the following block off-diagonal form

$$\begin{pmatrix} 0 & \hat{h}' + \hat{\Delta} \\ \hat{h}' - \hat{\Delta} & 0 \end{pmatrix} \begin{pmatrix} \hat{\chi}^{\pm}_{\alpha,1} \\ \hat{\chi}^{\pm}_{\alpha,2} \end{pmatrix} = E^{\pm}_{\alpha} \begin{pmatrix} \hat{\chi}^{\pm}_{\alpha,1} \\ \hat{\chi}^{\pm}_{\alpha,2} \end{pmatrix} , \tag{137}$$

where

$$\begin{pmatrix} \hat{\chi}^{\pm}_{\alpha,1} \\ \hat{\chi}^{\pm}_{\alpha,2} \end{pmatrix} \equiv R \begin{pmatrix} \hat{\psi}^{\pm}_{\alpha,1} \\ \hat{\psi}^{\pm}_{\alpha,2} \end{pmatrix} . \tag{138}$$

The new transformed eigenstates are called by the authors of Ref.[96] the auxiliary functions. The next step in this derivation is to apply the transformed Hamiltonian Eq. (137) onto the left of Eq. (137) to obtain,

$$\begin{pmatrix} (\hat{h}' + \hat{\Delta})(\hat{h}' - \hat{\Delta}) & 0 \\ 0 & (\hat{h}' - \hat{\Delta})(\hat{h}' + \hat{\Delta}) \end{pmatrix} \begin{pmatrix} \hat{\chi}^{'}_{\alpha,1} \\ \hat{\chi}^{'}_{\alpha,2} \end{pmatrix} = E^2_{\alpha} \begin{pmatrix} \hat{\chi}^{'}_{\alpha,1} \\ \hat{\chi}^{'}_{\alpha,2} \end{pmatrix} . \tag{139}$$

The new eigenstates $\hat{\chi}^{'}_{\alpha,1}$ and $\hat{\chi}^{'}_{\alpha,2}$ can be in general linear combinations of the negative and positive states $\hat{\chi}^{\pm}_{\alpha,1}$ and $\hat{\chi}^{\pm}_{\alpha,2}$, since we lost information about the sign of the energy $\mathrm{E}_{\alpha}$. We can write

$$\begin{pmatrix} \hat{\chi}'_{\alpha,1} \\ \hat{\chi}'_{\alpha,2} \end{pmatrix} = w^{+} \begin{pmatrix} \hat{\chi}^{+}_{\alpha,1} \\ \hat{\chi}^{+}_{\alpha,2} \end{pmatrix} + w^{-} \begin{pmatrix} \hat{\chi}^{-}_{\alpha,1} \\ \hat{\chi}^{-}_{\alpha,2} \end{pmatrix} , \tag{140}$$

where $w^{+}$ and $w^{-}$ are complex constants. Throughout this work we use the Hamiltonian expressed via the hermitian pairing field $\tilde{h}$, Eq. (116)

$$\begin{pmatrix} \hat{h}' & \hat{\tilde{h}} \\ \hat{\tilde{h}} & -\hat{h}' \end{pmatrix} \begin{pmatrix} \hat{\psi}^{\pm}_{\alpha,1} \\ \hat{\psi}^{\pm}_{\alpha,2} \end{pmatrix} = E^{\pm}_{\alpha} \begin{pmatrix} \hat{\psi}^{\pm}_{\alpha,1} \\ \hat{\psi}^{\pm}_{\alpha,2} \end{pmatrix} . \tag{141}$$

With such a form of the Hamiltonian it is not possible to apply directly the unitary transformation (Eq. 135) in order to obtain the block off-diagonal form of the Hamiltonian (Eq. 137). We have to transform first unitarily the Hamiltonian Eq. (141) to obtain opposite signs for the pairing field $\hat{\tilde{h}}$ on the off-diagonal. In order to do so the unitary transformation $Z$ needs to be complex [97]

$$Z = \frac{1}{\sqrt{2}} \begin{pmatrix} 1 & 1 \\ -i & i \end{pmatrix} , \tag{142}$$

$$Z^{-1} = \frac{1}{\sqrt{2}} \begin{pmatrix} 1 & i \\ 1 & -i \end{pmatrix} . \tag{143}$$

After transformation we arrive at the form of the Hamiltonian suitable for applying the real transformation $R$ (Eq. 135).

$$Z\begin{pmatrix} \hat{h}' & \hat{\tilde{h}} \\ \hat{\tilde{h}} & -\hat{h}' \end{pmatrix} Z^{-1} Z \begin{pmatrix} \hat{\psi}^{\pm}_{\alpha,1} \\ \hat{\psi}^{\pm}_{\alpha,2} \end{pmatrix} = E^{\pm}_{\alpha} Z \begin{pmatrix} \hat{\psi}^{\pm}_{\alpha,1} \\ \hat{\psi}^{\pm}_{\alpha,2} \end{pmatrix} \Rightarrow \tag{144}$$

$$\Rightarrow \begin{pmatrix} \hat{\tilde{h}} & i\hat{h}' \\ -i\hat{h}' & -\hat{\tilde{h}} \end{pmatrix} Z \begin{pmatrix} \hat{\psi}^{\pm}_{\alpha,1} \\ \hat{\psi}^{\pm}_{\alpha,2} \end{pmatrix} = E^{\pm}_{\alpha} Z \begin{pmatrix} \hat{\psi}^{\pm}_{\alpha,1} \\ \hat{\psi}^{\pm}_{\alpha,2} \end{pmatrix}.$$

Note the opposite signs next to the pairing field on the diagonal, and next to the complex mean field on the off-diagonal. The transformation $R$ and $Z$ can be combined into the one unitary transformation $U$

$$U = RZ = \frac{1}{2}\begin{pmatrix} 1-i & 1+i \\ 1+i & i-i \end{pmatrix}, \tag{145}$$

$$U^{-1} = \frac{1}{2}\begin{pmatrix} 1+i & 1-i \\ 1-i & 1+i \end{pmatrix}. \tag{146}$$

We can repeat now the steps (Eqs. 135-140) that were taken to arrive at the Eq. (139) and apply the transformation (Eq. 145) to the Eq. (141)

$$U\begin{pmatrix} \hat{h}' & \hat{\tilde{h}} \\ \hat{\tilde{h}} & -\hat{h}' \end{pmatrix} U^{-1} U \begin{pmatrix} \hat{\psi}^{\pm}_{\alpha,1} \\ \hat{\psi}^{\pm}_{\alpha,2} \end{pmatrix} = E^{\pm}_{\alpha} U \begin{pmatrix} \hat{\psi}^{\pm}_{\alpha,1} \\ \hat{\psi}^{\pm}_{\alpha,2} \end{pmatrix} \Rightarrow$$

$$\Rightarrow \quad \begin{pmatrix} 0 & (-i\hat{h} + \hat{\tilde{h}}) \\ (i\hat{h} + \hat{\tilde{h}}) & 0 \end{pmatrix} \begin{pmatrix} \hat{\chi}^{\pm}_{\alpha,1} \\ \hat{\chi}^{\pm}_{\alpha,2} \end{pmatrix} = E^{\pm}_{\alpha} \begin{pmatrix} \hat{\chi}^{\pm}_{\alpha,1} \\ \hat{\chi}^{\pm}_{\alpha,2} \end{pmatrix}, \tag{147}$$

where

$$\begin{pmatrix} \hat{\chi}^{\pm}_{\alpha,1} \\ \hat{\chi}^{\pm}_{\alpha,2} \end{pmatrix} = U \begin{pmatrix} \hat{\psi}^{\pm}_{\alpha,1} \\ \hat{\psi}^{\pm}_{\alpha,2} \end{pmatrix}. \tag{148}$$

As expected we obtain the block diagonal form of the transformed Hamiltonian (Eq. 147)

$$\begin{pmatrix} (-i\hat{h} + \hat{\tilde{h}})(i\hat{h} + \hat{\tilde{h}}) & 0 \\ 0 & (i\hat{h} + \hat{\tilde{h}})(-i\hat{h} + \hat{\tilde{h}}) \end{pmatrix} \begin{pmatrix} \hat{\chi}'_{\alpha,1} \\ \hat{\chi}'_{\alpha,2} \end{pmatrix} = E^2_{\alpha} \begin{pmatrix} \hat{\chi}'_{\alpha,1} \\ \hat{\chi}'_{\alpha,2} \end{pmatrix}, \tag{149}$$

where again we have (Eq. 140)

$$\begin{pmatrix} \hat{\chi}'_{\alpha,1} \\ \hat{\chi}'_{\alpha,2} \end{pmatrix} = w^{+} \begin{pmatrix} \hat{\chi}^{+}_{\alpha,1} \\ \hat{\chi}^{+}_{\alpha,2} \end{pmatrix} + w^{-} \begin{pmatrix} \hat{\chi}^{-}_{\alpha,1} \\ \hat{\chi}^{-}_{\alpha,2} \end{pmatrix}. \tag{150}$$

Table 3: Relative speed up factor in CPU time for diagonalization of the HFB matrix: decoupled vs. coupled version.

| isotope | coupled HFB matrix size | decoupled HFB matrix size | speed up |
|---|---|---|---|
| $^{22}$Ne | 2160 | 1080 | 4.07 |
| $^{112}$Zr | 4680 | 2340 | 3.78 |
| $^{238}$U | 6944 | 3472 | 3.86 |

Since in Eq. (149) the states $\hat{\chi}'_{\alpha,1}$ and $\hat{\chi}'_{\alpha,2}$ are decoupled the problem can be diagonalized by using the smaller matrices along the diagonal. As we will show, solving for only one of the components is sufficient. Acting with the transformed Hamiltonian (Eq. 147) on both sides of the Eq. (150) results in two states, one of which is

$$\hat{\chi}''_{\alpha,2} \equiv \tfrac{1}{|E^{\pm}_{\alpha}|}(i\hat{h} + \hat{\bar{h}})\chi'_{\alpha,1} = w^{+}\hat{\chi}^{+}_{\alpha,2} - w^{-}\hat{\chi}^{-}_{\alpha,2} \quad , \tag{151}$$

where we have explicitly used the minus sign for the negative energy component. Now we construct new states

$$\begin{aligned} \hat{X}_{+} &\equiv \hat{\chi}'_{\alpha,1} + \hat{\chi}''_{\alpha,2} \ , \\ \hat{X}_{-} &\equiv \hat{\chi}'_{\alpha,1} - \hat{\chi}''_{\alpha,2} \ . \end{aligned} \tag{152}$$

To evaluate the new states we express all quantities in terms of original states $\hat{\psi}^{\pm}_{\alpha,1}, \hat{\psi}^{\pm}_{\alpha,2}$ using Eq. (148)

$$\begin{aligned} \hat{\chi}^{\pm}_{\alpha,1} &= \frac{1}{2}\left[(1-i)\hat{\psi}^{\pm}_{\alpha,1} + (1+i)\hat{\psi}^{\pm}_{\alpha,2}\right] \ , \\ \hat{\chi}^{\pm}_{\alpha,2} &= \frac{1}{2}\left[(1+i)\hat{\psi}^{\pm}_{\alpha,1} + (1-i)\hat{\psi}^{\pm}_{\alpha,2}\right] \ . \end{aligned} \tag{153}$$

After inserting it into the Eq. (152) we obtain

$$\hat{X}_{+} = w_{+}(\hat{\psi}^{+}_{\alpha,2} + \hat{\psi}^{+}_{\alpha,1}) + iw^{-}(\hat{\psi}^{-}_{\alpha,2} - \hat{\psi}^{-}_{\alpha,1}), \tag{154}$$

$$\hat{X}_{-} = iw^{+}(\hat{\psi}^{+}_{\alpha,2} - \hat{\psi}^{+}_{\alpha,1}) + w^{-}(\hat{\psi}^{-}_{\alpha,1} + \hat{\psi}^{-}_{\alpha,2}) \ . \tag{155}$$

The states $\hat{X}^{+}$ and $\hat{X}^{-}$ contain the mixture of original negative and positive eigenstates $\hat{\psi}^{\pm}_{\alpha}$. We use the relation between positive and negative [80],

$$\begin{pmatrix} \hat{\psi}^{E}_{\alpha,1} \\ \hat{\psi}^{E}_{\alpha,2} \end{pmatrix} = \begin{pmatrix} \hat{\psi}^{-E}_{\alpha,2} \\ -\hat{\psi}^{-E}_{\alpha,1} \end{pmatrix} \ . \tag{156}$$

to express the states $\hat{X}^+$ and $\hat{X}^-$ only in terms of positive states $\hat{\psi}^+_\alpha$ or negative ones $\hat{\psi}^-_\alpha$

$$\begin{aligned}\hat{X}_+ &= w^+(\hat{\psi}^+_{\alpha,2} + \hat{\psi}^+_{\alpha,1}) + iw^-(\hat{\psi}^+_{\alpha,1} + \hat{\psi}^+_{\alpha,2}),\\ \hat{X}_- &= iw^+(\hat{\psi}^+_{\alpha,2} - \hat{\psi}^+_{\alpha,1}) + w^-(\hat{\psi}^+_{\alpha,1} - \hat{\psi}^+_{\alpha,2}) \ ,\end{aligned} \tag{157}$$

or

$$\begin{aligned}\hat{X}_+ &= w^+(\hat{\psi}^-_{\alpha,2} - \hat{\psi}^-_{\alpha,1}) + iw^-(\hat{\psi}^-_{\alpha,2} - \hat{\psi}^-_{\alpha,1}),\\ \hat{X}_- &= -iw^+(\hat{\psi}^-_{\alpha,2} + \hat{\psi}^-_{\alpha,1}) + w^-(\hat{\psi}^-_{\alpha,1} + \hat{\psi}^-_{\alpha,2}) \ .\end{aligned} \tag{158}$$

From the Eqs. (157-158) we easily extract our original positive states equal to

$$\begin{aligned}(iw^+ - w^-)\hat{\psi}^+_{\alpha,1} &= \tfrac{1}{2}(i\hat{X}_+ - \hat{X}_-) \ ,\\ (iw^+ - w^-)\hat{\psi}^+_{\alpha,2} &= \tfrac{1}{2}(i\hat{X}_+ + \hat{X}_-) \ ,\end{aligned} \tag{159}$$

or negative ones

$$\begin{aligned}(w^- - iw^+)\hat{\psi}^-_{\alpha,1} &= \tfrac{1}{2}(i\hat{X}_+ + \hat{X}_-) \ ,\\ (w^- - iw^+)\hat{\psi}^-_{\alpha,2} &= \tfrac{1}{2}(-i\hat{X}_+ + \hat{X}_-) \ ,\end{aligned} \tag{160}$$

which are multiplied by a complex constant handled by normalization. We summarize here the steps, which lead to the more effective diagonalization:

- Using the unitary transformation U in Eq. (145), construct and diagonalize only the upper (lower ) block of the Hamiltonian, Eq. (149)
- take the obtained eigenstate $\chi'_{\alpha,1}$ ($\chi'_{\alpha,2}$) and generate the state $\chi''_{\alpha,2}$ ($\chi''_{\alpha,1}$), Eq. (151)
- generate the states $X^+$ and $X^-$, (Eq. 152)
- calculate the RHS of Eq. (159) or Eq. (160)
- take the real or imaginary part of the RHS of Eq. (159) or Eq. (160) and normalize it.

The time saved in obtaining the eigenstates (original eigenstates) of the Hamiltonian in Eq. (141) by diagonalizing only the upper block of the Hamiltinian in Eq. (149) is shown in Table. (3). Studies show a gain in computation time by a factor of four. The tests were performed for the three isotopes $^{22}$Ne,$^{112}$Zr and $^{238}$U with the appropriate Hamiltonian matrices size. The method of obtaining the original eigenstates by diagonalizing the complex upper block of the matrix in Eq. (149) includes an extra step, which is extracting the original

eigenstates from the complex eigenstates of the Hamiltonian in Eq. (149). This step is also included in the timing procedure, therefore we can draw the conclusion, that finding the HFB ground state using our HFB-2D-LATTICE code can be speeded up according to Table. (3) almost four times. The time spent on other operations inside the program e.g. constructing densities and mean-field Hamiltonian, which has not been included in the timing studies is negligible compared to the diagonalization time.

# CHAPTER IV

# NUMERICAL IMPLEMENTATIONS

## 4.1 Implementation of HFB-2D-LATTICE code on parallel computers

The numerical solution of the HFB-2D-LATTICE code requires the use of the parallel computers due to the very time consuming calculations. Currently, we use as the method of solution the iterative diagonalization technique, where we obtain the wave-functions and the corresponding eigenvectors from the direct diagonalization. The size of the constructed HFB Hamiltonian on the spatial lattice depends on the size of the 2D-grid (sec:3.1.2) . This leads to the size of matrices of the order of $4000 \times 4000$ for the relatively large systems (e.g. calculations for the Zr isotope chain, see section (5.1)). The Hamiltonian matrix in 2D is real and non-symmetric. The lack of the symmetric property is caused by the application of the Galerkin/collocation method to represent the differential operators on the spatial lattice [90, 91, 50, 92, 93, 94]. Therefore, we are forced to use the direct eigensolvers (Linear Algebra Package(LAPACK95)) for general matrices. Additionally, the diagonalization needs to be performed separately for all magnetic substates, per iteration (i.e. 22 times for the our typical choice of the $\Omega$=21/2) . Typically, our HFB code requires on average about 50 iterations for all of the observables to converge. It is obvious that the bottle-neck of the performance of the our HFB code is caused by the direct diagonalization method. Unfortunately, as of today this is the only known reliable technique that one has to use to solve the 2D HFB problem in coordinate space using the Basis -Spline method [90, 91, 50, 92, 93, 94]. For all of the mentioned reasons, to speed up our calculations, we chose to implement our HFB code on parallel computers.

### 4.1.1 MPI implementation of the HFB-2D-LATTICE code.

Currently, our 2D Basis-Spline code in coordinate space utilizes the iterative diagonalization technique to obtain ground states properties. The iterations are performed until the convergence is achieved. Below we describe the process for the iterative solution.

I. Construct the quasiparticle Hamiltonian (Eq. 124) $\hat{\mathcal{H}}_\Omega(\rho, \rho_{n,p}, \tilde{\rho}, \tilde{\rho}_{n,p}, \tau, \tau_{n,p}, \lambda_{n/p})$,

which depends on various densities and the Fermi levels $\lambda_{n/p}$ for each angular momentum number $\Omega$ . Perform diagonalization separately for neutrons and protons for each $\Omega$ and obtain the quasiparticle energies $E_{\Omega,n}$ and wave-functions $\Phi_{\Omega,n}$.

II. Calculate the following quantities:

- add up the partial densities $\{\rho_\Omega, \rho^\Omega_{n,p}, \tilde{\rho}_\Omega, \tilde{\rho}^\Omega_{n,p}, \tau_\Omega, \tau^\Omega_{n,p}\}$ and calculate the total densities $\rho, \rho_{n,p}, \tilde{\rho}, \tilde{\rho}_{n,p}, \tau, \tau_{n,p}$
- average pairing gaps $\Delta_{n,p}(\tilde{h}, \rho)$
- Fermi levels $\lambda_{n,p}(\Delta_{n,p}, E_n)$

III. Check convergence comparing several observables (i.e. binding energy,pairing gaps) from the previous two iterations. If convergence is achieved, then print output files. If not, then go to (1).

On a multi-processors computer it is possible to parallelize the above scheme for different angular momentum numbers $\Omega$ and different isospin ( protons/neutrons). To simplify, the diagonalization for every angular momentum number from $\Omega_{min} = \frac{1}{2}$ to $\Omega_{max}$ is carried separately for neutrons and protons by the processors labeled by $(\Omega - \frac{1}{2})$. In general, one needs PN=$(2\Omega_{max} + 1)$ processors; for example, if $\Omega_{max} = \frac{21}{2}$, one needs 22 processors (neutrons+protons). In the MPI (Message Passage Interface) [98] nomenclature we talk about processes, which have its own IDs. For simplicity, we can think about the processors as they were the processes. The parallelization scheme we have chosen to write the (Fortran90+MPI) parallel implementation of the Vanderbilt HFB code designates one process (*Root process*(#0)) , which calculates the total densities, Fermi level and pairing gaps. Consequently, *every process* labeled by $\Omega$ (including *Root process* ) performs a diagonalization and calculates partial densities (for each angular momentum number $\Omega$). The communication between the (*Root process*(#0) and the *every process*, which is necessary to perform more than one iteration is provided by the MPI commands. We used "MPI Fortran Bindings" [98], which means that MPI commands can be mixed with the Fortran language. Below as well as in Fig. (15) we describe the parallelized process of the iterative solution

I. *Every process ($\Omega$)*:

- if the iteration number is greater than one, every process receives the total densities, the average pairing gaps $\Delta_{n,p}(\tilde{h},\rho)$ and the Fermi levels $\lambda_{n,p}$ from the *Root process* by calling the subroutine $rec\_from\_root()$. If iteration number is equal equal to one, every process reads the mentioned quantities from the input files
- constructs and diagonalizes the Hamiltonian $\hat{\mathcal{H}}_\Omega(\rho,\rho_{n,p},\tilde{\rho},\tilde{\rho}_{n,p},\tau,\tau_{n,p},\lambda_{n/p})$ dependent on various total densities and the Fermi level $\lambda_{n/p}$
- calculates the new partial densities $\{\rho_\Omega,\rho^\Omega_{n,p},\tilde{\rho}_\Omega,\tilde{\rho}^\Omega_{n,p},\tau_\Omega,\tau^\Omega_{n,p}\}$ from the eigenfunctions $\Phi_{\Omega,n}$
- sends the quasiparticle energies $E_{n,\Omega}$ and the new partial densities $\{\rho_\Omega,\rho^\Omega_{n,p},\tilde{\rho}_\Omega,\tilde{\rho}^\Omega_{n,p},\tau_\Omega,\tau^\Omega_{n,p}\}$ to the *Root process* by calling the subroutine $send\_to\_root()$

II. *Root process (#0):*

- receives the quasiparticle energies $E_{n,\Omega}$ and the partial densities $\{\rho_\Omega,\rho^\Omega_{n,p},\tilde{\rho}_\Omega,\tilde{\rho}^\Omega_{n,p},\tau_\Omega,\tau^\Omega_{n,p}\}$ from every process by calling the subroutine $rec\_from\_everybody()$
- calculates the total densities $\rho,\rho_{n,p},\tilde{\rho},\tilde{\rho}_{n,p},\tau,\tau_{n,p}$ from the received partial densities $\{\rho_\Omega,\rho^\Omega_{n,p},\tilde{\rho}_\Omega,\tilde{\rho}^\Omega_{n,p},\tau_\Omega,\tau^\Omega_{n,p}\}$
- calculates average pairing gaps $\Delta_{n,p}(\tilde{h},\rho)$ for protons and neutrons
- calculates the Fermi levels $\lambda_{n,p}(\Delta_{n,p},E_{n,\Omega})$ for protons and neutrons
- checks the convergence comparing chosen observables (i.e. binding energy, pairing gaps) from the previous two iterations.
  - if convergence is achieved, then print output files and stop
  - if not, send the total densities $\{\rho,\rho_{n,p},\tilde{\rho},\tilde{\rho}_{n,p},\tau,\tau_{n,p}\}$, the Fermi levels $\lambda_{n,p}(\Delta_{n,p},E_{n,\Omega})$ and average pairing gaps $\Delta_{n,p}(\tilde{h},\rho)$ to the *Root process* for the next iteration by calling the subroutine $send\_to\_everybody()$. Go to (1).

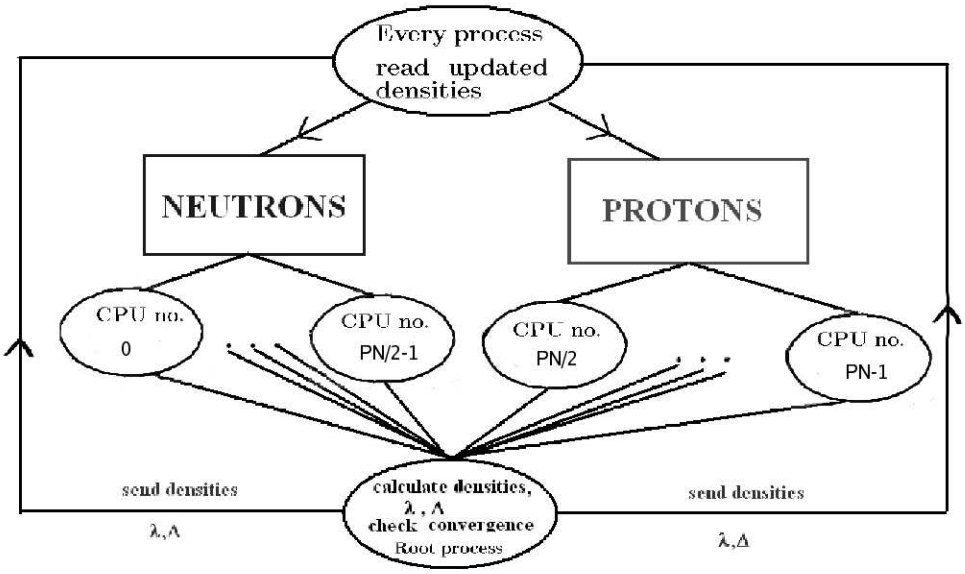


Figure 15: Scheme of the parallelization of the HFB-2D-LATTICE code ; PN is the total number of the available processors. The processes are enumerated from 0 . . . PN-1.

As was mentioned, there is a need of communication between the designated "*Root process*" and the "*Every process*". In the parallel version of our HFB code is controlled by the four subroutines, namely (Fig. 16)

- $rec\_from\_root()$
- $send\_to\_root()$
- $rec\_from\_everybody()$
- $send\_to\_everybody()$.

Each subroutine uses the nonblocking (Ref. [98]) MPI_ISEND(. . .) subroutine to send the data and the corresponding MPI_IRECV(. . .) to receive. Additionally, the sending and receiving process needs to synchronized, e.g. the "'Root process" sends a message first to the chosen process that is ready to receive the data (calls $rec\_from\_everybody$). After the selected process receives the message from the ''Root process" it starts to send

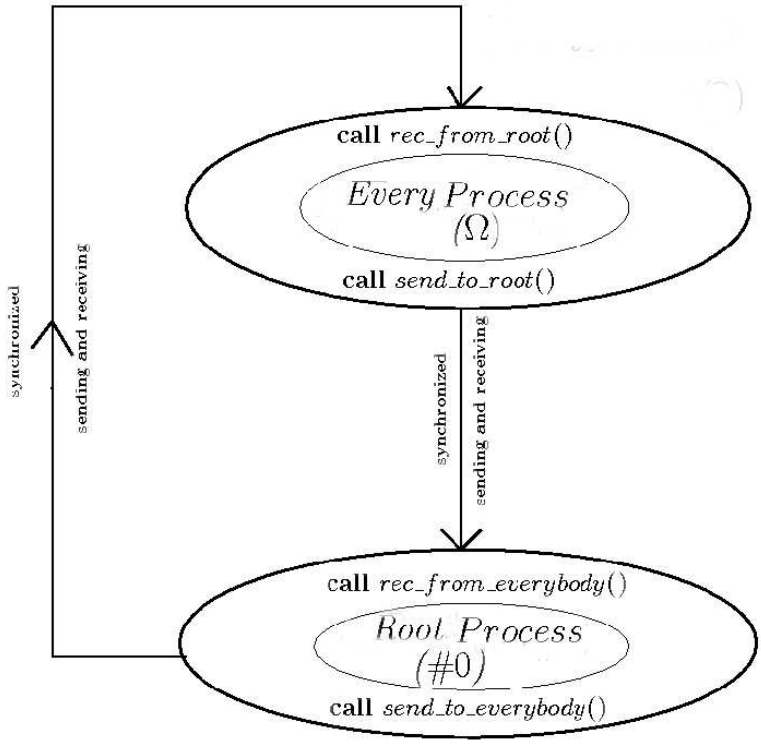


Figure 16: Synchronized sending and receiving the data between the "'Root process" and the "Every process".

(calls *send_to_root*) the data to the 'Root process" . Similarly, the ''Root process" (calls *send_to_everybody*) sends the successive portions of the data to the "'Every process" only when the addressee received (calls r*ec_from_root*) the information packet. The benefit of the effort spent on parallelizing our HFB-2D-LATTICE code was worthwhile. For the typical choice of the maximum angular momentum number $\Omega_{max} = 21/2$ our code runs approximately 22 times faster due to the use of 22 processors at the same time. This limits the time spent on the calculations for one isotope from several weeks to approximately three days [82, 95].

We perform our calculations on the NERSC IBM SP RS/6000 supercomputer and on the cluster computer "Vampire" at the ACCRE, Vanderbilt University. The former, named "SEABORG" in honor of Glenn Seaborg, is a distributed memory computer with 6,080 processors. The processors are distributed among 380 compute nodes with 16 processors per

node. Each node has available memory between 16 and 64 GBytes. The latter, "Vampire", currently consists of 360 Linux compute nodes with two 2.0 GHz Xeon or Opteron processors per node. The available memory per node ranges from 512 KB to 2 GB.

# CHAPTER V

# RESULTS

We solve the Hartree-Fock-Bogoliubov (HFB) equations for deformed, axially symmetric even-even nuclei in coordinate space on a 2-D lattice utilizing the Basis-Spline expansion method. Results are presented for the neutron-rich Zirconium and Krypton isotopes up to the two-neutron dripline. These isotopes are from the mass region of $A \sim 100$, which has been of interest for a long time to nuclear structure physicists as an area of competition between various coexisting nuclear shapes (well-deformed prolate, oblate, or spherical) [99]. In particular, we calculate binding energies, two-neutron separation energies, normal densities and pairing densities, mean square radii, quadrupole moments, and pairing gaps.

## 5.1 Calculations for Zr isotope chain .

In this section we study the ground state properties of neutron-rich Zirconium nuclei ($Z = 40$) up to the two-neutron dripline [95, 100]. The isotope chain calculations start from the $^{102}$Zr isotope up to the dripline nucleus, which turns out to be $^{122}$Zr. The Zirconium isotopes are known to possess a rapidly changing nuclear shape when the neutron number changes from 56 to 60 [101]. We find that a spherical ground state shape is preferred over a prolate shape starting from the $^{114}$Zr isotope up to the dripline nucleus $^{122}$Zr. Very large prolate quadrupole deformations ($\beta_2 = 0.42, 0.43, 0.47$) are found for the $^{102,104,112}$Zr isotopes, in agreement with recent experimental data. Two theoretical approaches are presented and compared: a) a 2-D lattice method using Basis-Spline technology (hereafter referred to as HFB-2D-LATTICE), and b) an expansion in a 2-D harmonic oscillator (HFB-2D-HO) and transformed harmonic oscillator basis (HFB-2D-THO) [79].

### $^{120}$Sn isotope - fitting the pairing strength.

In all calculations we utilize the SLy4 Skyrme force [102, 103] and a zero-range pairing force with a strength parameter $V_0 = -187.1305$ (HFB-2D-LATTICE code), and $V_0 = -187.1000$ (HFB-2D-THO code) with an equivalent single particle energy [104, 82] cutoff

parameter of $\varepsilon_{max} = 60$ MeV.

The pairing strength $V_0$ has been adjusted in both codes to reproduce the measured average neutron paring gap of 1.245 MeV in $^{120}$Sn [81], as can be seen from Table 4.

Table 4: Results for $^{120}_{50}Sn$. Comparison of results obtained from the HFB-2D-LATTICE code (first row) with HFB-2D-THO results (second row) and the experiment (third row). The columns display binding energies (BE), intrinsic quadrupole moments for neutrons and protons ($Q_n$,$Q_p$), rms-radii ($r_n$,$r_p$), average pairing gaps ($\Delta_n, \Delta_p$), pairing energy for neutrons ($PE_n$), and Fermi levels ($\lambda_n, \lambda_p$).

| BE(MeV) | $Q_n$(fm$^2$) | $Q_p$(fm$^2$) | $r_n$(fm) | $r_p$(fm) |
|---|---|---|---|---|
| -1019.26 | 0.29 | 0.12 | 4.725 | 4.590 |
| -1018.22 | 0.00 | 0.00 | 4.728 | 4.593 |
| -1020.54 | - | - | - | - |
| $\Delta_n$(MeV) | $\Delta_p$(MeV) | $PE_n$(MeV) | $\lambda_n$(MeV) | $\lambda_p$(MeV) |
| 1.244999 | 0.0 | -10.24 | -7.98 | -8.16 |
| 1.245469 | 0.0 | -10.26 | -7.99 | -11.13 |
| 1.245 | - | - | - | - |

In Table 4 we compare the results from the two HFB codes for the $^{120}_{50}$Sn isotope. All observables agree very well. The apparent "disagreement" in the proton Fermi level $\lambda_p$ is really an artifact: the pairing gap vanishes at the magic proton number $Z = 50$ resulting in an ill-defined Fermi energy. The two codes use different prescriptions for calculating $\lambda_p$ in the trivial case of no pairing. HFB+THO accepts the last occupied equivalent single-particle energy as $\lambda_p$ in this no pairing case, whereas the Basis-Spline code takes the average of the last occupied and first unoccupied equivalent single-particle energy levels.

Deformations, dripline and pairing properties

Recently, triple-gamma coincidence experiments have been carried out with Gammasphere at LBNL [105] which have determined half-lives and quadrupole deformations of the neutron-rich $^{102,104}Zr$ isotopes. The isotopes from that region are produced in the pro-

cess of fission of transuranic elements and have been studied via $\gamma$-ray spectroscopy techniques. These medium-mass nuclei are among the most neutron-rich isotopes ($N/Z \approx 1.6$) for which spectroscopic data are available. Very large prolate quadrupole deformations ($\beta_2 = 0.43, 0.45$) are found for the $^{102,104}$Zr isotopes. Furthermore, the laser spectroscopy measurements [99] for the Zirconium isotopes have yielded precise rms-radii in this region. Recently, an experiment has been carried out to measure the mass of the $^{104}$Zr isotope [101]. It is therefore of a great interest to compare these data with the predictions of the self-consistent HFB mean field theory.

In radial ($r$) direction, the lattice in the HFB-2D-LATTICE code extends from $0-15$ fm, and in symmetry axis ($z$) direction from $-15, ..., +15$ fm, with a lattice spacing of about 0.8 fm in the central region. Angular momentum projections $\Omega = 1/2, 3/2, ..., 21/2$ were taken into account. Calculations performed with the HFB-2D-THO code used 20 transformed harmonic oscillator shells. Figure 17 shows the calculated two-neutron separation energies for the Zirconium isotope chain. The two-neutron separation energy is defined as

$$S_{2n}(Z,N) \;=\; E_{bind}(Z,N) \;-\; E_{bind}(Z,N-2)\;. \tag{161}$$

Note that in using this equation, all binding energies must be entered with a positive sign. The position of the two-neutron dripline is defined by the condition $S_{2n}(Z,N) \;= 0$, and nuclei with negative two-neutron separation energy are unstable against the emission of two neutrons. As one can see both methods (HFB-2D-THO and HFB-2D-LATTICE) are in excellent agreement for the two-neutron separation energy for the entire isotope chain. Particularly, the $^{122}$Zr isotope is predicted in both calculations as the dripline nucleus. In addition, we also give a comparison with the latest experimental data, available only up to the isotope $^{110}$Zr [106]. As it is shown on Fig. 17 the separation energy values obtained from the experiment are somewhat larger than the theoretical calculations although the trend remains the same.

In Fig. 18 we compare the intrinsic proton and neutron quadrupole moments calculated with the lattice code and the THO code. Available experimental data [105] are also given. Generally, we observe a nearly perfect agreement between the two codes as well as with the experiment. The deformations (for neutrons ) in terms of the deformation parameter $\beta_2$ for those nuclei, namely for the $^{102-112}$Zr isotopes range from $\beta_2$=0.42 to $\beta_2 = 0.47$. Both

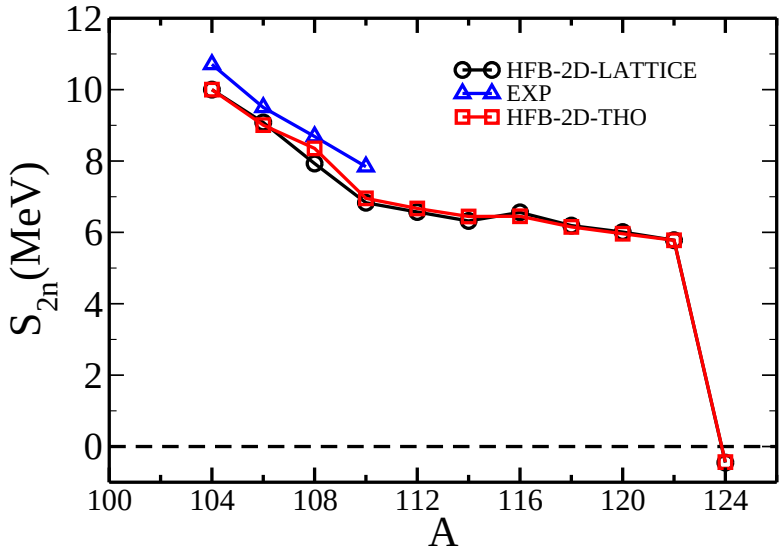


Figure 17: Two-neutron separation energies for the neutron-rich Zirconium isotopes. The dripline is located where the separation energy becomes zero. The $^{122}$Zr isotope is the last stable nucleus against two neutron emission.

the Basis-Spline lattice code and the HFB-2D-THO code predict the $^{112}$Zr isotope to have the largest ground state deformation. For mass numbers larger than 112 (Table. 5), we observe a transition to spherical ground state shape. This phenomenon had been also found in calculations performed by Möller et al. [107] (Finite Range Droplet Model calculations (FRDM)) and in Relativistic Mean-Field calculations by Lalazissis et al. [54]. We depict this comparison in Fig. 19 . Experimental deformations for protons are available for two isotopes, $^{102}$Zr and $^{104}$Zr [105]. Calculations agree with the experiment reasonably well and give $\beta_2$ values of 0.42,0.43 while the experiment predicts $\beta_2^{102}$=0.42, $\beta_2^{104}$=0.45.

In Fig. 20 we compare the root-mean-square radii of protons and neutrons predicted by the LATTICE code and the THO code. Both codes give nearly identical results for the whole isotope chain. Only one experimental data point is available, the proton rms radius of $^{102}$Zr [99]. The experiment yields a proton rms radius of 4.54 fm while the HFB codes predict a value of 4.45 fm (HFB-2D-LATTICE) and 4.46 fm (HFB-2D-THO). The difference between theory and experiment is quite small, of order 2%. We can clearly observe the presence of the neutron-skin manifested by the large differences between the neutron and proton rms

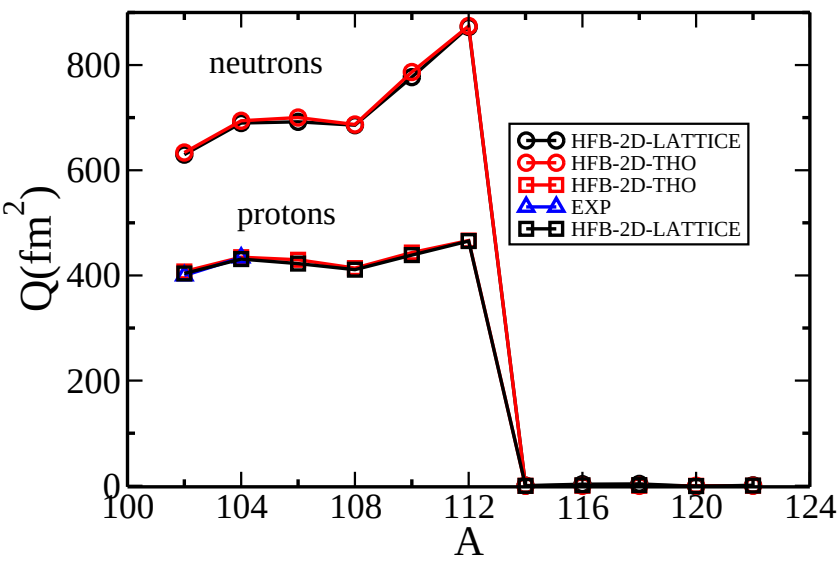


Figure 18: Intrinsic quadrupole moments for protons and neutrons.

radii for all of the isotopes in the chain. As expected the neutron-skin becomes "thicker" as we approach the dripline. Starting at the mass number A=114 up to the dripline the nuclei prefer a spherical ground state shape (Fig. 18) which results in a sudden shrinking of the rms radius at A=114.

Table 5: The calculated HFB observables for the most deformed $^{112}$Zr isotope. The columns display binding energy (BE), deformation parameter $\beta_2$ for neutrons and protons ($\beta_2^n$,$\beta_2^p$), rms-radii ($r_n$,$r_p$,$r_{total}$), average pairing gaps ($\Delta_n, \Delta_p$), pairing energy for neutrons and protons ($PE_n$,$PE_p$ ), and Fermi levels ($\lambda_n, \lambda_p$).

| BE(MeV) | $\beta_2^n$(fm$^2$) | $\beta_2^p$(fm$^2$) | $\beta_2^{tot}$(fm$^2$) | $r_n$(fm) | $r_p$(fm) | $r_{tot}$(fm) |
|---|---|---|---|---|---|---|
| -901.90 | 0.47 | 0.45 | 0.47 | 4.88 | 4.58 | 4.77 |
| $\Delta_n$(MeV) | $\Delta_p$(MeV) | $PE_n$(MeV) | $PE_p$(MeV) | $\lambda_n$(MeV) | $\lambda_p$(MeV) | - |
| 8.41 $10^{-2}$ | 8.01 $10^{-2}$ | $-4.53$ $10^{-2}$ | $-3.33$ $10^{-2}$ | $-2.82$ | $-16.22$ | - |

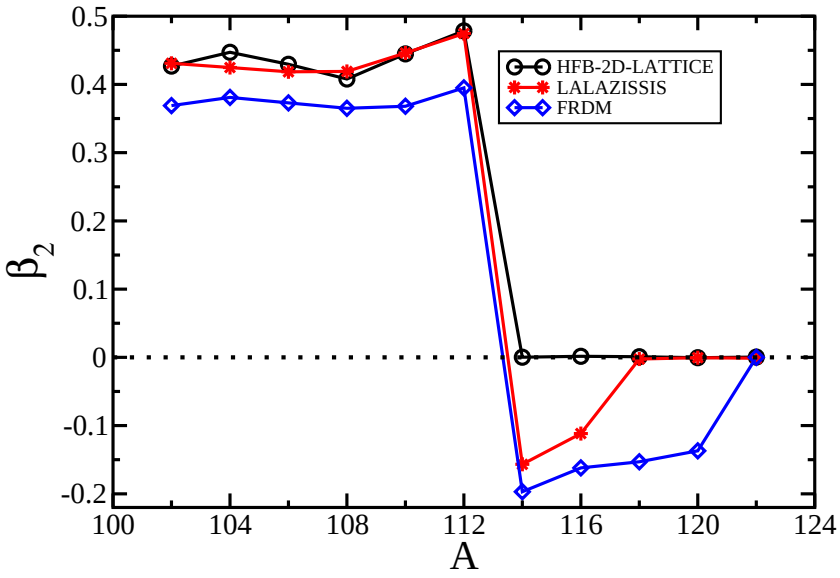


Figure 19: Mass quadrupole parameter $\beta_2$ comparison for neutrons. Calculations by Lalazissis et al. (RMF), HFB-2D-LATTICE and Möller et al. (FRDM) ($\beta_2$ total is shown ).

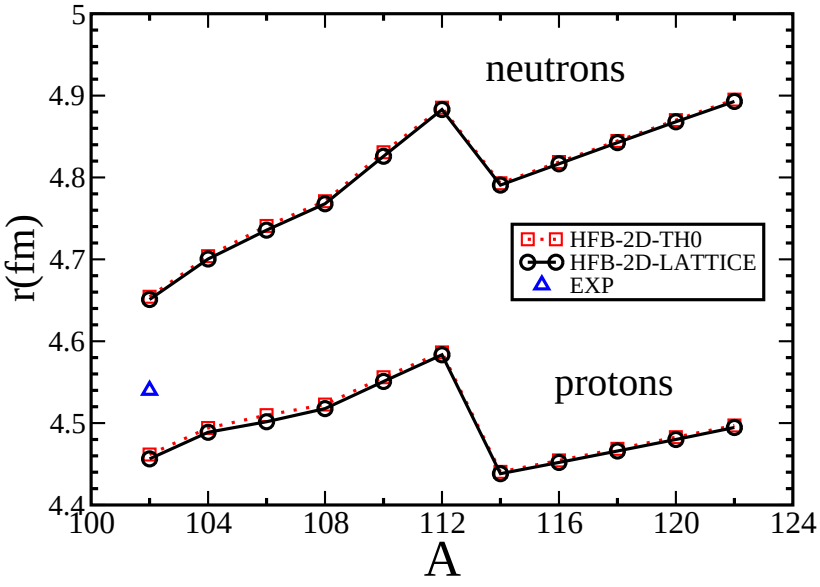


Figure 20: Root-mean-square radii for the chain of Zirconium isotopes.

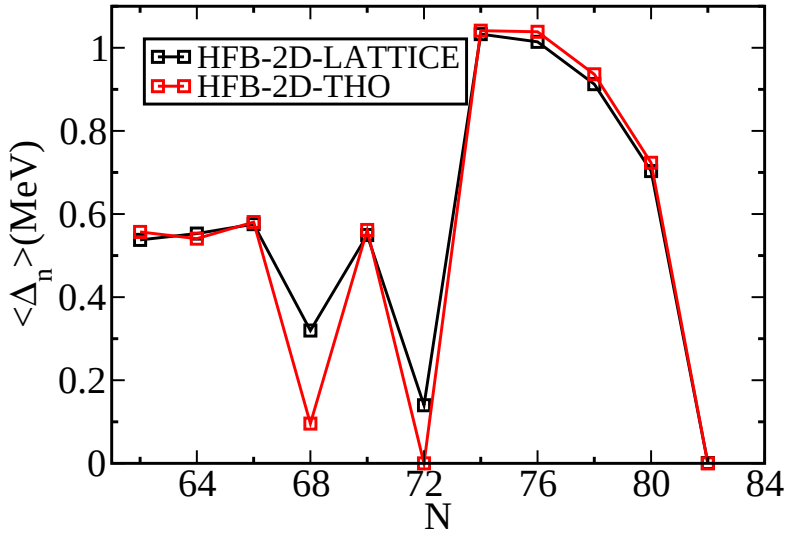


Figure 21: Average neutron pairing gap for the chain of Zirconium isotopes.

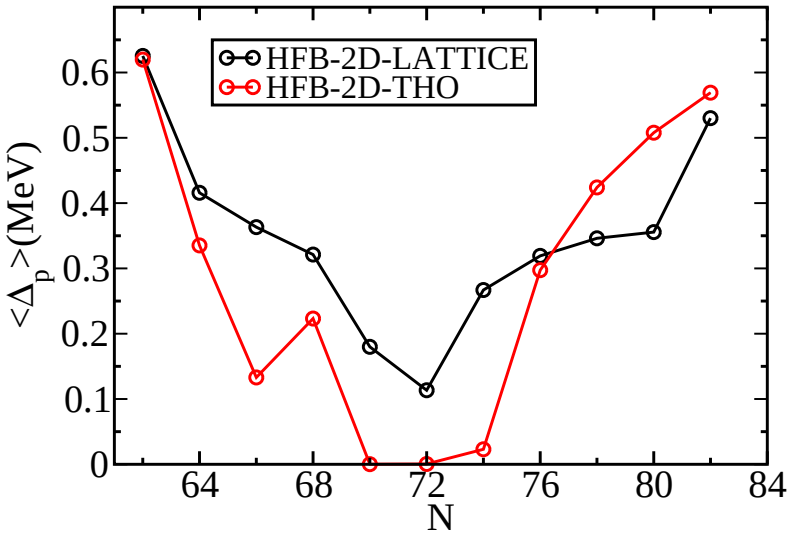


Figure 22: Average proton pairing gap for the chain of Zirconium isotopes.

Fig. 21 and Fig. 22 depict the average pairing gaps for neutrons and protons. Generally, both HFB codes show the same trend for the pairing gaps as a function of neutron number; the agreement is noticeably better for neutrons. The two HFB codes predict a small value of the neutron pairing gap for the $^{112}$Zr isotope which on the other hand has the largest prolate deformation (Fig. 18) among the calculated nuclei. Coincidentally, the dripline turns out to be at the neutron magic number (N=82) and, as expected, both codes yield a pairing gap of zero for the $^{122}$Zr isotope. The differences observed in the neutron and proton pairing gaps can be attributed to different approaches in representing the continuum states, namely discretized continuum states in the HFB-2D-LATTICE versus positive energy bound states in a stretched harmonic oscillator. In general, the pairing gap is the one observable which is most sensitive to the properties of the continuum states. In addition, two approaches use different methods for representing differential operators as well as calculating the Coulomb potential.

Density studies

In this section we focus on the normal and pairing densities for the selected isotopes. In Fig. 23 we show a contour plot of normal densities for protons and neutrons for the $^{110}$Zr isotope. It is the last deformed isotope with a significant value of the pairing gap for neutrons, (Fig. 21), therefore it is possible to show plots of both normal and pairing densities. The results obtained for the neutron normal and pairing densities (Figs. 23 and 24) clearly exhibit a large prolate deformation. The normal density for neutrons (Fig. 23) is concentrated in the region that extends from 0 fm to 2 fm in $r$-direction and from $-5$ fm to $+5$ fm in $z$-direction. Within this region, we find an enhancement in the neutron density with a shape that resembles the figure "eight". In comparing the neutron to the proton density, one notices that both the center of the nucleus and the surface is dominated by neutrons. The pairing density for neutrons in Fig. 24 shows a richer structure than the normal density. This quantity describes the probability of correlated nucleon pair formation with opposite spin projection, and it determines the pair transfer formfactor. We can see that most correlated pair formation takes place in the four closed shaped structured areas near the z-axis. We may conclude that neutrons dominate the pairing properties of this nucleus

which is a consequence of $\Delta_n$ being larger than $\Delta_p$. A similar argument applies to normal densities (N>Z) , yet the difference between neutrons and protons is more pronounced in case of the pairing densities. A graph depicting the single-particle energy spectrum of the pairing density for the $^{104}Zr$ isotope has been published in Ref. [84]. In Figs. 25 and 26 we show plots of normal densities as a function of the distance from the center, $r = \sqrt{\rho^2 + z^2}$. For a given value of $r$, the density is single-valued for a spherical nucleus and multi-valued for a deformed density distribution because in the latter case different combinations of lattice points $z_i$ and $\rho_j$ give rise to the same $r$-value.

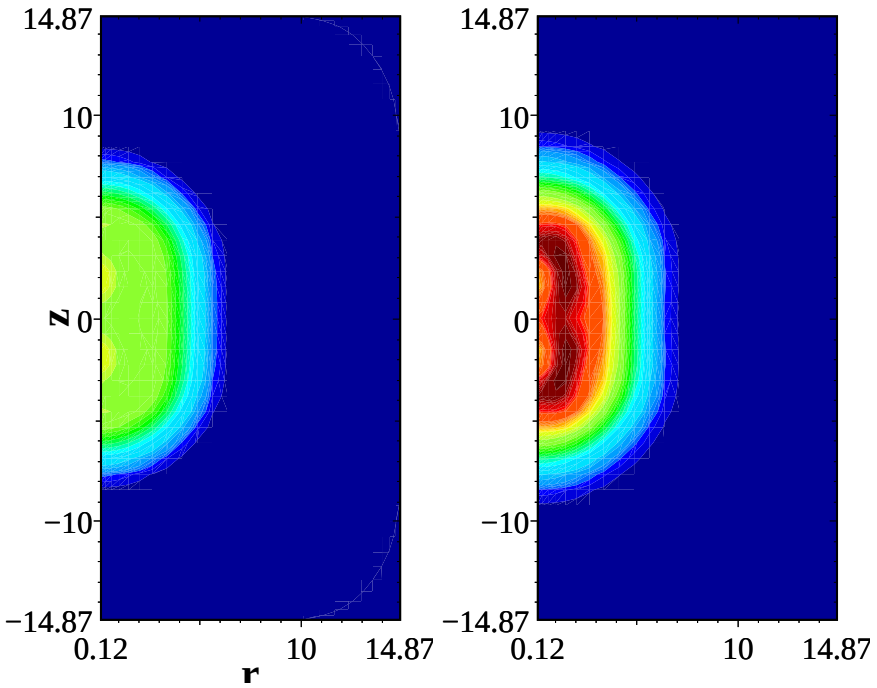


Figure 23: Contour plots of the $^{110}$Zr normal densities, for protons (left) and neutrons (right). Densities are shown as a function of the cylindrical coordinates $(r, z)$, where $z$ is the symmetry axis. The scale ranges from 9.7 $\cdot 10^{-2}$ fm$^{-3}$ (dark red), through 5.0 $\cdot 10^{-2}$ (light green), 3.0 $\cdot 10^{-3}$ (light blue), to 3.4 $\cdot 10^{-15}$ (dark blue) .

In Fig. 25 we compare three different calculations of the neutron normal density for the most deformed $^{112}$Zr isotope. The plot on a logarithmic scale shows that the density distribution predicted by the HFB-2D-THO and HFB-2D-LATTICE codes is deformed for

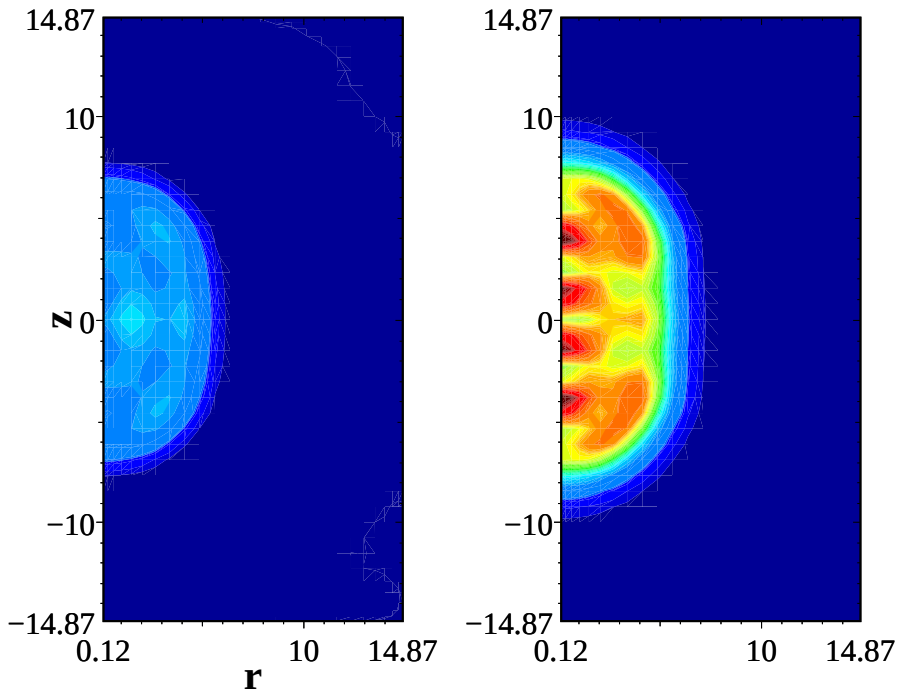


Figure 24: Contour plots of the $^{110}$Zr pairing densities, for protons (left) and neutrons (right). The densities are shown as a function of the cylindrical coordinates $(r, z)$, where $z$ is the symmetry axis. The scale ranges from 9.0 $\cdot 10^{-3}$ fm$^{-3}$ (dark red), through 4.9 $\cdot 10^{-3}$ (light green), 8.0 $\cdot 10^{-4}$ (light blue), to 9.3 $\cdot 10^{-14}$ (dark blue) .

almost all values of the distance from the nuclear center, $r$. At very large distances the densities become less deformed since nuclear potentials go to zero and HFB equations lead to a spherical asymptotic solution. Fig. 25 also shows for comparison the HFB-2D-HO result as an illustration of the shortcomings of the pure harmonic oscillator basis calculations to reproduce density distributions asymptoticly at very large distances. One can see its too rapid decay beyond distances of about 12 fm. Clearly, the pure harmonic oscillator basis calculations cannot represent properly density asymptotic for nuclei close to the neutron drip line. Neutron and proton normal densities for the drip-line nucleus $^{122}$Zr are shown in Fig. 26. From the single-valued plot as a function of $r = \sqrt{\rho^2 + z^2}$ one can immediately conclude that both neutron and proton normal densities are spherical. Another feature is the strong neutron enhancement at the center and a corresponding depletion in the proton density, which is due to occupied (unoccupied) $s$ orbitals near the Fermi level.

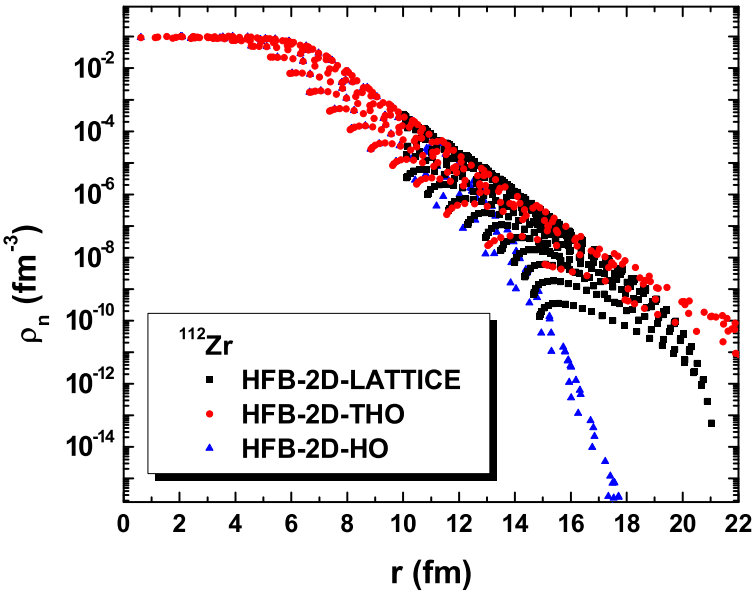


Figure 25: Logarithmic plot of the normal neutron density for the most deformed isotope $^{112}$Zr as a function of the distance $r = \sqrt{\rho^2 + z^2}$.

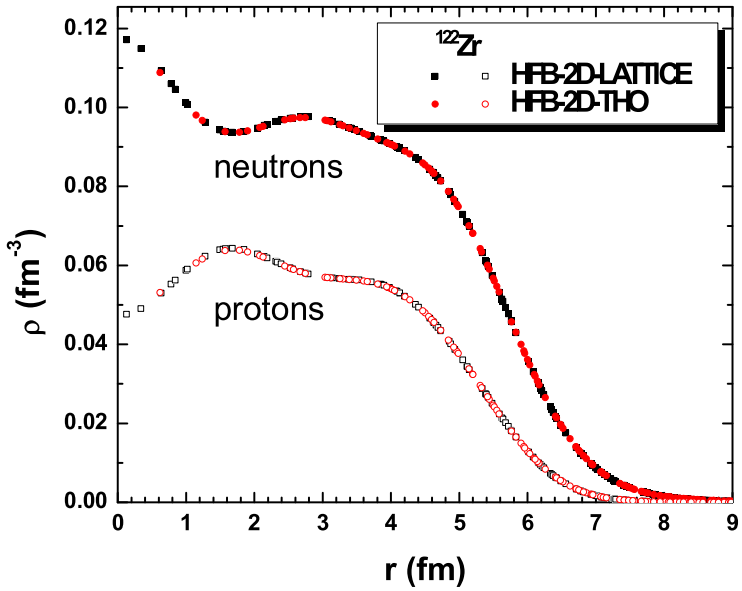


Figure 26: Linear plot of the normal neutron and proton density for the dripline nucleus $^{122}$Zr as a function of distance $r = \sqrt{\rho^2 + z^2}$. Comparison between the HFB-2D-THO code and the HFB-2D-LATTICE code.

We also note that the neutron density is substantially larger than the proton density for all values of $r$.

The convergence study of the HFB observables

In this section we focus on the convergence studies of the HFB observables (see section 3.1.3). In Fig. 27 are plotted the average neutron pairing gap $\langle\Delta_n\rangle$ and deformation parameter $\beta_2$ for neutrons as a function of the iteration number. As one can observe

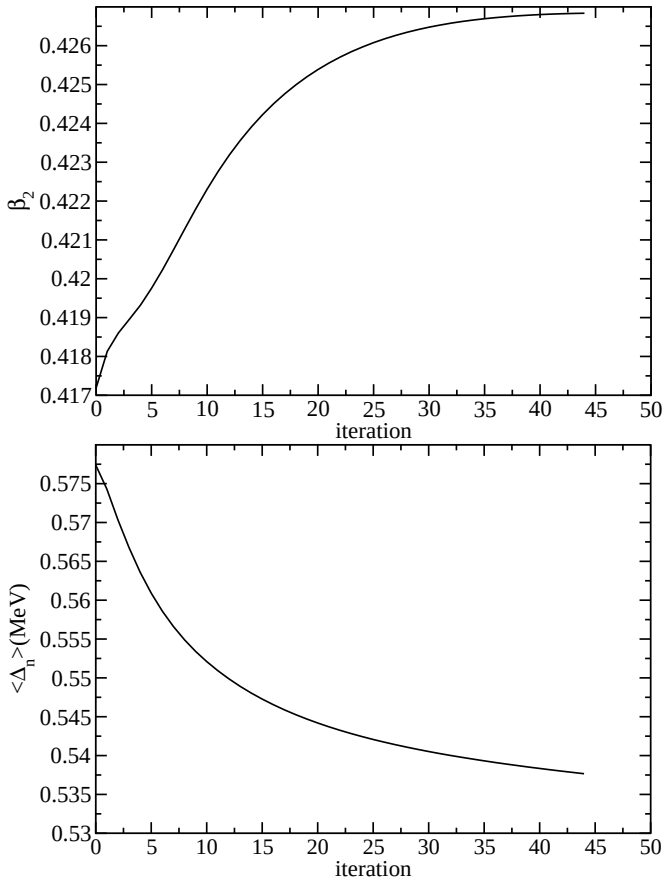


Figure 27: Convergence studies. Shown are the average neutron pairing gap $\langle\Delta_n\rangle$ and deformation parameter $\beta_2$ for neutrons for the $^{102}$Zr isotope as a function of the iteration number.

both observables converge asymptotically to the final value after about forty iterations.

These two selected observables exhibit two different kinds of the monoticity; the pairing gap $\langle\Delta_n\rangle$ monotically decreases while the deformation parameter $\beta_n$ increases. Our goal is to plot simultaneously few selected observables in order to observe and compare the rate at which these quantities reach the converged value. For the quantity of choice $f$ we plot it's percentage relative error versus the iteration number

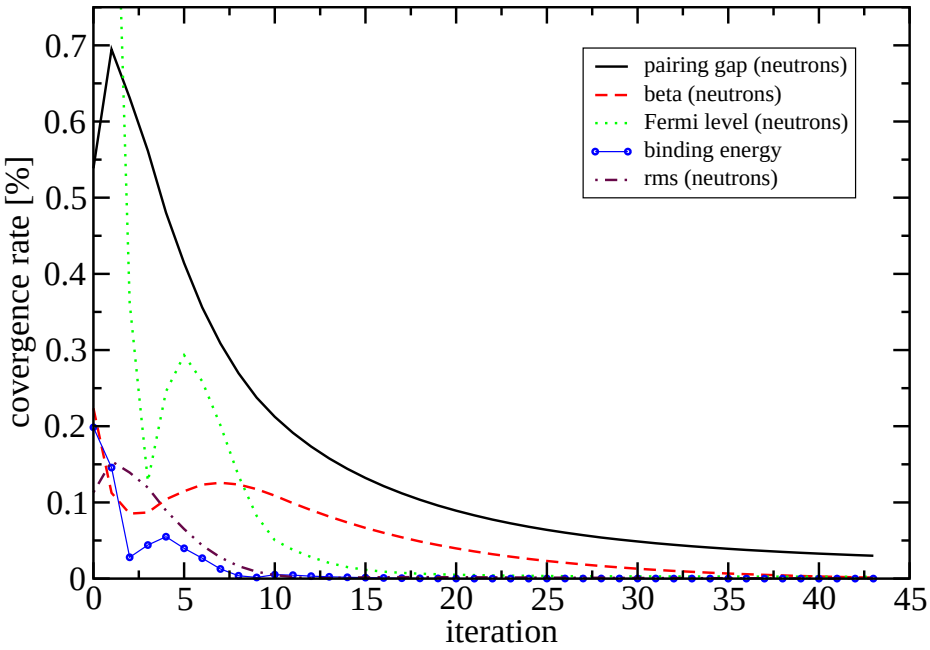


Figure 28: Convergence studies for the $^{102}$Zr isotope. Plotted is the relative percentage error of the five selected HFB observables: binding energy, neutron Fermi level, neutron rms-radius, deformation parameter $\beta_2$ for neutrons and average neutron pairing gap $\langle\Delta_n\rangle$.

$$\frac{\Delta f}{f}\times 100\% \equiv \frac{||f_{iter+1}|-|f_{iter}||}{|f_{iter+1}|}\times 100\%. \tag{162}$$

We take also an absolute value of all quantities to be able to plot simultaneously the selected observables regardless of the character of it's monoticity or sign. The results for the two neutron-rich isotopes $^{102,106}$Zr are shown in Figs. 28 and 29. We plot the most important observables i.e. binding energy, Fermi level, pairing gap, deformation parameter and rms-radius as the function of the iteration number. As can be seen, the observables converge at

different rates. Another noticeable feature, is that we can observe two families of observables; the "slow" ones, i.e. the pairing gap and deformation parameter $\beta_2$, and the "fast" ones, i.e. binding energy, rms-radius and the Fermi level. This is a fact one should keep in mind when making decisions about the number of required iterations.

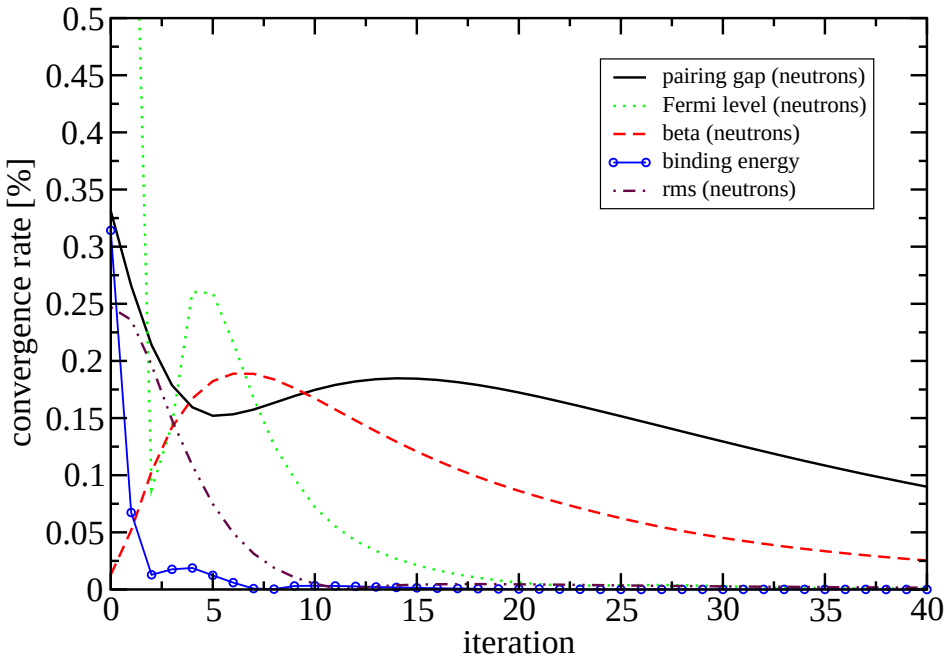


Figure 29: Convergence studies for the $^{106}$Zr isotope. Plotted is the relative percentage error of the five selected HFB observables: binding energy, neutron Fermi level, neutron rms-radius, deformation parameter $\beta_2$ for neutrons and average neutron pairing gap $\langle\Delta_n\rangle$.

## 5.2 Calculations for Kr isotope chain .

This section addresses the ground state properties of the neutron-rich Krypton isotopes ($Z = 36$) up to the two-neutron dripline. The isotope chain calculations start from the $^{104}$Kr isotope up to the dripline nucleus $^{116}$Kr. In our calculations we use the grid size, maximum magnetic number $j_z = 21/2$, pairing strength $V_0$ as in case of Zr isotope chain. We find a shape transition from the prolate deformation into oblate and also various coexisting nuclear shapes in calculated isotope chain. We compare our results with the Finite Range Droplet Model calculations (FRDM) [107] and with the Relativistic Mean-Field calculations by Lalazissis et al. [54].

### 5.2.1 Bulk properties.

Figure (30) shows the calculated two-neutron separation energies for the Krypton isotope chain (Eq. 161).

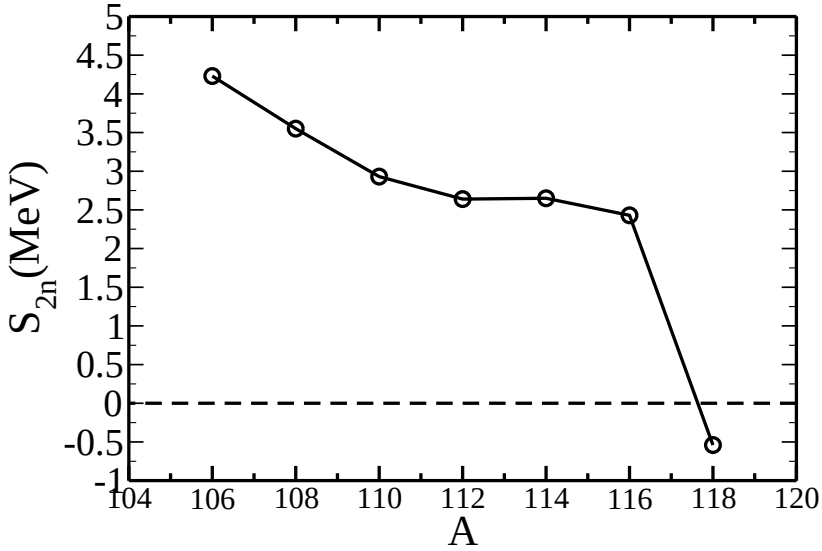


Figure 30: Two-neutron separation energies for the neutron-rich Krypton isotopes. The dripline is located where the separation energy becomes zero. The $^{116}$Kr isotope is the last stable nucleus against two neutron emission.

As can be seen the dripline is found to be at $A = 116$.

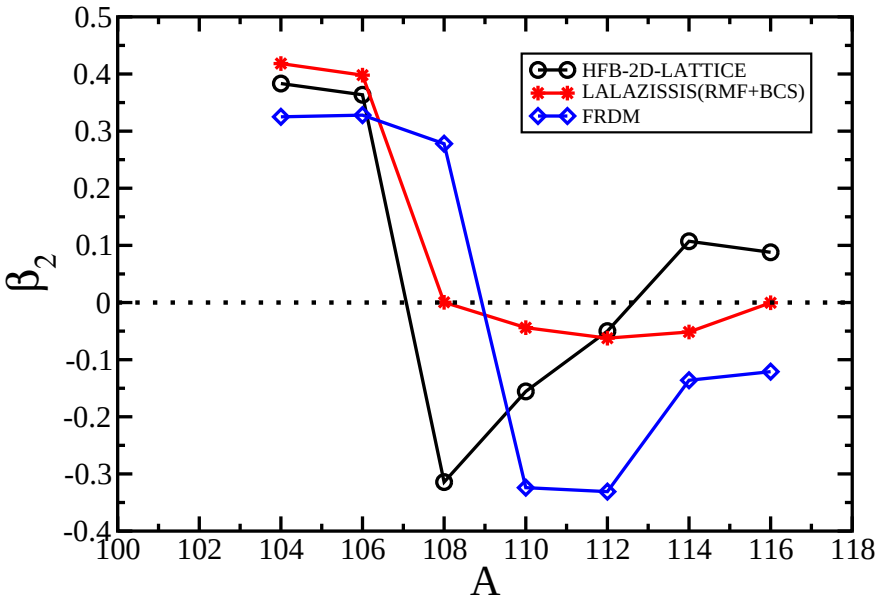


Figure 31: Mass distribution quadrupole parameter $\beta_2$ for neutrons. Comparison of calculations by Lalazissis et al. (RMF+BCS), HFB-2D-LATTICE and Möller et al. (FRDM) ($\beta_2$ total is shown ).

Compared to the two-neutron separation energy for the Zr isotope chain for the same mass number (Fig. 17 ) the energy values are on average smaller by about 4 MeV. This observed energy difference occures naturally due to the absence of the four protons. Experimental data for the Krypton isotopes chain calculated in this work is unavailable. It is due to experimental difficulties to reach the region of the relatively large N/Z ratios. The most neutron-rich Zirconium isotope for which experimental data is available is $^{110}$Zr with N/Z$\approx$ 1.75. Our Krypton isotope chain starts from the $^{104}$Kr with N/Z $\approx$ 1.8. Krypton isotopes similarly as in case of Zirconium chain reveal variety of shapes. The deformations in Fig.31 range from $\beta_2$=0.38 ($^{104}$Kr), through $\beta_2$=-0.31 ($^{108}$Kr-see Fig. 33) up to $\beta_2$=0.1 ($^{110}$Kr) . In particular we can observe the shape change from the prolate deformation into the oblate at the mass number A=108. The shape transition is also indicated by two other models, namely the Finite Range Droplet Model calculations (FRDM) [107] and by the Relativistic Mean-Field calculations by Lalazissis et al. (RMF+BCS) [54]. We can observe the same trend for the depicted three models, yet not a perfect agreement. The discrepancies between our HFB-2D-LATTICE code and the former two methods are expected and

Table 6: Shape coexistence studies. Shown are the deformations $\beta_2^{n/p}$ for neutrons/protons and binding energy for selected isotopes. The results are showed for three possible minima (1st,2nd,3rd). The first column contains the ground state minimum.

| isotope | 1st min. | | | 2nd min. | | | 3rd min. | | |
|---|---|---|---|---|---|---|---|---|---|
| | $\beta_2^n$ | $\beta_2^p$ | E[MeV] | $\beta_2^n$ | $\beta_2^p$ | E[MeV] | $\beta_2^n$ | $\beta_2^p$ | E[MeV] |
| $^{104}$Kr | 0.38 | 0.35 | -821.41 | 0.09 | 0.1 | -816.44 | -0.26 | -0.25 | -821.30 |
| $^{106}$Kr | 0.36 | 0.35 | -825.65 | - | - | - | -0.29 | -0.28 | -825.29 |
| $^{110}$Kr | -0.15 | -0.15 | -832.14 | 0.07 | 0.08 | -830.45 | 0.40 | 0.36 | -829.94 |

can be understood as the result of the simplistic BCS model [56] of pairing interaction used by FRDM and RMS calculations, which is known to break down in the vicinity of the dripline. In Table (6) we study the shape coexistence phenomenon present for the Kr isotope chain. As can be seen, the selected isotopes $^{104,106,110}$Kr can have several different coexisting $J^\pi = 0^+$ states with stable deformed shapes. These deformations correspond to the local minima of the binding energy as the function of the deformation, where the ground state minimum has the lowest binding energy. What can be noticed is that the energy difference between the prolate and oblate minimum for $^{104,106}$Kr isotopes is very small of the order of 10-40 keV. a As anticipated, the rms-radii studies in Fig. 32 show the neutron-skin phenomenon manifested as the large difference between proton and neutron rms-radius. A sudden radius drop at A=108-110 falls exactly into the mass region of the the shape change occurrence (see Fig. 31). The comparison with Relativistic Mean-Field calculations by Lalazissis et al. [54] clearly show the shortcomings of the BCS model based treatment of pairing interaction, which introduces a systematically larger radius for neutrons. This effect has also been seen in calculations of the Sulfur isotopes by Oberacker et al. (fig.4) [83] and also in the Zr isotopes chain (fig. 20). In Figures 36 and 37 we show the average pairing gaps for neutrons and protons respectively. For instance, the relatively larger neutron pairing gap for $^{108}$Kr ($\Delta_n > \Delta_p$) implies also a larger neutron pairing density what is shown in Fig. 34. In the opposite case of $^{104}$ Kr, when $\Delta_n < \Delta_p$, it is more probable to find the two protons at the same position with the opposite spin projection (Fig. 35 ).

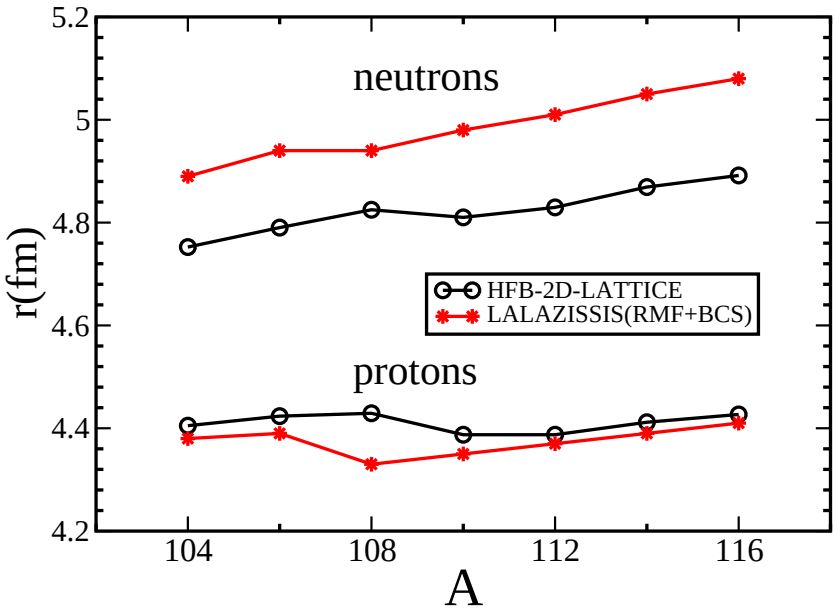


Figure 32: Root-mean-square radii for the chain of Krypton isotopes.

Another interesting pairing quantity which we have studied is the "pairing density spectral distribution" $P_{n\Omega q}$ plotted in Fig.38

$$P_{n\Omega q} = -\int_0^\infty r dr \int_{-\infty}^\infty dz \sum_{\sigma=\uparrow\downarrow} \Psi^{(2)}_{n\Omega}(r,z,\sigma,q)\Psi^{(1)*}_{n\Omega}(r,z,\sigma,q). \tag{163}$$

The quantity $P_{n\Omega q}$ carries an information about the contribution of a given quasiparticle state $|n\Omega q\rangle$ to the neutron pairing density [82].

As we can notice the function $P_{n\Omega q}$ is peaked around the Fermi energy $\lambda_n = -1.49$ MeV, what tells us that the states near the Fermi level contribute most to the pairing density. In calculating the observables we include states up the 60 MeV in the equivalent single particle energy $\varepsilon_n$. The plot in Fig. 38 reassures us that the contribution to the pairing density above the energy 60 MeV can be neglected (contribution of the order of $\sim 10^{-3}$). Thus, the cut-off at the energy of 60 MeV is fully justified.

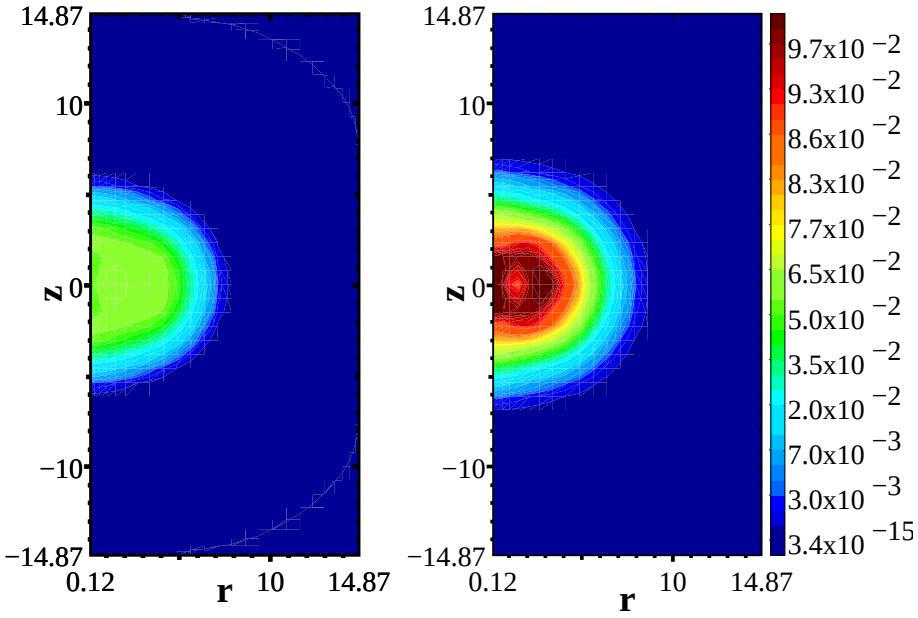


Figure 33: Contour plots of the $^{108}$Kr normal densities, for protons (left) and neutrons (right). Densities are shown as a function of the cylindrical coordinates $(r, z)$, where $z$ is the symmetry axis. Note the oblate shape, with $\beta_2$=-0.31.

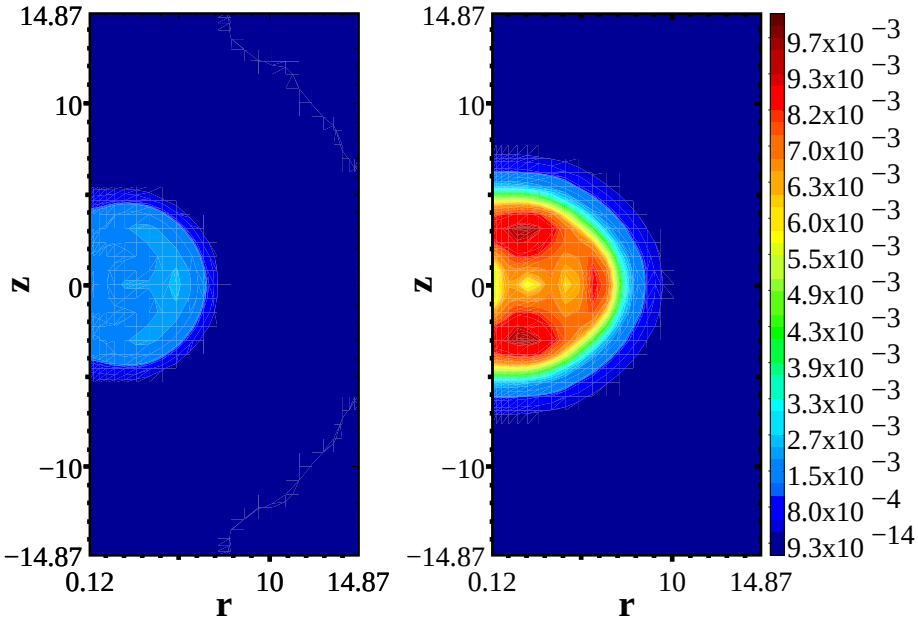


Figure 34: Contour plots of the $^{108}$Kr pairing densities, for protons (left) and neutrons (right). The densities are shown as a function of the cylindrical coordinates $(r, z)$, where $z$ is the symmetry axis. The oblate quadrupole deformation is $\beta_2 = -0.31$.

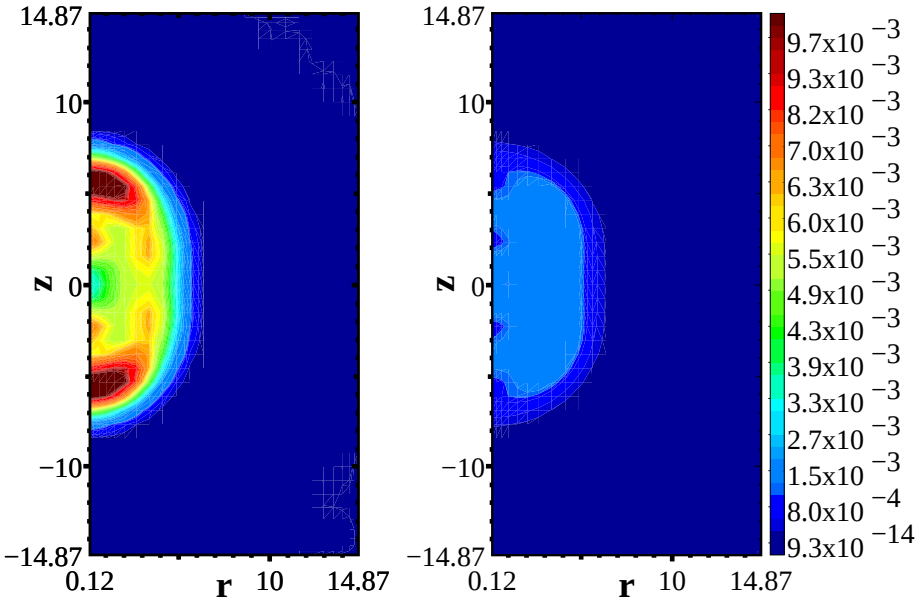


Figure 35: Contour plots of the $^{104}$Kr pairing densities, for protons (left) and neutrons (right). The densities are shown as a function of the cylindrical coordinates $(r, z)$, where $z$ is the symmetry axis. The prolate quadrupole deformation is $\beta_2$=0.38.

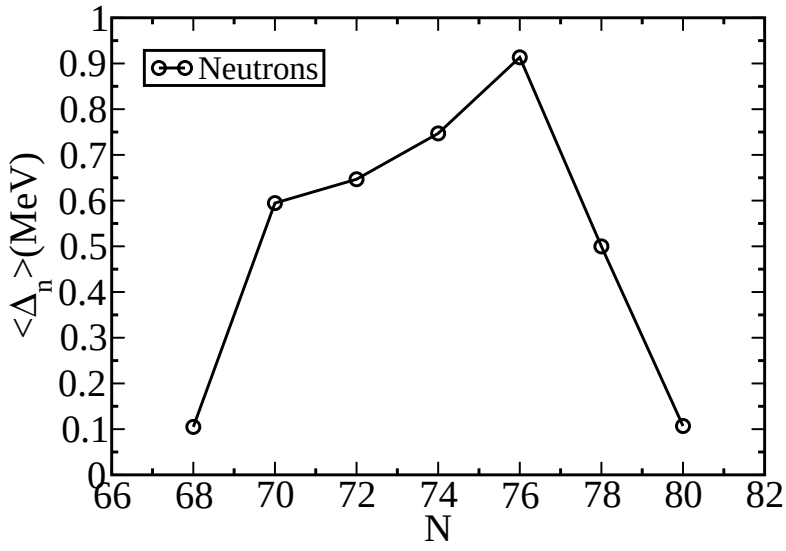


Figure 36: Average neutron pairing gap for the chain of Krypton isotopes.

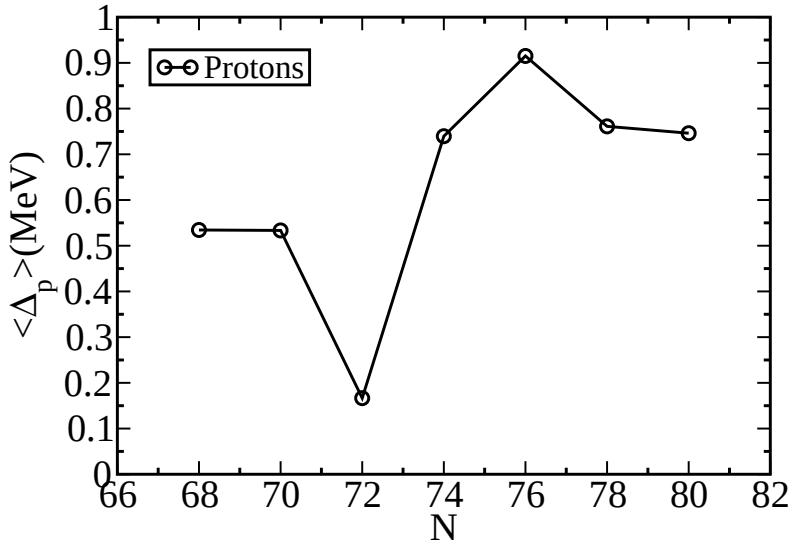


Figure 37: Average proton pairing gap for the chain of Krypton isotopes.

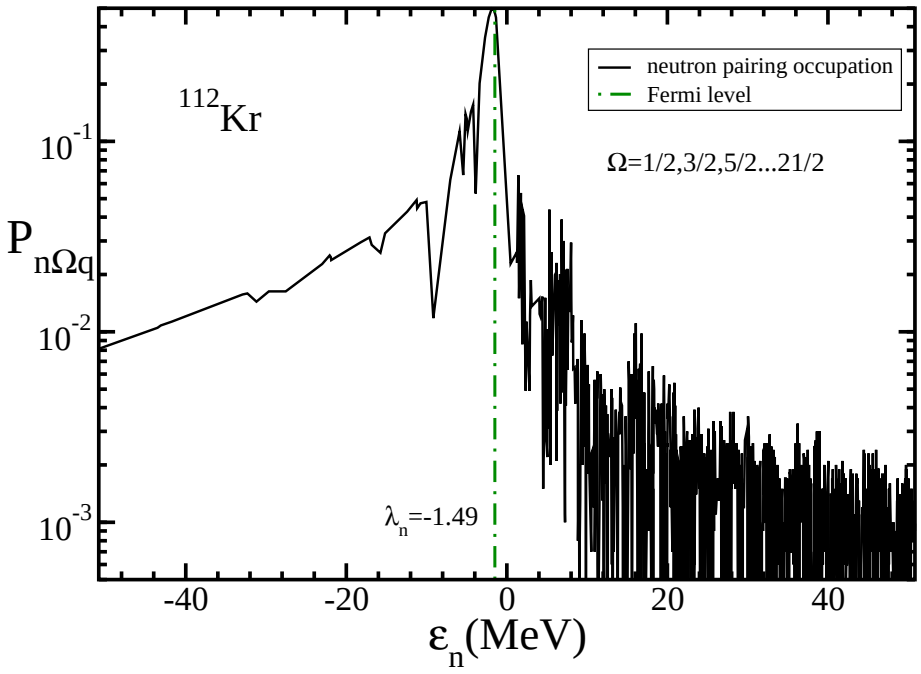


Figure 38: Neutron (q=-$\frac{1}{2}$) pairing density spectral distribution $P_{n\Omega q}$ as a function of the equivalent single particle energy $\varepsilon_n$ for the $^{112}$Kr isotope. Plotted is the contribution from all angular momentum projection numbers $\Omega = 1/2, 3/2, \ldots, 21/2$ up to the energy cut-off of $\varepsilon_n = 60$ MeV.

# CHAPTER VI

# CONCLUSIONS

This work concentrates on the 2D-lattice coordinate-space HFB calculations for neutron-rich nuclei. The 2D axially symmetric coordinate-space calculations are a natural continuation of the 1D coordinate-space calculations by Dobaczewski et al. [81]. In the lattice approach, no region of the spatial lattice is favored over any other region: the well bound, weakly bound, and (discretized) continuum states can be represented with the same accuracy. Our method does not have any limitations in taking into account the continuum states. The arbitrary cut-off in the equivalent single-particle energy is possible (currently 60 MeV), thanks to the utilization of the Basis-Spline techniques [93, 89, 108, 90, 91, 92] in representing the differential operators. In this sense the lattice calculations are considered the most accurate, as they do not impose any approximations (e.g. low-energy cut-off or harmonic oscillator basis expansion methods).

As of today, our 2D lattice HFB code is a fully functional and highly optimized FORTRAN 95 program suitable for parallel supercomputers. The applied parallelization scheme for different angular momentum numbers $\Omega$ and different isospins (proton/neutron) enabled us to speed up calculations for $\Omega_{max} = \frac{21}{2}$ almost 22 times. Furthermore, nearly four times gain in the speed was achieved by diagonalization of the smaller reduced Hamiltonian. Clearly, the current code advanced in speed $\sim$88 times compared to the older versions. The reduction of the size of the diagonalized Hamiltonian was accomplished by applying the unitary transformation to the original Hamiltonian, which decouples the HFB equations (sec:3.1.4). A smaller Hamiltonian matrix allows us to reach heavier systems e.g. calculations for $^{238}$U are feasible at reasonable computation time. It is also important to mention that the Hamiltonian matrix of the reduced Hamiltonian is a general positive definite matrix compared to the general nondefinite one of the original Hamiltonian. This property makes a search for an alternative to the direct diagonalization methods of solving the HFB problem much easier.

Moreover, it has been found that the precise pairing strength $V_0$ depends on the method

used (lattice, THO) and cannot be taken over from the calculations of others in order to have comparable results. In section (sec:5.1) the fit to the properties of the $^{120}$Sn isotope was made providing the new value of $V_0$.

Furthermore, we explored the neutron-rich $A \sim 100$ mass region resulting in the calculations of properties of the two isotope chains, namely $_{36}$Kr and $_{40}$Zr.

The results obtained for the Zr isotope chain agree remarkably well with the calculations by Stoitsov et al. [79] giving the reassurance that both codes, namely our HFB-2D-LATTICE code and the Transformed Harmonic Oscillator (THO) approach are fully functional. In particular both codes agree on the dripline nucleus and predict the same shape change from prolate into spherical. The comparison of rms-radii and neutron densities show also the presence of a neutron skin in the neutron-rich Zr isotope chain. However, we find minor differences in the pairing gaps predicted by both methods; this is expected because $\Delta_{n,p}$ is sensitive to the continuum states. Finally, the convergence studies based on the two selected Zr isotopes exhibit two families of observables, the "fast" ones converging fairly quickly to the final value and the "slow" ones, which require many more iterations in order to converge.

Similarly, as in case of Zirconium we find in studied Kr isotope chain a shape change from the prolate deformation into an oblate, which is reflected in the neutron and proton rms-radius as well. The results obtained for the chain of Kr isotopes confirm that the mass region of $A \sim 100$ is the area of the competition between various coexisting nuclear shapes. In particular we found several different coexisting $J^\pi = 0^+$ states in selected three Kr nuclei. The usefulness of the average pairing gap quantity in studying the pairing densities was demonstrated. The plot of the neutron pairing density spectral distribution vs. equivalent single-particle energy demonstrates that the 60 MeV cut-off energy limit is sufficient.

To summarize, we have numerically solved the HFB problem on the 2D lattice without any approximations. As mentioned before, the lattice calculations are considered to be the most accurate from the numerical point of view. Unfortunately, the size of the Hamiltonian matrix in two dimensions requires fairly large amount of CPU time. For this reason our code cannot provide a complete mass table of neutron-rich nuclei within a reasonable time frame. Such calculations are crucial in astrophysics.

As it was demonstrated in case of the Zr isotopes our HFB ground state results agree very well with the THO-calculations by Stoitsov et al., whose code is much faster. However, our lattice 2-D code provides a much better representation of continuum states which may be crucial in future calculations of excited states.

It is possible to generate ground state solution of several selected nuclei, which will serve as the input for the future time dependent calculations. Currently, our group focuses on the Time-Dependent-Hartree-Fock (TDHF) calculations of heavy-ion collisions. The 2D HFB lattice code will provide a base for the planned in the future Time-Dependent-Hartree-Fock-Bogoliubov (TDHFB) calculations for exotic nuclei.

REFERENCES


[1] http://www.ornl.gov/info/ornlreview/v34_2_01/search.htm/.

[2] RIA Physics White Paper, Technical report, RIA 2000 Workshop, Raleigh-Durham, NC, 2000.

[3] I. Tanihata , Nucl. Phys. **522**, 275c (1991).

[4] J. Enders, H. Kaiser, P. von Neumann-Cosel, C. Rangacharyulu, A. Richter, Phys. Rev. C **59**, R1851 (1999).

[5] J. Engel, S. Pittel, M. Stoitsov, P. Vogel and J. Dukelsky, Phys. Rev. C. **55**, 1782 (1997).

[6] John J. Cowan and Friedrich-Karl Thielemann , Physics Today **57**, 47 (2004).

[7] http://isolde.web.cern.ch/isolde/.

[8] http://www.triumf.info/.

[9] http://www.nscl.msu.edu/.

[10] http://www.phy.anl.gov/atlas/.

[11] http://www.phy.ornl.gov/hribf/.

[12] http://www.riken.go.jp/engn/.

[13] http://www-aix.gsi.de/.

[14] http://www.orau.org/ria/riatg/.

[15] A. Bohr and B.R. Mottelson, *Nuclear Structure* , W.A. Benjamin, INC., New York, Amsterdaam, 1969.

[16] W.D. Myers, W.J. Swiatecki , Nucl. Phys. **81**, 1 (1966).

[17] M.G. Mayer and J.H.D. Jensen, *Elementary Theory of Nuclear Shell Structure* , Wiley, New York, 1955.

[18] P. Navratil, G.P. Kamuntavicius and B.R. Barrett, Phys. Rev. C. **61**, 044001 (2000).

[19] P. Navratil and B.R. Barrett, Phys. Rev. C. **57**, 562 (1998).

[20] P. Navratil and B.R. Barrett, Phys. Rev. C. **54**, 2986 (1996).

[21] D.C. Zheng et al., Phys. Rev. C. **48**, 1083 (1993).

[22] B.R. Barrett, Nuclear. Physics News **13** (2003).

[23] P. Navratil, J.P Vary, and B.R. Barrett, Phys. Rev. Lett. **84**, 5728 (2000).

[24] P. Navratil and W.E. Ormand, Phys. Rev. Lett. **88**, 152502 (2002).

[25] J. Da Providencia and C.M. Shakin, Ann.Phys. (N.Y.) **30**, 95 (1964).

[26] P. Navratil and W.E. Ormand, Phys. Rev. C. **68**, 034305 (2003).

[27] J. Lomnitz-Adler, V.R. Pandharipande, and R.A. Smith, Nucl. Phys. **A361**, 399 (1981).

[28] K. Varga, Steven C. Peiper, Y. Suzuki, and R.B. Wiringa, Phys. Rev. C. **66**, 034611 (2002).

[29] J. Carlson, Phys. Rev. C. **36**, 2026 (1987).

[30] F. Coester , Nucl. Phys **7**, 421 (1958).

[31] F. Coester and H. Kummel, Nucl. Phys **17**, 477 (1960).

[32] D.J. Dean and M. Hjorth-Jensen , Phys. Rev. C. **69**, 054320 (2004).

[33] H. Kümmel, K.H. Lührmann, and J.G. Zabolitzky , Phys. Reports **36**, 1 (1970).

[34] B. Michaila and J.H. Heisenberg, Phys. Rev. C. **60**, 054309 (2000).

[35] D.R. Entem and R. Machleidt , Phys. Lett. B. **524**, 93 (2002).

[36] M. Hjorth-Jensen, T.T.S. Kuo and E. Osnes, Phys. Rep. **261**, 125 (1995).

[37] B.A. Brown , Progress in Particle and Nuclear Physics **47**, 517 (2001).

[38] E. Caurier, G. Marinez-Pinedo, F. Nowacki, A.Poves, J.Retamosa, A.P. Zuker, Phys. Rev C. **59**, 2033 (1999).

[39] M. Honma, T.Otsuka, B.A. Brown, T. Mizusaki, Phys. Rev C. **65**, 061301 (2002).

[40] S.E. Koonin, D.J. Dean and K. Langanke, Phys. Rep. **577**, 1 (1996).

[41] S.E. Koonin, D.J. Dean and K. Langanke, Annu. Rev. Nucl. Part. Sci. **47**, 463 (1997).

[42] M. Honma, T. Mizusaki, T.Otsuka , Phys. Rev. Lett. **77**, 3315 (1996).

[43] T.Otsuka, M. Honma, T. Mizusaki , Phys. Rev. Lett. **81**, 1588 (1998).

[44] A. L. Fetter and J. D. Walecka, *Quantum theory of many-particle systems*, MaGraw Hill, New York, 1971.

[45] http://www.physics.vanderbilt.edu/volker/p365/.

[46] P. Ring and P. Schuck, *The Nuclear Many-Body Problem*, Springer Verlag, New York, 1980.

[47] M.A. Preston and R.K. Bhaduri, *Staructure of the Nucleus*, Addison-Wesley, London, Amsterdam, 1975.

[48] J.-P. Blaizot and G. Ripka, *Quantum theory of finite systems*, The MIT Press, Cambridge, MA, 1986.

[49] P.-G. Reinhard, D.J. Dean, W. Nazarewicz, J. Dobaczewski, J. A. Maruhn and M.R. Strayer, Phys. Rev. **C60**, 014316 (1999).

[50] A.S. Umar, M.R. Strayer, J.-S. Wu, D.J. Dean and M.C. Güçlü, Phys. Rev. **C44**, 2512 (1991).

[51] S. T. Belyaev, Introduction to the Bogoliubov canonical transformation method, in *The Many-Body Problem*, edited by C. DeWitt, 1959.

[52] W. Nazarewicz, J. Dobaczewski, T.R. Werner, J.A. Maruhn, P.-G. Reinhard, K.Rutz, C.R. Chinn, A.S. Umar and M.R. Strayer, Phys. Rev. **C53**, 740 (1996).

[53] arxiv:nucl-th/0110017.

[54] G. A. Lalazissis and S. Raman and P. Ring, Atomic Data and Nuclear Data Tables **71**, 1 (1999).

[55] W. Greiner and J.A. Maruhn , *Nuclear Models*, Springer, Berlin, New York, Budapest, Paris, Tokyo, 1996.

[56] J. Bardeen, L. N. Cooper and J. R. Schrieffer, Phys. Rev. **108**, 1175 (1957).

[57] W. Pöschl, D. Vretenar, G.A. Lalazissis and P. Ring, Phys. Rev. Lett. **79**, 3841 (1997).

[58] G.A. Lalazissis, D. Vretenar, W. Pöschl, and P. Ring, Nucl. Phys. A. **632**, 363 (1998).

[59] G.A. Lalazissis, D. Vretenar, and P. Ring, Phys. Rev. C. **57**, 2294 (1998).

[60] G.A. Lalazissis, D. Vretenar, and P. Ring, Nucl. Phys. A. **650**, 133 (1999).

[61] T. Niksic, D. Vretenar, P. Finelli, P. Ring, Phys. Rev. C. **66**, 024306 (2002).

[62] T. Niksic, P. Ring, D. Vretenar, Phys. Rev. C. **71**, 044320 (2005).

[63] L.Eisenberg and E.P. Wigner, Proc. Nat. Acad. Sci. **27**, 281 (1941).

[64] J.M. Eisenberg and W.Greiner , *Nuclear Theory* , North Holland, Amsterdam, New York, 1975.

[65] J.D. Bjorken,S.D. Drell , *Relativistic quantum fields* , McGraw-Hill, New York, 1965.

[66] J.D. Walecka , *Theoretical nuclear and subnuclear physics*, Oxford University Press, New York, 1995.

[67] R.B. Wiringa, V. G. J. Stoks, R. Schiavilla, Phys. Rev. C **51**, 38 (1995).

[68] V.G.J. Stoks et. al., Phys. Rev. C **49**, 2950 (1994).

[69] H.A. Bethe and J. Goldstone, Proc. Roy. Soc. **A238**, 157 (1957).

[70] D.W.L Sprung , Nucl. Phys. **A182**, 97 (1972).

[71] P.K. Banerjee and D.W.L Sprung , Can. J. Phys. **49**, 1899 (1971).

[72] D.W.L Sprung, P.K. Banerjee, Nucl. Phys. **A168**, 273 (1971).

[73] T. H. R. Skyrme, Phil. Mag. **1**, 1048 (1956).

[74] D. Vautherin and D.M. Brink, Phys. Rev. **C5**, 626 (1972).

[75] T. H. R. Skyrme, Nucl. Phys. **9**, 615 (1959).

[76] E. Teran, PhD thesis, Vanderbilt University, 2003.

[77] N. N. Bogoliubov, Sov. Phys. JETP **7**, 41 (1958).

[78] V.E. Oberacker , *HFB research* , Vanderbilt University, 2004.

[79] M. V. Stoitsov, J. Dobaczewski, W. Nazarewicz, S. Pittel and D. J. Dean, Phys. Rev. C **68**, 054312 (2003).

[80] J. Dobaczewski, H. Flocard, J. Treiner, Nucl. Phys. **A422**, 103 (1984).

[81] J. Dobaczewski, W. Nazarewicz, T.R. Werner, J.F. Berger, C.R. Chinn and J. Dechargé, Phys. Rev. **C53**, 2809 (1996).

[82] E. Terán, V.E. Oberacker, and A.S. Umar, Phys. Rev. C **67**, 064314 (2003).

[83] V.E. Oberacker, A.S. Umar, E. Terán, and A. Blazkiewicz, Phys. Rev. C **68**, 064302 (2003).

[84] V.E. Oberacker, A.S. Umar, A. Blazkiewicz and E. Terán, A new era of nuclear structure physics, pages 179–183, World Scientific, 2004.

[85] J.L. Egido, L. M. Robledo, and Y. Sun, Nucl. Phys. **A560**, 253 (1993).

[86] J. Terasaki, P. H. Heenen, H. Flocard, and P. Bonche, Nucl. Phys. A **600**, 371 (1996).

[87] M. Yamagami, K. Matsuyanagi, and M. Matsuo, Nucl. Phys. **A693**, 579 (2001).

[88] N. Tajima , Phys. Rev. C **69**, 034305 (2004).

[89] D.R. Kegley, PhD thesis, Vanderbilt University, 1996.

[90] A.S. Umar, J. Wu, M.R. Strayer and C.Bottcher, J. Comp. Phys. **93**, 426 (1991).

[91] A.S. Umar, M.R. Strayer, R.Y. Cusson, P.-G. Reinhard and D.A. Bromley, Phys. Rev. **C32**, 172 (1985).

[92] C.Bottcher, M.R. Strayer, A.S. Umar and P.-G. Reinhard, Phys. Rev. **A40**, 4182 (1989).

[93] D.R. Kegley, V.E. Oberacker, M.R. Strayer, A.S. Umar and J.C. Wells, J. Comp. Phys. **128**, 197 (1996).

[94] J.C. Wells, V.E. Oberacker, M.R. Strayer and A.S. Umar, Int. J. Mod. Phys. **C6**, 143 (1995).

[95] A. Blazkiewicz, V.E. Oberacker, A.S. Umar, and M. Stoitsov, Phys. Rev. C. **71**, 054321 (2005).

[96] D.A. Hutchinson, E.Zaremba, A. Griffin , Phys. Rev. Lett. **78**, 1842 (1997).

[97] David Latimer (private communication).

[98] W. Gropp, S. Huss-Lederman, A. Lumsdaine, E. Lusk, B. Nitzberg, W. Saphir, M. Snir, *MPI-The Complete Reference*, The MIT Press, Cambridge, Massachusetts, London, England, 1998.

[99] P. Campbell *et al.*, Phys. Rev. Lett. **89**, 082501 (2002).

[100] A. Blazkiewicz, V.E. Oberacker, A.S. Umar, Eur. Phys. J. **A25, Supplement 1**, 543 (2005).

[101] S. Rinta-Antila,S. Kopecky,V.S. Kolhinen,J. Hakala, J. Huikari, A. Jokinen,A. Nieminen,J. Äystö, Phys. Rev. C **70**, 011301(R) (2004).

[102] E. Chabanat, P. Bonche, P. Haensel, J. Meyer and R. Schaeffer, Nucl. Phys. **A634**, 441 (1998).

[103] E. Chabanat, P. Bonche, P. Haensel, J. Meyer and R. Schaeffer, Nucl. Phys. **A635**, 231 (1998).

[104] M.V. Stoitsov, J. Dobaczewski, P. Ring and S. Pittel, Phys. Rev. **C61**, 034311 (2000).

[105] K. Hwang, A.V. Ramayya, J.H. Hamilton, D. Fong, C.J. Beyer, P.M. Gore, E.F. Jones, E. Terán, V.E. Oberacker, A.S. Umar, Y.X. Luo, J.O. Rasmussen, S.J. Zhu, S.C. Wu, I.Y. Lee, P. Fallon, M.A. Stoyer, S. J. Asztalos, T.N. Ginter, J.D. Cole, G.M. Ter-Akopian, and R. Donangelo, subm. to Phys. Rev. C (2003).

[106] G. Audi, A. H. Wapstra and C. Thibault, Nucl. Phys. **A729**, 337 (2003).

[107] P. Möller, J. R. Nix, W. D. Myers and W. J. Swiatecki, Atomic Data and Nuclear Data Tables **59**, 185 (1995).

[108] C. De Boor, *Practical Guide to Splines*, Springer Verlag, New York, 1978.

## Refereed Journal Articles and Book Chapters

1. *Hartree-Fock-Bogoliubov Calculations in Coordinate Space: Neutron-Rich Sulfur, Zirconium, Cerium, and Samarium Isotopes*, V.E. Oberacker, A.S. Umar, E. Terán, and A. Blazkiewicz, Phys. Rev. C 68, 064302 (2003)

2. *HFB Calculations for Nuclei far from Stability*, A.S. Umar, V.E. Oberacker, E. Terán, and A. Blazkiewicz, book chapter in "Structure and Dynamics of Elementary Matter", ed. W. Greiner et al.; Kluwer Academic Publishers (2004), p. 561-567

3. *Solution of the HFB continuum problem on a 2-D lattice: neutron-rich and dripline nuclei*, V.E. Oberacker, A.S. Umar, A. Blazkiewicz and E. Terán, book chapter in "A New Era of Nuclear Structure Physics", ed. Y. Suzuki, S. Ohya, M. Matsuo & T. Ohtsubo, World Scientific (2004), pp.179-183

4. *2-D Lattice HFB Calculations for Neutron-Rich Zirconium Isotopes*, A. Blazkiewicz, V.E. Oberacker, and A.S. Umar, Eur. Phys. J. A25 (Supplement 1), 543 (2005)

5. *Coordinate space Hartree-Fock-Bogoliubov calculations for the zirconium isotope chain up to the two-neutron dripline*, A. Blazkiewicz, V.E. Oberacker, A.S. Umar, and M. Stoitsov, Phys. Rev. C71, 054321 (2005) [8 pages]

## Conference Abstracts

1. *2-D Hartee-Fock-Bogoliubov Calculations For Exotic Deformed Nuclei*, A. Blazkiewicz, V.E. Oberacker, A.S. Umar, and E. Teran, APS-DNP Meeting, Tuscon, AZ (Oct. 2003), Bull. Am. Phys. Soc. 48 (2003), paper HE 6, p.95

2. *Mean field Hartree-Fock-Bogoliubov theory to model the ground state of non-stable heavy and deformed nuclei*, E. Teran, V.E. Oberacker, A.S. Umar, and A. Blazkiewicz,

APS Spring Meeting, (May 1-4, 2004, Denver, Colorado), Bull. Am. Phys. Soc. 49 (2004), paper L10.001

3. *HFB lattice calculation: zirconium isotope chain up to 2n-dripline*, Volker Oberacker, Sait Umar, and Artur Blazkiewicz, APS-DNP Meeting, Chicago, IL (Oct. 2004), Bull. Am. Phys. Soc. v.49, No.6 (2004) p.77